Theses and Dissertations

8-2019

Bioengineering Extracellular Matrix Scaffolds for Volumetric Muscle Loss

Kevin Roberts
University of Arkansas, Fayetteville

Follow this and additional works at: https://scholarworks.uark.edu/etd

Part of the Biochemical and Biomolecular Engineering Commons, Biomaterials Commons, Cell Biology Commons, and the Molecular, Cellular, and Tissue Engineering Commons

Bioengineering Extracellular Matrix Scaffolds for Volumetric Muscle Loss

A dissertation submitted in partial fulfillment
of the requirements for the degree of
Doctor of Philosophy in Cell and Molecular Biology

by

Kevin Roberts
University of Arkansas
Bachelor of Science in Biology, 2014

August 2019
University of Arkansas

This dissertation is approved for recommendation to the Graduate Council.

_____   _____
Jamie Hestekin, PhD   Jeffrey Wolchok, PhD
Dissertation Co-Director   Dissertation Co-Director

_____   _____
Kartik Balachandran, PhD   Bob Beitle, PhD
Committee Member   Committee Member

Abstract

Volumetric muscle loss overwhelms skeletal muscle's ordinarily capable regenerative machinery, resulting in fibrosis and severe functional deficits which have defied clinical repair strategies. My work spans the design and preclinical evaluation of implants intended to drive the cell community of injured muscle toward a regenerative state, as well as the development of an understanding of the molecular responses of this cell community to biomaterial interventions. I demonstrate a new class of biomaterial by leveraging the productive capacity of sacrificial hollow fiber membrane cell culture; I show specifically that unique threads of whole extracellular matrix can be isolated by solvent degradation of cultured hollow fiber systems and that this matrix exhibits composition and structure appropriate for wound healing applications. I additionally demonstrate the application of an emerging pore characterization technique and contribute a new open source software for evaluation of mesoporous pore diameter distribution and surface area, key properties governing the performance of sacrificial cell culture materials. Toward a better understanding of the biomolecular systems mediating implant efficacy, I demonstrate the first transcriptomic investigation of a specific promising combinatorial cell-scaffold implant in a rat model of volumetric muscle loss, showing an expedited recovery of muscle contractile force concurrent with a coordinated upregulation of peripheral neuroregenerative signaling. Together, these findings establish a new scalable approach for the production of biomimetic implant materials *in vitro* as well as molecular targets informing the design of promising muscle regenerative biomaterials.

Acknowledgements

Dedication

I dedicate this work to my Mother, Father, and Supriya, to whom I owe an unpayable debt for

giving me life and unwavering support.

Table of Contents

List of Published Papers

Chapter 2:

Roberts, K., Schluns, J., Walker, A., Jones, J. D., Quinn, K. P., Hestekin, J., & Wolchok, J. C. (2017). Cell derived extracellular matrix fibers synthesized using sacrificial hollow fiber membranes. *Biomedical Materials*, *13*(1), 015023 (Published).

Chapter 3:

Roberts, K., Kim, J. T., White, S., Hestekin, J., & Wolchok, J. C. (2019). Production of Extracellular Matrix Fibers via Sacrificial Hollow Fiber Membrane Cell Culture. *JoVE (Journal of Visualized Experiments)*, (144), e58791 (Published).

Chapter 5:

Roberts, K., Kim, J., Dunlap G., Hestekin J., Wolchok J. (2019). Transcriptome profiling of volumetric muscle loss repair strategies reveals synergetic neuroregenerative signaling. NPJ Regenerative Medicine. (In Review).

Chapter 1

Introduction

A. The Cell Community of Skeletal Muscle in Health and Injury

Skeletal muscle is a complex tissue which functions to enable locomotion through the transmission of force about joints. It represents the most massive constituent of the human body by mass, representing up to ~40% of adult male body mass[1,2] and therefore is a major contributing factor in resting energy expenditure[3] despite exhibiting a specific metabolic rate an order of magnitude lower than that of the major organs.[4] This tissue manifests largely as bilateral pairs of muscles comprising a specialized community of cells containing the molecular machinery which transduces action potentials into muscle contractions, producing forces which are carried across musculotendinous junctions to bone, enabling movement.

Much of the fundamental anatomy of skeletal muscle was explored in depth in the 19th century, with a remarkable number of early histological studies exploring the complex anatomy and physiology of the muscle-nerve interface across different pathologies.[5] Muscle is principally composed of cylindrical cells (myofibers) approximately 100 µm in diameter with a length of up to several centimeters and organized into bundles (fascicles) separated into a honeycomb structure by a distinct connective tissue (perimysium) comprising thick and thin layers composed primarily of the fibrillar collagens I, III, and V,[6] though the precise amount and composition of both the perimysium and the finer matrix encasing individual myofibers (endomysium) can vary considerably between muscles of different function and age.[7] The perimysium further hosts nerve fibers and arterioles branching into capillaries supplying the endomysium as well as corresponding venules. Muscle contraction is enabled by the action of complex protein superstructures termed myofibrils; Myofibrils are bundled in sarcomeres partitioned by z-discs, complex structures which

contain the largest human protein, the up-to 3000 kDa Titin, estimated to represent 8.5% of total myofibril protein.[8,9] Within each sarcomere reside "thick" and "thin" myofibril filaments composed principally of myosin and actin, respectively; myosin filaments are anchored to the center of the sarcomere (the "M-line"), while actin filaments are anchored to the z-discs. Muscle contraction is produced when these actin filaments are made to overlap myosin; action potentials stimulate myofibers to release Ca^{2+} from the sarcoplasmic reticulum into the sarcoplasm, where it binds a troponin-tropomyosin complex to uncover a binding site for myosin on actin. Conformational changes induced by binding of ATP to myosin and subsequent dissociation of P_i and ADP lead to a strong association of its actin-binding domain with actin, forming the canonical "cross-bridge"[10] which pulls actin filaments, bringing their associated z-discs closer together. An additional ATP-myosin binding event results in dissociation of the myosin-actin cross-bridge, concluding the cycle. While myofibers represent the critical contractile cell of muscle, skeletal muscle is supported by a broader community of resident and injury-responsive infiltrating cells. The innate heterogeneity of these cell populations has presented challenges in terms of the identification of reliable molecular markers. However, improvements in methods have led to emerging evidence and interest in the roles of these cells in normal muscle function, injury, and regeneration.

The cells of the skeletal muscle community can be broadly divided based on their capability for myogenic differentiation; In 1961, analysis of frog muscle electromicrographs by Alexander Mauro[11] indicated the presence of a previously unknown cell type residing between the cell membrane (sarcolemma) of myofibers and the basal lamina of the basement membrane. These *satellite cells* –so called for their adjacency to myofibers- are now known to be requisite for the regeneration of skeletal muscle.[12,13] In their quiescent state, satellite cells tend to overexpress

PAX7, a transcription factor which in these cells has been shown to regulate the transcription of hundreds of genes through a combination of paired domain and homeobox domain DNA binding.[14] Upon mild muscle injury, these cells are "activated," having been observed to undergo a phase of proliferation concurrent with coexpression of PAX7, MYF5, and ultimately MYOD. MYF 5 and MYOD appear to bind identical loci, with MYF5 promoting histone acetylation while MYOD participates in histone acetylation and the recruitment of RNA polymerase II, initiating transcription of the myogenic program.[15]   Through a variety of mechanisms, mild muscle damage incurred by exercise or trauma facilitates the action of several signals which serve to activate satellite cells, including HGF, MGF, and FGFs, with Wnt and Notch signaling also having prominent roles.[16] In particular, myofibers contain mechanosensitive Ca^{2+} import channels which are thought to respond to stretching by importing Ca^{2+} into the cytoplasm of the myofiber (sarcoplasm), where it binds calmodulin.[17] Calmodulin is bound by nitric oxide synthase (NOS), eliciting electron transfer from NADPH to an FAD domain and finally the heme prosthetic group of NOS, after which the enzyme catalyzes the conversion of arginine to citrulline and gaseous NO.[18] NO freely diffuses across the sarcolemma into the extracellular matrix, where it may participate in conversion of the zymogenic form of the matrix metalloproteinase (MMP) MMP-2 to its active form through a nitrosylation mechanism known to occur in MMP-9 activation.[19-21] MMP-2 participates in proteolytic cleavage of ECM, liberating HGF bound to collagen and other ECM constituents.[22-25] The binding of HGF with its receptor c-Met and resulting activation of the c-Met signaling pathway[26] is a key early step in satellite cell activation, and the intramuscular injection of exogenous HGF has been shown to activate quiescent satellite cells *in vivo*[27], though there also appears to be a negative feedback effect of high concentrations of HGF (>50 ng/mL) on satellite cell proliferation *in vitro* mediated by an upregulation of myostatin.[28] During this period

of proliferation, Pax7^{+}/Myf5^{-} satellite stem cells can produce two daughter cells whose fates are determined by their orientation relative to the myofiber and basal lamina; in this asymmetric division the myofiber-facing daughter cell upregulates Myf5 expression and becomes committed toward a myogenic fate (a satellite myogenic cell) while the daughter cell in contact with the basal lamina remains Myf5^{-}, which together with the planar symmetric division of Pax7^{+}/Myf5^{-} cells serves to replenish the pool of quiescent satellite cells.[29,30]Pax7^{+}/Myf5^{+} cells also undergo planar division in which case both daughters are committed to myogenesis.[31]

Following activation, satellite cells –at this point often classified as myoblasts- exhibit a remarkable ability to migrate to sites of injury across relatively large distances both along[32] and between myofibers, with some evidence indicating that these cells can migrate between adjacent muscles.[33,34] A precise mechanism of myoblast migration has yet to be described, but many of the relevant molecular participants have been identified. Myoblasts express receptors for a number of chemokines released by damaged myofibers and other cells which appear to promote myoblast migration in a manner that is independent of their effects on leukocyte recruitment.[35-37] Syndecan-4, a well described transmembrane receptor for ECM components, participates in signal transduction governing cell proliferation and motility[38], and has been directly implicated in regulating the migration of satellite cells through RhoA[39], with inhibition of this signaling also shown to impair focal adhesion formation[40]. The activity of matrix metalloproteinases –especially MMP-9- is necessary for normal myoblast migration across the ECM and basal lamina[41,42], and given the promotion of MMP activity by ECM-resident growth factors such as bFGF[43] and HGF[44], the liberation of additional ECM-bound factors during migration could play an important role in the guidance of myoblasts to injuries. The physical properties and spatial constraints of the ECM substrate also guide cell behavior in migration, with cells responding through multiple methods of

ECM digestion and turnover, including the diffuse release, cell surface localization, or lysosomal localization of proteases.[45] Upon arriving at a site of injury, myoblasts undergo a program of differentiation by which they can fuse with each other to form immature myocytes termed myotubes which themselves fuse to the sealed ends of existing damaged myofibers form a nascent regenerating myofiber.[46] Myogenin is a key myogenic regulatory factor (MRF) which in 1989 was shown to direct myoblasts toward differentiation and fusion.[47]

Intriguingly, while satellite cells are generally accepted as the principal contributors to myogenesis, some nonclassical muscle interstitial cells are capable of myogenic differentiation under certain conditions. Mitchell *et al* identified a subset of PW1$^+$/Pax7$^-$ interstitial cells (myoPICs) participating in myotube formation *in vitro* and *in vivo* that were shown to be of a separate embryonic lineage from satellite cells (PW1$^+$/Pax7$^+$) by their absence of positive recombinant β-galactosidase staining in Pax3^{Cre} × Rosa^{lacZ} mice, though they do express both Pax3 and Pax7 upon commitment to a myogenic program.[48] PICs appear to exhibit potential for skeletal muscle, smooth muscle, and fibro-adipogenic differentiation; further, a subset of PICs expressing PDGFRα exhibits an adipocyte-like pattern of gene expression *in vitro* and may have some relation to populations of fibro-adipogenic progenitors (FAPs) identified in skeletal muscle.[49] Recent evidence demonstrating a responsiveness of PICs to satellite cell depletion and an increased PIC population during rescue of myofiber atrophy by pharmacological inhibition of AcvR2B suggests physiological roles for PICs in muscle regeneration warranting further study.[50]

Rouget cells, a variety of contractile cell encircling capillary endothelial cells first described by Eberth[51] and Rouget[52-54] and recoined as "pericyten" (pericytes) by Zimmerman[55], are thought to regulate blood flow in capillaries through their contractility. However, a body of

evidence has emerged demonstrating the multipotent differentiability of these cells –as well as their mesoangioblast counterparts in the large vessels- toward osteogenic, chondrogenic, adipogenic, and myogenic lineages[56]; in fact, Crisan *et al* demonstrated that pericytes express mesenchymal stem cell (MSC) markers and display MSC-like behavior in culture regardless of their tissue of origin, intriguingly suggesting that MSCs found in adult organs may arise from a subset of pericytes.[57] Further, they demonstrated that these cells have an independent myogenic potential; when sorted pericytes were injected into cardiotoxin-injured skeletal muscles of immunodeficient mice and assessed three weeks post-injection, myotubes expressing human spectrin with central nuclei were identified, suggesting some pericytes exhibit the ability to participate in myogenesis. Interestingly, pericytes with myogenic potential do not appear to express the classic molecular markers of myogenesis during differentiation (Pax7, Myf5, or MyoD) until terminal differentiation, further distinguishing them from the canonical satellite cell population.[58] Evidence suggests that a natural contribution of skeletal muscle pericytes to myogenesis occurs mostly in the postnatal period, with minimal contribution toward adult myogenesis, even after acute cardiotoxin-induced injury[59]. Nonetheless, satellite cells are responsive to pericyte-secreted paracrine factors promoting quiescence (ANGPT1) and differentiation (IGF1), suggesting a potential indirect role for pericytes in muscle regeneration[60]. Myoblasts additionally exhibit pericyte-like patterns of gene expression –aside from maintaining Myf5 expression- when exposed to Dll4 and PDGF-BB from adjacent endothelium, suggesting some "pericytes" in skeletal muscle may derive from a satellite cell lineage[61]. Despite the apparent minimal direct contribution of pericytes to adult myogenesis, their ability to contribute to muscle regeneration following injection, underexplored paracrine crosstalk, and multipotency compel further characterization of this cell

population. In particular, the lack of highly specific markers for pericytes has to-date hindered thorough characterization and is critical for future insight into the roles of pericytes in myogenesis.

A case of induced fibroblast-myoblast transition was highlighted in a landmark study by Davis, Weintraub, and Lasser in which transfection of MYOD cDNA into 10T1/2 embryonic mouse fibroblast-like cells converted them to a myoblast-like phenotype[62]; fibroblasts have also been observed to undergo myotube formation when cultured in the presence of differentiating myoblasts *in vitro*.[63] Ito *et al* further implicated a number of coresident myoblast-expressed transcription factors in a myogenic transition of mouse tail-tip fibroblasts, including Pax3, Pax7, Mef2b, Pitx1, Mef2b, and Pitx1. These induced muscle progenitors were, however, not successfully expanded in culture.[64] While a similar approach involving adenoviral delivery of MYOD demonstrated that transformed mouse fibroblasts can participate in myofiber formation in both immunodeficient and immunocompetent mice[65], the anti-proliferative effects of exogenous MYOD hinders potential therapeutic applications and it is not clear that fibroblast-myoblast transition is a naturally occurring process *in vivo*.

Adding to the complexity of skeletal muscle regeneration is the myriad ways in which an arsenal of muscle ancillary cells shape the muscle microenvironment and secrete paracrine signals influencing cells with myogenic potential. Specifically, immune cells including neutrophils, monocytes/macrophages, dendritic cells, and $CD4^+$/$CD8^+$/regulatory T cells are now known to indirectly contribute significantly to skeletal muscle regeneration; while mechanisms of immune cell involvement in muscle regeneration are understood mostly in broad terms, they are now intensely studied for the insight they may lend to VML pathobiology and treatment.

Neutrophils -referred to as such due to Ehrlich's observation that they tend to retain neutral staining solutions[66]- are phagocytic cells of the innate immunity and the predominant form of granulocytes, cells which contain membrane-bound vesicles harboring proteases and signaling peptides which can be exocytosed for a variety of purposes.[67] They are recognized as the chief immune cell initially infiltrating skeletal muscle following muscle trauma, peaking in the immediate hours post-injury and generally declining rapidly after one day.[68] Several *in vitro* studies have established that while neutrophils have roles in debris clearance following injury, they can cause significant damage to otherwise viable myofibers through their secretion of reactive oxygen species (ROS), though the contribution of neutrophils to host-cell damage *in vivo* is less clear.[69,70] Interestingly, medium conditioned by injury of myofibers promotes neutrophil chemotaxis and ROS production *in vitro*[71], and exercise has been shown to increase production of the neutrophil chemoattractant IL-8 *in vivo*.[72] However, in VML the more probable chief contributor to neutrophil recruitment and priming following injury is injury-induced cell rupture and the resulting exposure of damage associated molecular patterns (DAMPs) recognized by cell surface receptors on circulating neutrophils as well as macrophages; these include the formylated peptides produced by both bacteria and mitochondria (bacterially derived by endosymbiosis), contributing to the apparent similarities between sterile inflammation and bacterial infection.[73-76] During infections, neutrophils form structures called neutrophil extracellular traps (NETs) which contain locally high concentrations of cytotoxic compounds. Recent evidence suggests that exposure to host mitochondrial DAMPs (mtDAMPs) may impair the formation of NETs and ROS production, possibly driving neutrophil behavior toward phagocytosis instead of degranulation[77]. Treatment of neutrophils with mtDAMPs was also shown to induce a tolerance whereby these cells become less responsive to further inflammatory stimulation. Conversely, another recent study

suggests increased NET formation and ROS production in response to endogenous mtDNA[78], so these may represent competing processes in the wound microenvironment. Regardless, extracellular mtDNA has been shown to be a potentially useful prognostic indicator for inflammation in trauma while data remains unclear on the predictive power of extracellular formyl peptides.[79] These aspects of neutrophil physiology do not appear to have been explored in the context of skeletal muscle trauma, but may participate in the degree of inflammatory response observed in the implantation of therapeutic biological materials containing residual DAMPs. As neutrophils (as well as macrophages) are capable of myofiber lysis via ROS, enzymatic inhibition of this process may be useful where it exacerbates muscle trauma, as in VML[80].

Macrophages are another immune cell type responsive to muscle injury, developing from circulating monocytes and undergoing extravasation into muscle in response to myofiber and neutrophil-secreted chemokines and DAMPs. They are among the longest-lived transient residents of injured and regenerating skeletal muscle, increasing rapidly in number roughly 2 days post-injury as neutrophils decline, and in some cases persisting for several weeks. While macrophages are well-known for their functions in pathogen and foreign body phagocytosis, evidence has emerged demonstrating roles in the skeletal muscle inflammatory and regenerative responses which vary with time course and degree of injury, evident in changes to their secretomes. Macrophages initially infiltrating muscle tend to have a pro-inflammatory effect, secreting relatively high levels of IL-12 as well as reactive oxygen and nitrogen intermediates. In typical mild muscle injury, a phenotypic transition toward a pro-constructive state is observed in the macrophage population several days post-injury, coinciding with greater secretion of IL-10 and TGF-β.[81] These alternative macrophage phenotypes were originally categorized by Mills *et al* based on their expression of nitric oxide and polyamines, respectively.[82] The former group were

9

categorized as "M1" while the latter were referred to as "M2." Subsequent studies have focused on the differing roles of these macrophage metabolic programs in disease, but recent evidence suggests a spectrum of macrophages phenotypes rather than a Boolean metabolic switch. In Novak *et al*'s examination of macrophage behavior following muscle laceration in mice, it is noted that the gene expression profiles of assessed macrophages did not correspond to the classical M1/M2 paradigm observed *in vitro*; rather, they exhibited substantial heterogeneity.[83] However, regardless of categorization, the general inflammatory-to-constructive macrophage transition in skeletal muscle is well attested.[84] In general, interventions which promote this transition have demonstrated improved myogenesis and reduced fibrosis.[85,86] Evidence suggests that inflammatory macrophages closely associate with proliferating satellite cells while those secreting anti-inflammatory factors associate with differentiating (MyoG+) myogenic precursors.[87] Further, depleting circulating monocytes in mice in the preceding study completely prevented muscle regeneration, while depletion of macrophages at later time points following injury reduce regenerating myofiber size. Fascinatingly, Ceafalan *et al* recently demonstrated by electron microscopy that macrophages establish direct cell-to-cell contacts with myogenic precursor cells from satellite cell activation through myoblast differentiation.[88] They further observed active exchange of secretory vesicles between these cells, suggesting potential modulation of cell behavior by well-known protein factors, but also epigenetic actors such as microRNAs, known to be shuttled through vesicular transport.[89,90]

T cells represent another important -though rather unexpected- participant in skeletal muscle regeneration; specifically, Burzyn *et al* showed that a population of regulatory T cells (T_{reg}) accumulates precisely during the inflammatory-to-constructive macrophage transition. They profiled the transcriptome of this T_{reg} population by microarray to show that T_{reg} cells differentially

express several hundred transcripts relative to their closest-expressing cousins (adipose T_{reg} cells). Further, depletion of T_{reg} cells in injured mouse muscle resulted in a disorganized pattern of myofiber regeneration as well as increased collagen deposition. While thorough descriptions of T_{reg} roles in injured skeletal muscle have yet to be defined, evidence indicates that their absence results in absence of the normal M1-M2 macrophage transition, causing chronic inflammation and fibrosis.[91] Burzyn *et al* recently published improved methods for isolation and characterization of T_{reg} cells which will doubtlessly enable deeper study of their participation in the regeneration of injured muscle.[92]

Perhaps the most poorly understood yet consequential cell population in skeletal muscle are the fibroadipogenic progenitors (FAPs), a population of muscle-interstitial multipotent cells which exhibit substantial heterogeneity. Recent research has identified that FAPs expressing Vcam1 exhibit a pro-fibrotic gene expression profile in period following injury, and are notably persistent in the event of macrophage depletion.[93] FAPs exhibit the capability to differentiate into fibroblasts and adipocytes and are the primary source of fibrosis and adipogenesis following muscle injury.[93] Intriguingly, despite being the chief contributors to fibrosis, preventing FAP cells ($Sca1^{+}$/$CD45^{-}$/$CD31^{-}$/$\alpha7$-integrin^{-}) from proliferating and differentiation through Nilotinib treatment impairs regeneration of muscle from acute injury, possibly due to a contribution of FAPs to satellite cell proliferation.[94] Lukjanenko *et al* recently showed that FAP function is dramatically impaired in senescence; transcriptome profiling revealed that the ability of FAPs to produce WISP1 is dramatically reduced with age, and that WISP1$^{-/-}$ mice exhibited unusually small myofibers following regeneration, which was further shown to be preventable through treatment with exogenous WISP1.[95] Thus, initial indications are that FAP cells, like others in the

skeletal muscle cell community, exhibit cross-talk with myogenic progenitors requisite for

normal tissue assembly in regeneration.

Table 1. FACS Gating Strategies for the Skeletal Muscle Cell Community

Cell type	+FACS markers	-FACS markers	Refs
Dendritic cells	Highly heterogeneous - No definitive gating strategy yet developed		[96]
Endothelial cells	$CD31^+ + \alpha7\text{-integrin}^+$	$CD45^- + F4/80^-$	[97]
FAPs	$Sca1^+$	$\alpha7\text{-integrin}^- + CD31^- + CD45^- + F4/80^-$	[97]
Macrophages	$CD45^+ + F4/80^+$		[97]
Macrophages, M1-like	$CD45^+ {}_+ CD11b^+ + CD86^+$		[98]
Macrophages, M2-like	$CD45^+ {}_+ CD11b^+ + CD163^+$		[98]
Pan-myeloid cells	$CD45^+ + CD11b$		[98]
Pericytes	$CD146^+$	$CD34^{-\,+} CD45^- + CD56^-$	[99]
Satellite cells	$\alpha7\text{-integrin}^+$	$CD45^- + F4/80^- + CD31^-$	[97]
Schwann cells	$P75NTR^+$		[100-102]
T lymphocytes	$CD3^+ + CD4^+$ and $CD3^+ + CD8\alpha^+$		[98]

13

B. Volumetric Muscle Loss

As intimated in the previous section, skeletal muscle is host to a diverse cell community which coordinates a robust regenerative program following trauma leading to functional recovery; however, in cases where large volumes (>20%) of muscle are lost to trauma, recovery is hindered due to myofiber regeneration being substituted by deposition of scar tissue following a period of prolonged inflammation. Referred to as volumetric muscle loss (VML), these injuries contribute to significant disability. In a 2016 review of US Army service members with documented VML injuries leading to medical retirement, condition was counterintuitively seen to deteriorate with time; medical evaluations observed muscle-related loss of motion and pain as well as increases in disability rating over time[103]. Aside from diligent wound debridement, skin graft closures, generally ineffective physical therapy, and pain management, there exists no consensus standard of care for VML leading to appreciable functional recovery. This is compounded by the fact that VML injuries have a naturally heterogeneous presentation. For example, while a VML injury resulting from typical bullet wounds might be confined to a relatively small area with substantial healthy tissue remaining, those resulting from primary blast injuries are more likely to result in transection of major nerves, blood vessels, and bone, as well as deep tissue infections (occurring in 27%-77% of open fracture wounds)[104-108], necessitating more aggressive treatment and complicating development of a one-size-fits-all solution.

While the general anatomy and physiology of muscle has been explored for centuries, it is largely in the past decade that a substantial interdisciplinary effort to address the unique challenges of VML has coalesced, burgeoned by interest and clinical data generated by the

14

ongoing Global War on Terror[109,110].
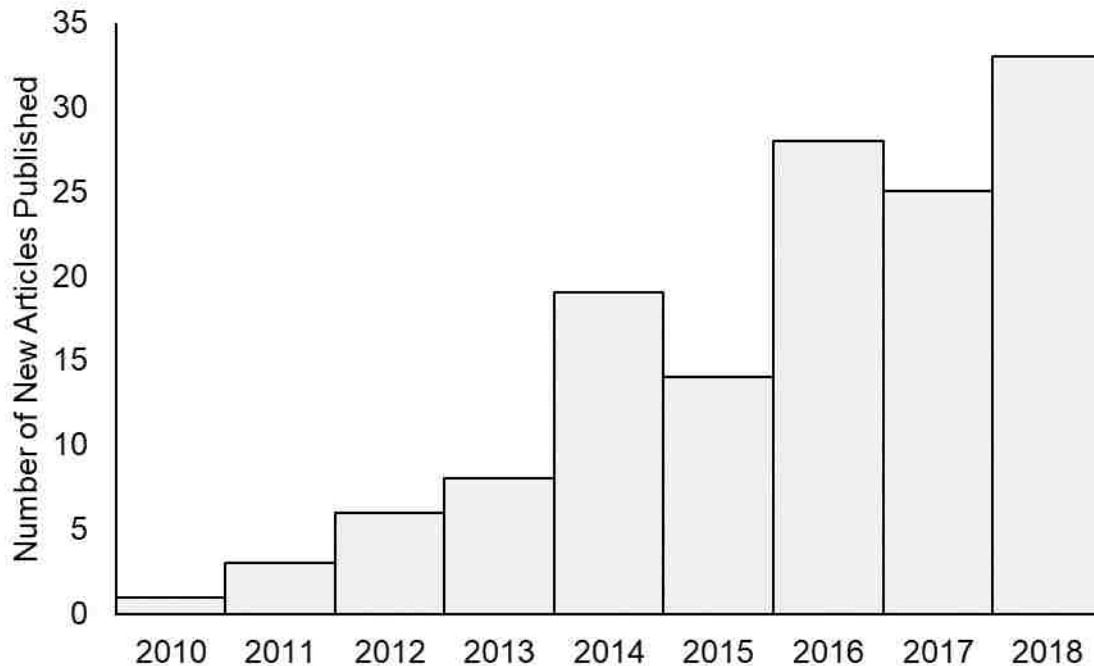
Figure 1: Research Articles Related to Volumetric Muscle Loss Indexed by PubMed

Interest in volumetric muscle loss has increased substantially in recent years, as evidenced by the past decade's positive trend in the number of new PubMed-indexed original research articles containing the keyword "volumetric muscle loss" over time. Beginning with a 2010 case report by Mase *et al* detailing positive functional recovery in the first tissue engineering-based treatment of a human VML injury, the body of VML-related literature now encompasses nearly 200 original research articles and case reports (**Figure 1**).[111] This original case report applied decellularized porcine small intestinal submucosa extracellular matrix (SIS-ECM, a biomaterial described and evaluated for tissue repair by Badylak[112]) as a scaffold to a severe injury of the quadriceps femoris muscles, resulting in considerable improvement in peak torque and total work for the affected limb.

This case report was followed by establishment of standardized mouse and rat models of VML by the Badylak[113] and Walters[114] groups which are now the basis of many studies evaluating

15

potential scaffold and cell-based therapies for VML. Implantation of lone decellularized ECM scaffolds similar to that of the original 2010 case report have been attempted in these models but have yielded mixed results. Intriguingly, Corona reported that implantation of decellularized muscle ECM in the rat VML model resulted in significant force recovery without concurrent myofiber regeneration, potentially due to the implant and resulting fibrotic mass conferring protection from overloading on the remaining healthy muscle[115]. A later study examining the effects of Losartan -an antihypertension medication which has been shown to reduce fibrosis in regenerating skeletal muscle[116,117]- on fibrosis and regeneration in rat VML revealed that while daily Losartan administration from 3 through 28 days post-injury reduced fibrosis, the functional outcome was a significant decrease in limb force along with no significant evidence of myogenesis.[118] Thus, reducing fibrosis without some other compensating factor present further impairs muscle function in VML, possibly due to the simple obstacle of the defect to force transmission.

A specific promising strategy was described by Corona *et al* in 2013 whereby implantation autologous minced muscle grafts (MMGs) at the site of injury resulted in the formation of new myofiber generation and reduced fibrosis, as well as an increase in net isometric torque compared to unrepaired limbs, though no significance was observed with when torque was normalized to muscle mass.[119] However, the addition of voluntary wheel running following MMG treatment resulted in a significant increase in muscle mass-normalized isometric torque and decrease in intramuscular collagen; the concurrent observation of decreased macrophage marker expression suggested a potential augmentation of the fibrotic response and immune cell involvement in recovery from VML. Cross-sectional area of new myofibers within the defect area decreased with the addition of exercise, potentially implicating hypertrophy of surrounding muscle in force

improvements seen, though this does not appear to have been assessed in that work and free wheel running does not appear to induce myofiber cross-sectional area in the tibialis anterior of mice[120] nor any increase in tibialis anterior mass in rats[121].

The foundational rationale for exploring the use of autologous MMGs is that they are essentially a liberation of myofibers and consequently satellite and other muscle resident cells; thus, transplantation of additional regeneration-capable cells following wound debridement might promote regeneration whereas the inflammatory and potentially infected wound environment immediately following injury and preceding debridement (and thereby a likely disruption of resident cells) presents an obstacle to regeneration by resident satellite cells. Indeed, devitalization of MMGs in VML -leaving defect-adjacent cells as the sole source of myogenic precursors- results in no notable myofiber regeneration, whereas rats treated with unmodified MMGs exhibited significant myofiber regeneration.[122] Further, the amount of autologous donor muscle required for preparing the MMG can be halved by suspending the preparation in a collagen hydrogel, leading to a functional outcome similar to that seen when the full MMG mass is used without a carrier.[123] Importantly, GFP labeling of MMG donor cells has demonstrated the direct and primary contribution of these cells to myofiber regeneration following mouse VML, with an average of 284 GFP$^+$ myofibers per tibialis anterior muscle at 28 days post-injury.[124] Encouragingly, positive effects of MMG transplantation in porcine VML have been observed, suggesting the potential scalability of this approach to the clinic, though MMG transplantation does not yet appear to have been trialed in human VML.[125]

The ineffectiveness of devitalized MMGs in promoting muscle regeneration highlights the difficulties in applying acellular scaffolds to the treatment of VML, despite the positive 2010 case report. While improved functional outcomes have been seen in the use of acellular scaffolds for

VML in some small clinical reports[126-129], these improvements are generally modest, with unconvincing evidence of myofiber regeneration and lingering functional deficits compared to uninjured limbs, implicating fibrosis-mediated improvement in force transmission as the primary contributor to recovery; this is consistent with reports of a lack of myogenesis during acellular scaffold treatment of VML in the rat model.[130] Clinical reports to date have also tended to involve interventions taking place months after the initial injury, complicating comparison of functional outcomes to existing preclinical studies which typically perform repair on the same day as injury; it is therefore difficult to ascertain the predictive value of the present body of preclinical VML studies in estimating clinical outcomes of potential therapies. Given that immediate biomaterial repair of VML is an ideal not realized in the clinic, it may be prudent in to assess promising VML therapies in animal models with a delayed onset of repair from the time of injury. Such studies will yield clinically relevant insight into whether promising therapies are able to revive a muscle-regenerative program weeks or months after the initial injury when fibrosis of the wound is complete. Additional clinical study is clearly needed as well, as the cumulative number of VML patients in clinical reports reviewed here totals only ~22 subjects, with varying sites, degrees, and manners of injury, though it is recognized that the natural heterogeneity of VML presents difficulties in acquiring subjects suitable for controlled study.

Griesing *et al* evaluated two commercially available FDA-approved ECM biomaterials (SIS and urinary bladder matrix (UBM)) and hyaluronic acid hydrogel in the repair of VML in a porcine model, assessing both neuromuscular strength and transcriptome profiles by RNA-sequencing at 12 weeks post-injury. Notably, repair with SIS or UBM resulted in functional outcomes equivalent to unrepaired VML, and SIS implantation was observed to result in substantial inflammation in the days following surgery. While a detailed breakdown of

overrepresented pathways by treatment group was not presented, unrepaired and repaired muscles exhibited substantial numbers of unique differentially expressed genes (DEGs), with 499 DEGs unique to the SIS-treated group alone. Interestingly, there were no significant overrepresented pathways for the sets of DEGs unique to each treatment group, and PCA analysis revealed clustering of all VML-injured groups, suggesting that the treatment strategies assessed do not alter global transcriptome expression in a coordinated manner at 12 weeks post-injury.

Aguilar *et al* recently performed a somewhat more detailed transcriptome profiling of VML and autologous minced muscle autograft repair in the rat model across time points ranging from 3 to 14 days post injury. Interestingly, MM repair of VML resulted in a similar transcriptional trajectory as unrepaired VML, showing a persistent upregulation of inflammation and fibrosis-related transcripts in response to VML (1925 total DEGs at 3 days post injury to 16 DEGs at 28 days), though a detailed analysis of DEGs in the MM group in comparison to the VML set was not presented. It is therefore unclear from this work whether there any distinct transcriptional behavior occurring in the MM treatment group which could contribute to the improved functional outcome relative to untreated VML. Regardless, it is clear that MM alone does not change the overall fibrotic fate of the VML wound environment.

An underexplored aspect of VML is how the neuromuscular unit is affected by severe muscle injury, with what degree ostensibly effective preclinical biomaterial therapies are modulating peripheral nerve repair remaining largely unclear. It is evident that if substantial injury occurs to axons and neuromuscular synapses in the largely intact muscle adjacent to a VML injury, that muscle may atrophy from disuse without timely repair, and whether this is a common occurrence in VML remains unclear. Corona *et al* recently advanced this area considerably by demonstrating that a VML injury ablating 20% of the tibialis anterior in Lewis rats results in a

disproportionate degree of motoneuron axotomy in the tibialis anterior, with an average of 69% of motoneurons innervating the tibialis anterior being subjected to axotomy[131,132]. This finding was based on pre-surgical and post-surgical labeling by intramuscular injection of Alexafluor-conjugated Cholera Toxin Subunit B, which is commonly used as an approach for both retrograde and anterograde labelling of neurons and their associated axons[133]. CTB is principally a ligand for the GM1 ganglioside present on the surface of neurons, which is endocytosed following CTB-binding, allowing for imaging of the entire neuron and axonal tract[134,135]. Thus, this specific assay may be a useful indicator of axotomy for future investigations utilizing animal VML models, though Corona *et al* did not specify in their publication the exact area of the spinal cord assessed.

The finding of motoneuron axotomy in VML, its correlation with muscle force deficits, and apparent persistent lack of axon recovery in the weeks following VML injury suggests that the neuromuscular units of ostensibly intact adjacent muscle tissue are negatively impacted, and consequently that this neuromuscular disruption has a role in long term VML deficits. It has long been known that axotomy of muscle-innervating nerves results in significant atrophy of the formerly innervated muscle tissue[136], and therefore a goal of successful VML therapies should be to address damage to the neuromuscular unit where it occurs, by promoting the regeneration of cut axons and then formation of functional neuromuscular junctions; the key chemical synapses mediating the transduction of an action potential into muscle contraction. The general outcomes of muscle innervation following nerve injury have been studied in some depth in the plantar muscles such as the tibialis anterior assessed in most preclinical studies, often through crush of the sciatic nerve, which contains distal branches innervating muscles of the lower limbs.

One proposed approach to accelerating peripheral nerve repair is the application of electrical stimulation, which has been shown in various animal studies to promote the onset of

axonal regeneration.[137-139] Notably, it has been shown in rats that it is specifically brief low frequency stimulation (2 Hz) which promotes regeneration, with higher frequencies (200 Hz) resulting in less regeneration of sciatic nerve following injury.[140] Asensio-Pinilla *et al* demonstrated that a combination of treadmill running (5 meters per minute for 2 hours daily) with a one-hour electrical stimulation immediately following injury (3 volts, 20 Hz) resulted in significantly increased muscle innervation and number of regenerated axons compared to control rats and those subjected to chronic (1 hour daily) electrical stimulation.[141] Further, similar positive outcomes were observed in a clinical pilot study in which patients undergoing carpal tunnel release surgery were subjected to an acute electrical stimulation (1 hour, 4-6 volts, 20 Hz) of the median nerve[142]; quantification of axonal regeneration by motor unit number estimation (MUNE) revealed that patients subjected to electrical stimulation following surgery on average exhibited a remarkable comparable-to-normal innervation at 12 months post-surgery, while patients undergoing surgery only experience no significant increases in number of motor units when evaluated 3-12 months post-surgery. Brief electrical stimulation has also been shown to improve outcomes in recent clinical application toward shoulder dysfunction[143], recovery following digital nerve transection[144], as well as reduce pain[145]. However, the literature is less clear on whether such an approach would yield similar results when it is the downstream muscle-nerve unit subjected to direct injury rather than an upstream nerve. In contrast to much of the literature, limited reports suggest that electrical stimulation can have an adverse effect on the neuromuscular unit in the plantar muscles[146], or may prevent muscle atrophy while not appreciably affection reinnervation[147]. The molecular changes potentially mediating the effects of electrical stimulation have not been extensively characterized, but several studies have observed significant increases in neurotrophin expression following stimulation, including BDNF and GDNF.[148-151]. Specifically,

in vitro evidence suggests that exogenous BDNF promotes neurite outgrowth through activation of JAK/STAT signaling[152] as well as neuron survival[153]. The general trend of promising preclinical and clinical outcomes observed in the application of brief electrical stimulation toward restoring muscle innervation following upstream nerve injury invites preclinical exploration of the approach as an additional low-risk therapy for VML.

Biomaterials-based approaches to nerve regeneration have been extensively discussed in the recent neuroregenerative literature.[154-159] Nerve grafts are used in the clinical repair of peripheral nerve injury but, like muscle grafts, involve limited availability and the possibility of immunological reaction; considerable interest therefore exists in generating synthetic materials to promote nerve regeneration. Typically taking the form of a polymeric tube which is bridged across a nerve defect, successful nerve regeneration across defects of 10-30 mm are is well attested. Greater yet distances have been bridged through the use of collagen sponges, with one study in dogs indicating successful regeneration across an 80 mm nerve defect.[160] While biomaterials specifically targeting peripheral nerve regeneration in the context of VML are not yet described, evidence does exist that the class of allogeneic decellularized scaffolds that are commonly assessed for VML repair may improve muscle innervation following injury.[161]

C. Bioengineering Regenerative Materials *In Vitro*

While decellularized allogeneic and xenogeneic scaffolds are popular for their demonstrated potential in the repair of several tissues including skeletal muscle, the limited availability of cadaveric tissue and the potential for immune reaction to foreign epitopes are limiting factors in their application, particularly toward tissues which are not scar-tolerant or in which a foreign body reaction could prove fatal; such was the case in the implantation of Synergraft decellularized porcine heart valves, resulting in the death of three children due to inflammation-induced implant failure and subsequent explantation of the valve from the fourth child.[162]

A potential alternative for decellularized cadaveric tissues exists in the rapidly developing field of *in vitro* tissue engineering. While the prospect of producing whole functioning organs *in vitro* remains somewhat elusive, the production of extracellular matrix (ECM) -the foundational structure of any decellularized cadaveric tissue- *in vitro* is an existing technology. However, typical ECM production involves the culture of cell monolayers and the gentle mechanical or enzymatic dissociation of the cell/ECM sheet from its substrate[163,164]. Alternatively, a promising approach enabled by advances in material science in the past decades is the development of cell culture systems using temperature-responsive polymers as the cell substrate. Poly(N-isopropylacrylamide) (NIPAAM) is a polymer which dissolves in water below 32 °C due to conformational changes induced in the polymer chain induced by hydration[165]; Yamada and Okano *et al* demonstrated that this property allowed for deadhesion of hepatocytes from a NIPAAM-grafted polystyrene surface.[166] Interestingly, cells generally do not adhere efficiently to thick (>30 nm) layers of NIPAAM due to insufficient dehydration of polymer chains, resulting in insufficient hydrophobicity for cell adhesion.[167] Thus, constructs for thermally responsive deadhesion of cells and ECM typically use nanoscale layers of NIPAAM grafted to existing cell culture surfaces.

Regardless of substrate composition or method of ECM retrieval, conventional 2D culture has significant limitations in the retrieval of cell products. Principally, the relatively low surface area of flat culture flasks results in a low adherent cell density and protein productivity relative to that exhibited in suspension culture. For example, a typical 75 cm^2 cell culture flask may achieve approximately 100,000 cells/cm^2, utterly dwarfed by the extreme cell densities achievable (in excess of $100*10^6$ cells/mL) with suspension culture of the Chinese hamster ovary (CHO) cells currently used for 70% of industrial antibody production[168]. While it is intuitive that adherent cell systems are inherently less productive than suspension culture, most cell types of tissue engineering interest are anchorage-dependent, and bioreactor systems now exist which leverage high surface area substrates to maximize cell density and productivity.

Among the most productive of these is the hollow fiber bioreactor. Knazek *et al* described in 1972 the culture of fibroblasts on cellulose acetate capillaries, yielding 1 mm diameter growths following 28 days of incubation; the authors remarked the high cell densities culturable in a such a high surface area-to-volume-ratio system and thus the potential to engineer tissues *in vitro*.[169] In the decades since, hollow fiber membrane-based bioreactor systems have seen commercial application for the production of monoclonal antibodies in addition to their ubiquitous application in industrial separations processes. Hollow fibers are attractive as cell culture substrates due to their high surface area, tunable pore diameters governing their transport properties, and a wide range of materials allowing one to tailor the substrate properties for cell proliferation and survival.

Figure 3: Example of a Simple Hollow Fiber Membrane Bioreactor

The typical hollow fiber membrane bioreactor (**Figure 3,** example by author) takes the

form of a cylindrical cartridge in which rest hundreds of individual hollow fibers sealed at each

end by a biocompatible resin, with anchorage-dependent mammalian cells cultured on the outer

surfaces of the membranes and medium pumped through the extracapillary space of the

cartridge. While the assembly of such a bioreactor seems in principle relatively straightforward,

the choice of membrane substrate, perfusion rate, atmospheric conditions, fiber spacing[170], and

cartridge material have significant effects on cell survival, proliferation, and productivity.

Hollow fiber bioreactor development is an active area of private development, with several

recent patents on the matter[171-174] and commercial availability of ready-to-use bioreactor systems

such as those produced by FiberCell Systems, with surface areas of up to 1.2 m^2 and

corresponding cell densities of up to $5.0E^{10}$ cells in a single 60 mL cartridge[175].

Hollow fiber bioreactors have been of interest for use in tissue production as artificial

organs since the early investigations into the scalability of hollow fiber cell culture and modeling

of their transport properties.[176-178] In the context of ECM production, Potter *et al* demonstrated

the ability to grow 1 mm-thick masses of cartilage[179] after four weeks of culturing embryonic

chick chondrocytes in a hollow fiber bioreactor system, with development of tissue monitored by

MRI. Oxygen transport is considered to be the most limiting factor in the bioreactor culture of

mammalian cells, including within the hollow fiber bioreactor.[180] For example, when a

membrane-anchored biofilm grows -as with the development of cartilage in the Potter study- the

diffusive transport of oxygen and key medium nutrients across the membrane is hindered. Given

the short distances across which solely diffusive transport of oxygen across tissues is relevant

(~1 mm)[181], the addition of convective transport of oxygen is critical[182], as illustrated by Ku *et*

al's observation that as much as much as 25% of the dissolved oxygen in fresh medium is

consumed as it is perfused through a hollow fiber bioreactor.[176]

D. Fabrication, Tuning, and Characterization of Hollow Fiber Membranes

Hollow fiber membranes are ubiquitous in industrial separations for their ability to separate components of various streams based on size exclusion via layers of selective pores, with an application of transmembrane pressure and concentration gradients being the primary driving forces for permeation through the membrane. Hollow fibers commonly manifest as the asymmetric type, characterized by an exofacial layer of pores and a lumen-facing layer of pores bridged by a sponge-like support layer, as visible in this example of a NIPS polysulfone hollow fiber membrane fabricated by the author (**Figure, 2** scale-bar = 100 µm). Hollow fibers are engineered via a tunable process known as phase inversion. Phase inversion is a process which leads to the phase transition of a polymer solution from liquid to solid, precipitating a porous membrane.[183] It is one of the most prominent methods of membrane fabrication and can occur by several distinct mechanisms; these include nonsolvent-induced phase separation (NIPS), thermally induced phase separation (TIPS), evaporation-induced phase separation (EIPS) and vapor-induced phase separation (VIPS). NIPS-driven phase inversion occurs by exchange of nonsolvent for solvent upon immersion of a polymer solution in nonsolvent, while TIPS causes phase separation by extrusion of a heated polymer preparation into a cooling bath.[184-187] VIPS can be considered a special case of the NIPS mechanism, wherein the nonsolvent used is in the vapor phase.[188,189] Specific manufacturing processes can exploit combinations of these mechanisms to varying degrees. One of the more accessible processes is wet spinning, a form of hollow fiber fabrication based on the NIPS mechanism.

27
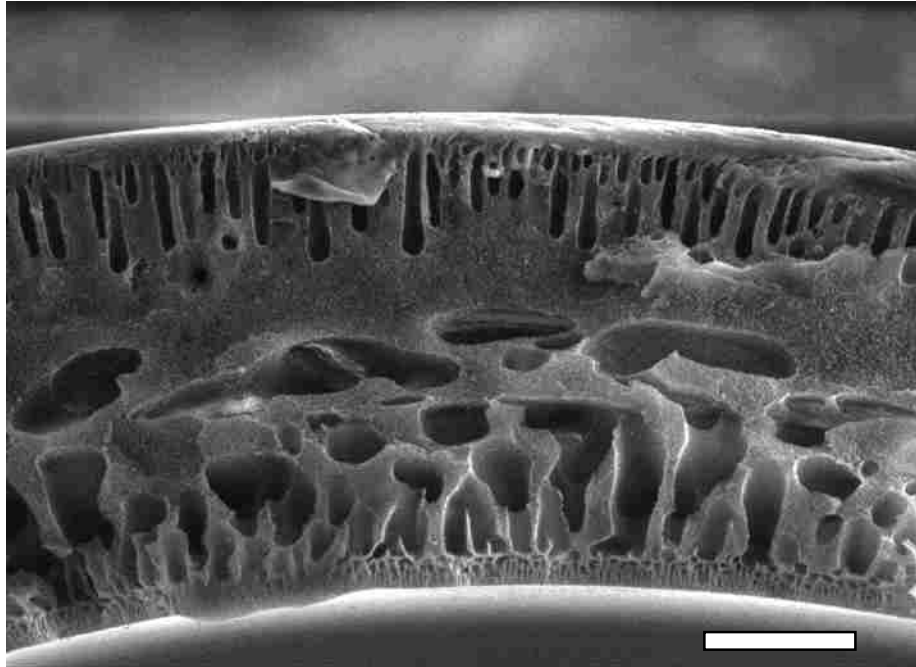
Figure 2: Example SEM micrograph of a NIPS-Cast Hollow Fiber Membrane

Wet spinning involves the extrusion of dope (polymer) and bore solutions through a spinneret, after which the combined streams enter an external coagulant (usually water), leading to the precipitation of a solid hollow fiber membrane by phase inversion; it is thus analogous to the immersion precipitation process for fabricating flat membranes. There is frequently an "air gap" between the outlet of the spinneret and the surface of the external coagulant; when an air gap is used, the process is termed dry-jet wet spinning. The phase inversion process begins immediately upon exit of the two streams from the spinneret, first primarily by evaporation of the solvent (if an air gap is present) and then by bulk exchange of solvent and nonsolvent (NIPS-driven) or cooling of a heated polymer dope (TIPS-driven) as the nascent fiber enters the coagulant bath. Extrusion can be achieved either through the use of pumps or a pressurized inert gas, wherein the pressures required for extrusion differ depending on factors such as the viscosity of the dope and bore solutions, as well as the dimensions of the spinneret.

Performance of hollow fiber membranes in size exclusion separations is often expressed in terms of a molecular weight cut-off (MWCO). The MWCO of a membrane is generally defined as the molecular weight of a compound in solution for which a membrane would reject greater than 90%.[190] Ultimately, the relation between molecular weight and rejection is only an approximation for which there are many exceptions, as rejection also depends on the specific structure and electrostatic characteristics of molecules; this is elegantly illustrated by the fact that relatively large plasmids can be transported through ultrafiltration membranes via elongation as they converge on pores, a result that would not be expected if molecular weight were the principal factor.[191] Despite this, MWCO is a useful property when used in reference to a common class of molecules, and is a ubiquitously reported property of membranes intended for protein separations. Determination of MWCO is often accomplished by evaluating the membrane separation of polyethylene glycols of varying molecular weight.[192,193] While MWCO provides a practical rule of thumb for the end user, analysis of membrane structure and composition are necessary for a predicting and tuning membrane performance during research and development.

The dimensions, distributions, and frequencies of pores dictate the size exclusion properties of a membrane. In a biopharmaceutical context, membranes of several different nominal pore sizes are used at different stages of separation, in part to prevent unnecessary fouling of highly selective membranes by large debris removable by less selective membranes. Microfiltration membranes (0.1 – 1 µm pores) or microsieves are commonly used to remove bacteria from a stream, while ultrafiltration membranes (1-100 nm) can be used to effectively separate viruses and high molecular weight components for purification of protein. Adsorption of protein within or adjacent to membrane pores is a common challenge in biological separations and is best prevented by using

a membrane least prone to fouling in the specific application. Thus, characterizing and tuning pore size distribution are critical aspects of membrane design.

Scanning electron microscopy (SEM) is sometimes used to observe pore size, but comes with several important caveats. Most importantly, SEM generally assesses a very small area of sample which may not be representative of the whole. Further, these analyses are most commonly made based on surface level images, and so the pore diameter determined by the investigator is typically of the pore opening rather then the pore throat that is most relevant to transport. Additionally, a more minor consideration is that the sputter-coating process for preparation of SEM samples may result in a smaller apparent pore size, though this is most relevant in the case of nanofiltration pores (<10 nm). Mercury porosimetry has been used for decades for determining the pore size distribution of a great variety of materials, including membranes. It is based on an inverse relation between the pressure required to push mercury into a pore and the size of that pore, as described by a modified form of the Young-Laplace equation referred to as the Washburn equation. However, there are several important caveats to consider regarding the use of this technique for membranes; first, the high pressures required to force mercury through a membrane may damage the membrane and thus alter its pore size distribution. Secondly, mercury porosimetry does not measure the most constricted portion of a pore channel; rather it determines the diameter of the pore's entrance, which is not as important to transport as the former property. It also does not distinguish between dead-end pores (which do not function in size exclusion) and continuous pores. Further, the instrumentation –while readily available from several commercial sources- can be quite expensive compared to alternative techniques. However, mercury porosimetry does have the advantage of being rapid and applicable across a relatively wide pore size range.

LLDP is an attractive technique for the measurement of ultrafiltration membrane pores, as it uses relatively low pressures compared to those required for mercury intrusion, avoiding compaction of membranes that could produce erroneous results, and generally measures the diameter of the continuous pores that are relevant to transport.[194] Further, it also evaluates the membranes while wetted, as they might be under operating conditions.[195] LLDP operates through the displacement of a wetting liquid in the membrane by a "displacing" liquid. As pressure is increased stepwise, the Hagen–Poiseuille equation can be used to generate a pore size distribution based on flux of displaced water.[196] Another useful aspect of LLDP is that it can be used to estimate the molecular weight cutoff (MWCO) of ultrafiltration membranes, as described by Calvo *et al*.[197] Despite the utility of LLDP, any interactions between the liquids used and the membrane that may affect its pore size distribution (e.g., swelling) must be considered.[198]

Nitrogen adsorption-desorption is generally considered the gold-standard technique for analysis of surface area and pore diameter, with widely available commercial equipment. In 1938 Brunauer, Emmet, and Teller published their method for relating the adsorption of gas to the surface area of the adsorbent.[199] Though the theory is based on the Langmuir model of adsorption which makes the assumption that the adsorbent is of a planar geometry[200], the BET theory remains the industrial standard for determination of surface area. In 1951 Barrett, Joyner, and Halenda described a procedure (BJH) for relating gas adsorption to pore diameter based on the Kelvin equation.[201] It is remains commonly used, but is criticized for resulting in high error as nominal pore size decreases.

Despite various advantages of the aforementioned techniques -including their broad use in literature enabling convenient comparison- common to all of them is the necessity of fairly specialized and expensive equipment which may not be accessible to investigators interested in

pore diameter who are not specialists in pore characterization. Evapoporometry is a novel method for calculation of pore diameter distribution which relates the instantaneous evaporation rate of a fluid from a saturated sample to the diameter of instantaneously draining pores via a derivation of the Kelvin equation:

$$d = - \frac{4yV}{RT ln \frac{W_{A0}}{W_{A0}^{\circ}}}$$

where y is surface tension, V is vapor molar volume, R is the universal gas constant, T is absolute temperature, W_{A0} is the instantaneous evaporation rate and W_{A0}° is the average rate of evaporation for a layer of the volatile fluid initially overlying the sample. Evapoporometry is most notable for the fact that it requires only materials that are ubiquitous in most engineering laboratories: an analytical balance with a 10 µg resolution and PC interface, a PTFE test cell in which to secure a fluid saturated sample, and a volatile fluid of choice. Evaporative mass loss is to molar evaporation rate (W_{A0} and W_{A0}°) and used with surface tension (of the fluid), vapor molar volume, and absolute temperature to yield the pore diameter in meters for pores draining at a particular instant. Importantly, evaporation proceeds in descending order of pore size due to supersaturation of vapor for all pores smaller than those draining at any instant. However, the method incurs some limitations, chiefly an upper limit of pore detection of ~300 nm[202], the possibility of fluid-sample interactions, and an unstandardized graphical analysis approach for data analysis which has in practice lead to considerable user-to-user variation in analysis of identical datasets. Further, the method has largely been validated with idealized flat sheet membranes with well defined pores, and it remains whether the precision of the technique is maintained when used for more irregular samples such as solvent-cast membranes or ion exchange resins. Finally, given the known relationship between pore diameter and surface area, there is expected to be a proportionality

between evaporated mass and surface area, but this has not been specifically evaluated in the literature. A software-aided approach to address challenges in evapoporometry data analysis is discussed in chapter 4.

E. Objective

The primary objectives of this work are threefold: to evaluate the feasibility of a sacrificial hollow fiber membrane cell culture approach for the production of matrix scaffolds targeted toward VML, improve the methodology for characterizing the dimensions of pores influencing the performance of membranes in industrial separations and cell culture, and to develop a better understanding of the biomolecular processes mediating recovery in biomaterial-based repair of VML.

We first demonstrate the isolation of bulk threads of ECM *in vitro* through the intraluminal seeding of ECM-productive mammalian cells in solvent-degradable hollow fiber membranes. We further characterize the mechanical and biochemical properties of ECM isolated from sacrificial scaffolds, demonstrate its assembly into implantable meshes, and show that it supports the viability of mammalian cells *in vitro*. We additionally provide a separate detailed description of methods for producing bulk ECM by this approach, from membrane fabrication through implant processing.

In the interest of increasing the accessibility of pore dimension analysis beyond the membrane specialist, we develop an open-source Python GUI tool for the analysis of Evapoporometry data. We show that software-aided analysis yields precise analysis of pore diameter for well-characterized membranes as well as ion exchange resin, in agreement with analysis by gold-standard methods. We further demonstrate the initial application of this method for evaluating relative differences in surface area.

Finally, we perform the first transcriptomic analysis by RNA-sequencing of a combined decellularized skeletal muscle (DSM) plus autologous minced muscle (MM) VML repair approach which in our previous work has been shown to restore over 50% of muscle contractile force lost to VML in a rat model.[203] We demonstrate that the primary patterns of gene expression correlating

with force recovery in the two-week period following injury are primarily of a neuroregenerative

nature, with significant implications for future VML research.

References

1   Shephard, R. J. & Shephard, R. F. *Body composition in biological anthropology*. Vol. 6 (Cambridge University Press, 1991).

2   Janssen, I., Heymsfield, S. B., Wang, Z. & Ross, R. Skeletal muscle mass and distribution in 468 men and women aged 18–88 yr. *Journal of applied physiology* **89**, 81-88 (2000).

3   Zurlo, F., Larson, K., Bogardus, C. & Ravussin, E. Skeletal muscle metabolism is a major determinant of resting energy expenditure. *The Journal of clinical investigation* **86**, 1423-1427, doi:10.1172/JCI114857 (1990).

4   Wang, Z. *et al.* Evaluation of specific metabolic rates of major organs and tissues: comparison between men and women. *American journal of human biology : the official journal of the Human Biology Council* **23**, 333-338, doi:10.1002/ajhb.21137 (2011).

5   Batten, F. E. The muscle spindle under pathological conditions*Brain* **20**, 138-179, doi:10.1093/brain/20.1-2.138 (1897).

6   Light, N. & Champion, A. E. Characterization of muscle epimysium, perimysium and endomysium collagens. *The Biochemical journal* **219**, 1017-1026 (1984).

7   Purslow, P. P. The structure and functional significance of variations in the connective tissue within muscle. *Comparative Biochemistry and Physiology Part A: Molecular & Integrative Physiology* **133**, 947-966, doi:https://doi.org/10.1016/S1095-6433(02)00141-1 (2002).

8   Fulton, A. B. & Isaacs, W. B. Titin, a huge, elastic sarcomeric protein with a probable role in morphogenesis. *BioEssays* **13**, 157-161, doi:doi:10.1002/bies.950130403 (1991).

9   Trinick, J., Knight, P. & Whiting, A. Purification and properties of native titin. *Journal of Molecular Biology* **180**, 331-356, doi:https://doi.org/10.1016/S0022-2836(84)80007-8 (1984).

10   De La Cruz, E. M. & Ostap, E. M. Relating biochemistry and function in the myosin superfamily. *Current Opinion in Cell Biology* **16**, 61-67, doi:https://doi.org/10.1016/j.ceb.2003.11.011 (2004).

11   Mauro, A. Satellite cell of skeletal muscle fibers. *The Journal of biophysical and biochemical cytology* **9**, 493-495 (1961).

12   Sambasivan, R. *et al.* Pax7-expressing satellite cells are indispensable for adult skeletal muscle regeneration. *Development* **138**, 3647-3656, doi:10.1242/dev.067587 (2011).

13   von Maltzahn, J., Jones, A. E., Parks, R. J. & Rudnicki, M. A. Pax7 is critical for the normal function of satellite cells in adult skeletal muscle. *Proceedings of the National Academy of Sciences* **110**, 16474-16479, doi:10.1073/pnas.1307680110 (2013).

14   Soleimani, V. D. *et al.* Transcriptional dominance of Pax7 in adult myogenesis is due to high-affinity recognition of homeodomain motifs. *Developmental cell* **22**, 1208-1220, doi:10.1016/j.devcel.2012.03.014 (2012).

15   Conerly, M. L., Yao, Z., Zhong, J. W., Groudine, M. & Tapscott, S. J. Distinct activities of Myf5 and MyoD indicate separate roles in skeletal muscle lineage specification and differentiation. *Developmental cell* **36**, 375-385 (2016).

16   Fu, X., Wang, H. & Hu, P. Stem cell activation in skeletal muscle regeneration. *Cellular and molecular life sciences : CMLS* **72**, 1663-1677, doi:10.1007/s00018-014-1819-5 (2015).

17   Tatsumi, R. *et al.* A role for calcium-calmodulin in regulating nitric oxide production during skeletal muscle satellite cell activation. *American journal of physiology. Cell physiology* **296**, C922-929, doi:10.1152/ajpcell.00471.2008 (2009).

18   Knowles, R. G. & Moncada, S. Nitric oxide synthases in mammals. *The Biochemical journal* **298 (Pt 2)**, 249-258 (1994).

19   Gu, Z. *et al.* S-nitrosylation of matrix metalloproteinases: signaling pathway to neuronal cell death. *Science* **297**, 1186-1190 (2002).

20   Maeda, H., Okamoto, T. & Akaike, T. Human matrix metalloprotease activation by insults of bacterial infection involving proteases and free radicals. *Biological chemistry* **379**, 193-200 (1998).

21   Viappiani, S. *et al.* Activation and modulation of 72kDa matrix metalloproteinase-2 by peroxynitrite and glutathione. *Biochemical pharmacology* **77**, 826-834, doi:10.1016/j.bcp.2008.11.004 (2009).

22   Mohammed, F. F. *et al.* Metalloproteinase inhibitor TIMP-1 affects hepatocyte cell cycle via HGF activation in murine liver regeneration. *Hepatology* **41**, 857-867, doi:doi:10.1002/hep.20618 (2005).

23   Schuppan, D. *et al.* Collagens in the liver extracellular matrix bind hepatocyte growth factor. *Gastroenterology* **114**, 139-152 (1998).

24   Rahman, S. *et al.* Novel hepatocyte growth factor (HGF) binding domains on fibronectin and vitronectin coordinate a distinct and amplified Met-integrin induced signalling pathway in endothelial cells. *BMC Cell Biology* **6**, 8, doi:10.1186/1471-2121-6-8 (2005).

25   Tatsumi, R. & Allen, R. E. Active hepatocyte growth factor is present in skeletal muscle extracellular matrix. *Muscle & Nerve* **30**, 654-658, doi:10.1002/mus.20114 (2004).

26   Organ, S. L. & Tsao, M.-S. An overview of the c-MET signaling pathway. *Therapeutic advances in medical oncology* **3**, S7-S19, doi:10.1177/1758834011422556 (2011).

27   Tatsumi, R., Anderson, J. E., Nevoret, C. J., Halevy, O. & Allen, R. E. HGF/SF is present in normal adult skeletal muscle and is capable of activating satellite cells. *Developmental biology* **194**, 114-128 (1998).

28   Yamada, M. *et al.* High concentrations of HGF inhibit skeletal muscle satellite cell proliferation in vitro by inducing expression of myostatin: a possible mechanism for reestablishing satellite cell quiescence in vivo. *American Journal of Physiology-Cell Physiology* **298**, C465-C476, doi:10.1152/ajpcell.00449.2009 (2010).

29   Kuang, S., Kuroda, K., Le Grand, F. & Rudnicki, M. A. Asymmetric self-renewal and commitment of satellite stem cells in muscle. *Cell* **129**, 999-1010 (2007).

30   Yin, H., Price, F. & Rudnicki, M. A. Satellite Cells and the Muscle Stem Cell Niche. *Physiological Reviews* **93**, 23-67, doi:10.1152/physrev.00043.2011 (2013).

31   Aziz, A., Sebastian, S. & Dilworth, F. J. The origin and fate of muscle satellite cells. *Stem Cell Reviews and Reports* **8**, 609-622 (2012).

32   Schultz, E., Jaryszak, D. L. & Valliere, C. R. Response of satellite cells to focal skeletal muscle injury. *Muscle & Nerve* **8**, 217-222, doi:doi:10.1002/mus.880080307 (1985).

33   Jockusch, H. & Voigt, S. Migration of adult myogenic precursor cells as revealed by GFP/nLacZ labelling of mouse transplantation chimeras. *Journal of cell science* **116**, 1611-1616 (2003).

34   Watt, D. J., Morgan, J. E., Clifford, M. A. & Partridge, T. A. The movement of muscle precursor cells between adjacent regenerating muscles in the mouse. *Anatomy and embryology* **175**, 527-536 (1987).

35   Warren, G. L. *et al.* Role of CC chemokines in skeletal muscle functional restoration after injury. *American Journal of Physiology-Cell Physiology* **286**, C1031-C1036, doi:10.1152/ajpcell.00467.2003 (2004).

36   Yahiaoui, L., Gvozdic, D., Danialou, G., Mack, M. & Petrof, B. J. CC family chemokines directly regulate myoblast responses to skeletal muscle injury. *The Journal of Physiology* **586**, 3991-4004, doi:doi:10.1113/jphysiol.2008.152090 (2008).

37   Griffin, C. A., Apponi, L. H., Long, K. K. & Pavlath, G. K. Chemokine expression and control of muscle cell migration during myogenesis. *Journal of cell science* **123**, 3052-3060, doi:10.1242/jcs.066241 (2010).

38   Elfenbein, A. & Simons, M. Syndecan-4 signaling at a glance. *Journal of cell science* **126**, 3799-3804, doi:10.1242/jcs.124636 (2013).

39   Shin, J., McFarland, D. C. & Velleman, S. G. Migration of turkey muscle satellite cells is enhanced by the syndecan-4 cytoplasmic domain through the activation of RhoA. *Molecular and cellular biochemistry* **375**, 115-130, doi:10.1007/s11010-012-1534-1 (2013).

40   Dovas, A., Yoneda, A. & Couchman, J. R. PKCα-dependent activation of RhoA by syndecan-4 during focal adhesion formation. *Journal of cell science* **119**, 2837-2846 (2006).

41   Nishimura, T. *et al.* Inhibition of matrix metalloproteinases suppresses the migration of skeletal muscle cells. *Journal of Muscle Research and Cell Motility* **29**, 37-44, doi:10.1007/s10974-008-9140-2 (2008).

42   El Fahime, E., Torrente, Y., Caron, N. J., Bresolin, M. D. & Tremblay, J. P. In Vivo Migration of Transplanted Myoblasts Requires Matrix Metalloproteinase Activity. *Experimental Cell Research* **258**, 279-287, doi:https://doi.org/10.1006/excr.2000.4962 (2000).

43   Lafreniere, J. F., Mills, P., Tremblay, J. P. & Fahime, E. E. GROWTH FACTORS IMPROVE THE IN VIVO MIGRATION OF HUMAN SKELETAL MYOBLASTS BY MODULATING THEIR ENDOGENOUS PROTEOLYTIC ACTIVITY. *Transplantation* **77**, 1741-1747, doi:10.1097/01.tp.0000131175.60047.eb (2004).

44   González, M. N. *et al.* HGF potentiates extracellular matrix-driven migration of human myoblasts: involvement of matrix metalloproteinases and MAPK/ERK pathway. *Skeletal Muscle* **7**, 20, doi:10.1186/s13395-017-0138-6 (2017).

45   Wolf, K. & Friedl, P. Extracellular matrix determinants of proteolytic and non-proteolytic cell migration. *Trends in Cell Biology* **21**, 736-744, doi:https://doi.org/10.1016/j.tcb.2011.09.006 (2011).

46   Snow, M. H. An autoradiographic study of satellite cell differentiation into regenerating myotubes following transplantation of muscles in young rats. *Cell and tissue research* **186**, 535-540 (1978).

47   Wright, W. E., Sassoon, D. A. & Lin, V. K. Myogenin, a factor regulating myogenesis, has a domain homologous to MyoD. *Cell* **56**, 607-617, doi:https://doi.org/10.1016/0092-8674(89)90583-7 (1989).

48   Mitchell, K. J. *et al.* Identification and characterization of a non-satellite cell muscle resident progenitor during postnatal development. *Nature Cell Biology* **12**, 257, doi:10.1038/ncb2025

https://www.nature.com/articles/ncb2025#supplementary-information (2010).

49   Pannérec, A., Formicola, L., Besson, V., Marazzi, G. & Sassoon, D. A. Defining skeletal muscle resident progenitors and their cell fate potentials. *Development* **140**, 2879-2891 (2013).

50   Saddler, N. I. *et al.* The First Characterization of a Novel Stem Cell Population and the Temporal Relationship with Satellite Cells in Human Skeletal Muscle. *The FASEB Journal* **32**, 615.612-615.612, doi:10.1096/fasebj.2018.32.1_supplement.615.2 (2018).

51   *Handbuch der Lehre von den Geweben des Menschen und der Thiere.* (Wilhelm Engelmann, 1871).

52   Rouget, C. Memoire sur le develloppment, la structure et les propietes physiologiques des capillaries senguins et lymphatiques. *Arch. Physiol. Norm. Pathol.* **5**, 603-663 (1873).

53   Rouget, C. Note sur le developpement de la tunique contractile des vaisseaux. *Compt Rend Acad Sci* **59**, 559-562 (1874).

54   Rouget, C. Sur la contractilite des capillaries sanguins. *CR Acad. Sci. Paris* **88**, 916-918 (1879).

55   Zimmermann, K. W. Der feinere bau der blutcapillaren. *Zeitschrift für Anatomie und Entwicklungsgeschichte* **68**, 29-109 (1923).

56   Esteves, C. & Donadeu, F. Pericytes and their potential in regenerative medicine across species. *Cytometry Part A* **93**, 50-59 (2018).

57   Crisan, M. *et al.* A Perivascular Origin for Mesenchymal Stem Cells in Multiple Human Organs. *Cell Stem Cell* **3**, 301-313, doi:https://doi.org/10.1016/j.stem.2008.07.003 (2008).

58   Dellavalle, A. *et al.* Pericytes of human skeletal muscle are myogenic precursors distinct from satellite cells. *Nature Cell Biology* **9**, 255, doi:10.1038/ncb1542

        https://www.nature.com/articles/ncb1542#supplementary-information (2007).

59   Dellavalle, A. *et al.* Pericytes resident in postnatal skeletal muscle differentiate into muscle fibres and generate satellite cells. *Nature Communications* **2**, 499, doi:10.1038/ncomms1508

        https://www.nature.com/articles/ncomms1508#supplementary-information (2011).

60   Kostallari, E. *et al.* Pericytes in the myovascular niche promote post-natal myofiber growth and satellite cell quiescence. *Development* **142**, 1242-1253 (2015).

61   Cappellari, O. *et al.* Dll4 and PDGF-BB Convert Committed Skeletal Myoblasts to Pericytes without Erasing Their Myogenic Memory. *Developmental Cell* **24**, 586-599, doi:https://doi.org/10.1016/j.devcel.2013.01.022 (2013).

62   Davis, R. L., Weintraub, H. & Lassar, A. B. Expression of a single transfected cDNA converts fibroblasts to myoblasts. *Cell* **51**, 987-1000, doi:https://doi.org/10.1016/0092-8674(87)90585-X (1987).

63   Salvatori, G. *et al.* Myogenic conversion of mammalian fibroblasts induced by differentiating muscle cells. *Journal of cell science* **108**, 2733-2739 (1995).

64   Ito, N., Kii, I., Shimizu, N., Tanaka, H. & Takeda, S. i. Direct reprogramming of fibroblasts into skeletal muscle progenitor cells by transcription factors enriched in undifferentiated subpopulation of satellite cells. *Scientific Reports* **7**, 8097, doi:10.1038/s41598-017-08232-2 (2017).

65   Lattanzi, L. *et al.* High efficiency myogenic conversion of human fibroblasts by adenoviral vector-mediated MyoD gene transfer. An alternative strategy for ex vivo gene therapy of primary myopathies. *The Journal of clinical investigation* **101**, 2119-2128 (1998).

66   Ehrlich, P. R. & Himmelweit, F. *The collected papers of Paul Ehrlich*. Vol. 1 (Pergamon, 1956).

67   Arber, D. A. *et al. Wintrobe's clinical hematology*. (Lippincott Williams & Wilkins, 2013).

68   Tidball, J. G. Inflammatory cell response to acute muscle injury. *Medicine and science in sports and exercise* **27**, 1022-1032 (1995).

69   McLoughlin, T. J., Tsivitse, S. K., Edwards, J. A., Aiken, B. A. & Pizza, F. X. Deferoxamine reduces and nitric oxide synthase inhibition increases neutrophil-mediated myotube injury. *Cell and Tissue Research* **313**, 313-319, doi:10.1007/s00441-003-0767-4 (2003).

70   Pizza, F. X., McLoughlin, T. J., McGregor, S. J., Calomeni, E. P. & Gunning, W. T. Neutrophils injure cultured skeletal myotubes. *American Journal of Physiology-Cell Physiology* **281**, C335-C341 (2001).

71   Dumont, N., Bouchard, P. & Frenette, J. Neutrophil-induced skeletal muscle damage: a calculated and controlled response following hindlimb unloading and reloading. *American Journal of Physiology-Regulatory, Integrative and Comparative Physiology* **295**, R1831-R1838, doi:10.1152/ajpregu.90318.2008 (2008).

72   Legård, G. E. & Pedersen, B. K. in *Muscle and Exercise Physiology*   (ed Jerzy A. Zoladz) 285-307 (Academic Press, 2019).

73   Zhang, Q. *et al.* Circulating mitochondrial DAMPs cause inflammatory responses to injury. *Nature* **464**, 104, doi:10.1038/nature08780

        https://www.nature.com/articles/nature08780#supplementary-information (2010).

74   McDonald, B. *et al.* Intravascular danger signals guide neutrophils to sites of sterile inflammation. *Science* **330**, 362-366 (2010).

75   Dorward, D. A. *et al.* The role of formylated peptides and formyl peptide receptor 1 in governing neutrophil function during acute inflammation. *The American journal of pathology* **185**, 1172-1184 (2015).

76   Maeda, A. & Fadeel, B. Mitochondria released by cells undergoing TNF-α-induced necroptosis act as danger signals. *Cell Death &Amp; Disease* **5**, e1312, doi:10.1038/cddis.2014.277 https://www.nature.com/articles/cddis2014277#supplementary-information (2014).

77   Hazeldine, J., Dinsdale, R. J., Harrison, P. & Lord, J. M. Traumatic Injury and Exposure to Mitochondrial-derived Damage Associated Molecular Patterns Suppresses Neutrophil Extracellular Trap Formation. *Frontiers in Immunology* **10**, 685 (2019).

78   Wasgewatte Wijesinghe, D. K., Mackie, E. J. & Pagel, C. N. Normal inflammation and regeneration of muscle following injury require osteopontin from both muscle and non-muscle cells. *Skeletal Muscle* **9**, 6, doi:10.1186/s13395-019-0190-5 (2019).

79   Lubkin, D. T., Bishawi, M., Barbas, A. S., Brennan, T. V. & Kirk, A. D. Extracellular Mitochondrial DNA and N-Formyl Peptides in Trauma and Critical Illness: A Systematic Review. *Critical Care Medicine* **46**, 2018-2028, doi:10.1097/ccm.0000000000003381 (2018).

80   Nguyen, H. X. & Tidball, J. G. Interactions between neutrophils and macrophages promote macrophage killing of rat muscle cells in vitro. *The Journal of physiology* **547**, 125-132 (2003).

81   Tidball, J. G. Regulation of muscle growth and regeneration by the immune system. *Nature Reviews Immunology* **17**, 165 (2017).

82   Mills, C. D., Kincaid, K., Alt, J. M., Heilman, M. J. & Hill, A. M. M-1/M-2 Macrophages and the Th1/Th2 Paradigm. *The Journal of Immunology* **164**, 6166-6173, doi:10.4049/jimmunol.164.12.6166 (2000).

83   Novak, M. L., Weinheimer-Haus, E. M. & Koh, T. J. Macrophage activation and skeletal muscle healing following traumatic injury. *The Journal of pathology* **232**, 344-355, doi:10.1002/path.4301 (2014).

84   Arnold, L. *et al.* Inflammatory monocytes recruited after skeletal muscle injury switch into antiinflammatory macrophages to support myogenesis. *The Journal of experimental medicine* **204**, 1057-1069, doi:10.1084/jem.20070075 (2007).

85   San Emeterio, C. L., Olingy, C. E., Chu, Y. & Botchwey, E. A. Selective recruitment of non-classical monocytes promotes skeletal muscle repair. *Biomaterials* **117**, 32-43, doi:https://doi.org/10.1016/j.biomaterials.2016.11.021 (2017).

86   Sicari, B. M. *et al.* The promotion of a constructive macrophage phenotype by solubilized extracellular matrix. *Biomaterials* **35**, 8605-8612, doi:https://doi.org/10.1016/j.biomaterials.2014.06.060 (2014).

87   Saclier, M. *et al.* Differentially Activated Macrophages Orchestrate Myogenic Precursor Cell Fate During Human Skeletal Muscle Regeneration. *STEM CELLS* **31**, 384-396, doi:10.1002/stem.1288 (2013).

88   Ceafalan, L. C. *et al.* Skeletal muscle regeneration involves macrophage-myoblast bonding. *Cell Adhesion & Migration* **12**, 228-235, doi:10.1080/19336918.2017.1346774 (2018).

89   Yang, M. *et al.* Microvesicles secreted by macrophages shuttle invasion-potentiating microRNAs into breast cancer cells. *Molecular cancer* **10**, 117 (2011).

90   Nguyen, M.-A. *et al.* Extracellular vesicles secreted by atherogenic macrophages transfer microRNA to inhibit cell migration. *Arteriosclerosis, thrombosis, and vascular biology* **38**, 49-63 (2018).

91   Panduro, M., Benoist, C. & Mathis, D. T$_{reg}$ cells limit IFN-γ production to control macrophage accrual and phenotype during skeletal muscle regeneration. *Proceedings of the National Academy of Sciences* **115**, E2585-E2593, doi:10.1073/pnas.1800618115 (2018).

92   Burzyn, D., Wagers, A., Mathis, D. & Cerletti, M. in *Immunological Tolerance*   229-237 (Springer, 2019).

93   Malecova, B. *et al.* Dynamics of cellular states of fibro-adipogenic progenitors during myogenesis and muscular dystrophy. *Nature Communications* **9**, 3670, doi:10.1038/s41467-018-06068-6 (2018).

94   Fiore, D. *et al.* Pharmacological blockage of fibro/adipogenic progenitor expansion and suppression of regenerative fibrogenesis is associated with impaired skeletal muscle regeneration. *Stem Cell Research* **17**, 161-169, doi:https://doi.org/10.1016/j.scr.2016.06.007 (2016).

95   Lukjanenko, L. *et al.* Aging Disrupts Muscle Stem Cell Function by Impairing Matricellular WISP1 Secretion from Fibro-Adipogenic Progenitors. *Cell Stem Cell* **24**, 433-446.e437, doi:https://doi.org/10.1016/j.stem.2018.12.014 (2019).

96   Guilliams, M. *et al.* Unsupervised High-Dimensional Analysis Aligns Dendritic Cells across Tissues and Species. *Immunity* **45**, 669-684, doi:https://doi.org/10.1016/j.immuni.2016.08.015 (2016).

97   Perdiguero, E., Moiseeva, V. & Muñoz-Cánoves, P. Simultaneous Isolation of Stem and Niche Cells of Skeletal Muscle: Applicability for Aging Studies. (2019).

98   Hurtgen, B. *et al.* Severe muscle trauma triggers heightened and prolonged local musculoskeletal inflammation and impairs adjacent tibia fracture healing. *Journal of musculoskeletal & neuronal interactions* **16**, 122 (2016).

99   Chen, C.-W. *et al.* Human Pericytes for Ischemic Heart Repair. *STEM CELLS* **31**, 305-316, doi:doi:10.1002/stem.1285 (2013).

100   Lopez, J. *et al.* Abstract: Muscle-Derived Stem Cells Are Capable of Transformation into Cells with Schwann Cell-Like Phenotypes. *Plastic and Reconstructive Surgery Global Open* **4**, 69-70, doi:10.1097/01.GOX.0000502957.15888.7b (2016).

101   Shen, M., Tang, W., Cao, Z., Cao, X. & Ding, F. Isolation of rat Schwann cells based on cell sorting. *Molecular medicine reports* **16**, 1747-1752, doi:10.3892/mmr.2017.6777 (2017).

102   Masaki, T. *et al.* Reprogramming Adult Schwann Cells to Stem Cell-like Cells by Leprosy Bacilli Promotes Dissemination of Infection. *Cell* **152**, 51-67, doi:https://doi.org/10.1016/j.cell.2012.12.014 (2013).

103   Rivera, J. C. & Corona, B. T. Muscle-related Disability Following Combat Injury Increases With Time. *US Army Medical Department journal* (2016).

104   Richards, J. T., Overmann, A., Forsberg, J. A. & Potter, B. K. Complications of Combat Blast Injuries and Wounds. *Current Trauma Reports* **4**, 348-358 (2018).

105   Burns, T. C. *et al.* Microbiology and injury characteristics in severe open tibia fractures from combat. *Journal of Trauma and Acute Care Surgery* **72**, 1062-1067 (2012).

106   Johnson, E. N., Burns, T. C., Hayda, R. A., Hospenthal, D. R. & Murray, C. K. Infectious complications of open type III tibial fractures among combat casualties. *Clinical infectious diseases* **45**, 409-415 (2007).

107   Huh, J., Stinner, D. J., Burns, T. C., Hsu, J. R. & Team, L. A. S. Infectious complications and soft tissue injury contribute to late amputation after severe lower extremity trauma. *Journal of Trauma and Acute Care Surgery* **71**, S47-S51 (2011).

108   Murray, C. K. Epidemiology of infections associated with combat-related injuries in Iraq and Afghanistan. *Journal of Trauma and Acute Care Surgery* **64**, S232-S238 (2008).

109   Mazurek, M. T. & Ficke, J. R. The scope of wounds encountered in casualties from the global war on terrorism: from the battlefield to the tertiary treatment facility. *JAAOS-Journal of the American Academy of Orthopaedic Surgeons* **14**, S18-S23 (2006).

110   Weil, Y. A. & Mosheiff, R. in *The Poly-Traumatized Patient with Fractures*   329-342 (Springer, 2016).

111   Mase, V. J. *et al.* Clinical application of an acellular biologic scaffold for surgical repair of a large, traumatic quadriceps femoris muscle defect. *Orthopedics* **33** (2010).

112   Badylak, S., Kokini, K., Tullius, B., Simmons-Byrd, A. & Morff, R. Morphologic Study of Small Intestinal Submucosa as a Body Wall Repair Device. *Journal of Surgical Research* **103**, 190-202, doi:https://doi.org/10.1006/jsre.2001.6349 (2002).

113   Sicari, B. M. *et al.* A murine model of volumetric muscle loss and a regenerative medicine approach for tissue replacement. *Tissue Engineering Part A* **18**, 1941-1948 (2012).

114   Wu, X., Corona, B. T., Chen, X. & Walters, T. J. A standardized rat model of volumetric muscle loss injury for the development of tissue engineering therapies. *BioResearch open access* **1**, 280-290 (2012).

115   Corona, B. T. *et al.* The promotion of a functional fibrosis in skeletal muscle with volumetric muscle loss injury following the transplantation of muscle-ECM. *Biomaterials* **34**, 3324-3335, doi:https://doi.org/10.1016/j.biomaterials.2013.01.061 (2013).

116   Bedair, H. S., Karthikeyan, T., Quintero, A., Li, Y. & Huard, J. Angiotensin II Receptor Blockade Administered after Injury Improves Muscle Regeneration and Decreases Fibrosis in Normal Skeletal Muscle. *The American Journal of Sports Medicine* **36**, 1548-1554, doi:10.1177/0363546508315470 (2008).

117   Burks, T. N. *et al.* Losartan restores skeletal muscle remodeling and protects against disuse atrophy in sarcopenia. *Science translational medicine* **3**, 82ra37-82ra37 (2011).

118   Garg, K., Corona, B. T. & Walters, T. J. Losartan administration reduces fibrosis but hinders functional recovery after volumetric muscle loss injury. *Journal of Applied Physiology* **117**, 1120-1131, doi:10.1152/japplphysiol.00689.2014 (2014).

119   Corona, B. T. *et al.* Autologous minced muscle grafts: a tissue engineering therapy for the volumetric loss of skeletal muscle. *American Journal of Physiology-Cell Physiology* **305**, C761-C775, doi:10.1152/ajpcell.00189.2013 (2013).

120   Ishihara, A. *et al.* Effects of running exercise with increasing loads on tibialis anterior muscle fibres in mice. *Experimental physiology* **87**, 113-116 (2002).

121   Legerlotz, K., Elliott, B., Guillemin, B. & Smith, H. K. Voluntary resistance running wheel activity pattern and skeletal muscle growth in rats. *Experimental physiology* **93**, 754-762 (2008).

122   Garg, K., Ward, C. L., Rathbone, C. R. & Corona, B. T. Transplantation of devitalized muscle scaffolds is insufficient for appreciable de novo muscle fiber regeneration after volumetric muscle loss injury. *Cell and tissue research* **358**, 857-873 (2014).

123   Ward, C. L., Ji, L. & Corona, B. T. An autologous muscle tissue expansion approach for the treatment of volumetric muscle loss. *BioResearch open access* **4**, 198-208 (2015).

124   Corona, B. T., Henderson, B. E. P., Ward, C. L. & Greising, S. M. Contribution of minced muscle graft progenitor cells to muscle fiber formation after volumetric muscle loss injury in wild-type and immune deficient mice. *Physiological reports* **5**, e13249, doi:10.14814/phy2.13249 (2017).

125   Ward, C. L. *et al.* Autologous minced muscle grafts improve muscle strength in a porcine model of volumetric muscle loss injury. *Journal of orthopaedic trauma* **30**, e396-e403 (2016).

126   Gentile, N. E. *et al.* Targeted rehabilitation after extracellular matrix scaffold transplantation for the treatment of volumetric muscle loss. *American journal of physical medicine & rehabilitation* **93**, S79-S87 (2014).

127   Sicari, B. M. *et al.* An acellular biologic scaffold promotes skeletal muscle formation in mice and humans with volumetric muscle loss. *Science translational medicine* **6**, 234ra258-234ra258 (2014).

128   Dziki, J. *et al.* An acellular biologic scaffold treatment for volumetric muscle loss: results of a 13-patient cohort study. *Npj Regenerative Medicine* **1**, 16008, doi:10.1038/npjregenmed.2016.8

       https://www.nature.com/articles/npjregenmed20168#supplementary-information (2016).

129   Han, N. *et al.* Electrodiagnostic evaluation of individuals implanted with extracellular matrix for the treatment of volumetric muscle injury: case series. *Physical therapy* **96**, 540-549 (2016).

130   Aurora, A., Roe, J. L., Corona, B. T. & Walters, T. J. An acellular biologic scaffold does not regenerate appreciable de novo muscle tissue in rat models of volumetric muscle loss injury. *Biomaterials* **67**, 393-407 (2015).

131   Corona, B. T. *et al.* Impact of volumetric muscle loss injury on persistent motoneuron axotomy. *Muscle Nerve* **57**, 799-807, doi:10.1002/mus.26016 (2018).

132   Quarta, M. Volumetric muscle loss: Including nerves into the equation. *Muscle Nerve* **57**, 705-706, doi:10.1002/mus.26080 (2018).

133   Abbott, C. J. *et al.* Imaging axonal transport in the rat visual pathway. *Biomedical optics express* **4**, 364-386, doi:10.1364/BOE.4.000364 (2013).

134   Joseph, K. C., Kim, S. U., Stieber, A. & Gonatas, N. K. Endocytosis of cholera toxin into neuronal GERL. *Proceedings of the National Academy of Sciences of the United States of America* **75**, 2815-2819 (1978).

135   Gonatas, N. K., Stieber, A., Gonatas, J., Mommoi, T. & Fishman, P. H. Endocytosis of exogenous GM1 ganglioside and cholera toxin by neuroblastoma cells. *Molecular and cellular biology* **3**, 91-101 (1983).

136   DENERVATED MUSCLE ATROPHY. *Journal of the American Medical Association* **72**, 348-349, doi:10.1001/jama.1919.02610050030015 (1919).

137   Al-Majed, A. A., Neumann, C. M., Brushart, T. M. & Gordon, T. Brief electrical stimulation promotes the speed and accuracy of motor axonal regeneration. *Journal of Neuroscience* **20**, 2602-2608 (2000).

138   Brushart, T. M. *et al.* Electrical stimulation promotes motoneuron regeneration without increasing its speed or conditioning the neuron. *Journal of Neuroscience* **22**, 6631-6638 (2002).

139   Mendonça, A. C., Barbieri, C. H. & Mazzer, N. Directly applied low intensity direct electric current enhances peripheral nerve regeneration in rats. *Journal of neuroscience methods* **129**, 183-190 (2003).

140   Lu, M.-C. *et al.* Effects of electrical stimulation at different frequencies on regeneration of transected peripheral nerve. *Neurorehabilitation and Neural Repair* **22**, 367-373 (2008).

141   Asensio-Pinilla, E., Udina, E., Jaramillo, J. & Navarro, X. Electrical stimulation combined with exercise increase axonal regeneration after peripheral nerve injury. *Experimental neurology* **219**, 258-265 (2009).

142   Gordon, T., Amirjani, N., Edwards, D. C. & Chan, K. M. Brief post-surgical electrical stimulation accelerates axon regeneration and muscle reinnervation without affecting the functional measures in carpal tunnel syndrome patients. *Experimental Neurology* **223**, 192-202, doi:https://doi.org/10.1016/j.expneurol.2009.09.020 (2010).

143   Barber, B. *et al.* Intraoperative brief electrical stimulation (BES) for prevention of shoulder dysfunction after oncologic neck dissection: study protocol for a randomized controlled trial. *Trials* **16**, 240, doi:10.1186/s13063-015-0745-7 (2015).

144   Wong, J. N., Olson, J. L., Morhart, M. J. & Chan, K. M. Electrical stimulation enhances sensory recovery: a randomized controlled trial. *Annals of neurology* **77**, 996-1006, doi:10.1002/ana.24397 (2015).

145   Wilson, R. D. *et al.* Fully Implantable Peripheral Nerve Stimulation for Hemiplegic Shoulder Pain: A Multi-Site Case Series With Two-Year Follow-Up. *Neuromodulation : journal of the International Neuromodulation Society* **21**, 290-295, doi:10.1111/ner.12726 (2018).

146   Pinheiro-Dardis, C. M., Erbereli, B. T., Gigo-Benato, D., Castro, P. A. T. S. & Russo, T. L. Electrical stimulation delays reinnervation in denervated rat muscle. *Muscle & Nerve* **56**, E108-E118, doi:10.1002/mus.25589 (2017).

147   Willand, M. P., Holmes, M., Bain, J. R., Fahnestock, M. & De Bruin, H. Electrical muscle stimulation after immediate nerve repair reduces muscle atrophy without affecting reinnervation. *Muscle & nerve* **48**, 219-225 (2013).

148   Al-Majed, A. A., Brushart, T. M. & Gordon, T. Electrical stimulation accelerates and increases expression of BDNF and trkB mRNA in regenerating rat femoral motoneurons. *European Journal of Neuroscience* **12**, 4381-4390 (2000).

149   Willand, M. P. *et al.* Electrical muscle stimulation elevates intramuscular BDNF and GDNF mRNA following peripheral nerve injury and repair in rats. *Neuroscience* **334**, 93-104 (2016).

150   English, A. W., Schwartz, G., Meador, W., Sabatier, M. J. & Mulligan, A. Electrical stimulation promotes peripheral axon regeneration by enhanced neuronal neurotrophin signaling. *Developmental neurobiology* **67**, 158-172 (2007).

151   Wenjin, W. *et al.* Electrical stimulation promotes BDNF expression in spinal cord neurons through Ca 2+-and Erk-dependent signaling pathways. *Cellular and molecular neurobiology* **31**, 459-467 (2011).

152   Lin, G. *et al.* Brain-derived neurotrophic factor promotes nerve regeneration by activating the JAK/STAT pathway in Schwann cells. *Translational andrology and urology* **5**, 167-175, doi:10.21037/tau.2016.02.03 (2016).

153   Schmidt, N. *et al.* Long-term delivery of brain-derived neurotrophic factor (BDNF) from nanoporous silica nanoparticles improves the survival of spiral ganglion neurons in vitro. *PLOS ONE* **13**, e0194778, doi:10.1371/journal.pone.0194778 (2018).

154   Pateman, C. J. *et al.* Nerve guides manufactured from photocurable polymers to aid peripheral nerve repair. *Biomaterials* **49**, 77-89 (2015).

155   Gaudin, R. *et al.* Approaches to peripheral nerve repair: generations of biomaterial conduits yielding to replacing autologous nerve grafts in craniomaxillofacial surgery. *BioMed research international* **2016** (2016).

156   Sun, A. X. *et al.* Conduits harnessing spatially controlled cell-secreted neurotrophic factors improve peripheral nerve regeneration. *Biomaterials* **203**, 86-95 (2019).

157   Soucy, J. R., Sani, E. S., Koppes, A. N., Koppes, R. A. & Annabi, N.   (Google Patents, 2019).

158   Nune, M., Subramanian, A., Krishnan, U. M. & Sethuraman, S. Peptide Nanostructures on Nanofibers for Peripheral Nerve Regeneration. *Journal of tissue engineering and regenerative medicine* (2019).

159   Carvalho, C. R., Silva-Correia, J., Oliveira, J. M. & Reis, R. L. Nanotechnology in peripheral nerve repair and reconstruction. *Advanced drug delivery reviews* (2019).

160   Toba, T. *et al.*   (SAGE Publications Sage UK: London, England, 2002).

161   Trevisan, C. *et al.* Allogenic tissue-specific decellularized scaffolds promote long-term muscle innervation and functional recovery in a surgical diaphragmatic hernia model. *Acta Biomaterialia*, doi:https://doi.org/10.1016/j.actbio.2019.03.007 (2019).

162   Rieder, E. *et al.* Early failure of the tissue engineered porcine heart valve SYNERGRAFT® in pediatric patients. *European Journal of Cardio-Thoracic Surgery* **23**, 1002-1006, doi:10.1016/s1010-7940(03)00094-0 (2003).

163   Canavan, H. E., Cheng, X., Graham, D. J., Ratner, B. D. & Castner, D. G. Cell sheet detachment affects the extracellular matrix: A surface science study comparing thermal liftoff, enzymatic, and mechanical methods. *Journal of Biomedical Materials Research Part A* **75A**, 1-13, doi:10.1002/jbm.a.30297 (2005).

164   Xing, Q. *et al.* Decellularization of fibroblast cell sheets for natural extracellular matrix scaffold preparation. *Tissue Engineering Part C: Methods* **21**, 77-87 (2014).

165   Kobayashi, J., Akiyama, Y., Yamato, M., Shimizu, T. & Okano, T. in *Cutting-Edge Enabling Technologies for Regenerative Medicine*   371-393 (Springer, 2018).

166   Yamada, N. *et al.* Thermo-responsive polymeric surfaces; control of attachment and detachment of cultured cells. *Die Makromolekulare Chemie, Rapid Communications* **11**, 571-576 (1990).

167   Akiyama, Y., Kikuchi, A., Yamato, M. & Okano, T. Ultrathin poly (N-isopropylacrylamide) grafted layer on polystyrene surfaces for cell adhesion/detachment control. *Langmuir* **20**, 5506-5511 (2004).

168   Jayapal, K. P., Wlaschin, K. F., Hu, W. & Yap, M. G. Recombinant protein therapeutics from CHO cells-20 years and counting. *Chemical Engineering Progress* **103**, 40 (2007).

169   Knazek, R. A., Gullino, P. M., Kohler, P. O. & Dedrick, R. L. Cell Culture on Artificial Capillaries: An Approach to Tissue Growth in vitro. *Science* **178**, 65-67, doi:10.1126/science.178.4056.65 (1972).

170   Chresand, T. J., Gillies, R. J. & Dale, B. E. Optimum fiber spacing in a hollow fiber bioreactor. *Biotechnology and bioengineering* **32**, 983-992 (1988).

171   Antwiler, G. D., Windmiller, D. A. & Givens, M.   (Google Patents, 2016).

172   Cadwell, J. J. & Barnes, K.   (Google Patents, 2017).

173   Pinxteren, J. A. M. & Craeye, D.   (Google Patents, 2017).

174   Jones, M. E. & Frank, N. D.   (Google Patents, 2017).

175   Cadwell, J. J. Hollow Fibers Enhance Protein Expression: Mammalian Systems Excel in 3D Conditions Provided by Hollow Fiber Bioreactors. *Genetic Engineering & Biotechnology News* **38**, 20-21 (2018).

176   Ku, K., Kuo, M. J., Delente, J., Wildi, B. S. & Feder, J. Development of a hollow-fiber system for large-scale culture of mammalian cells. *Biotechnology and Bioengineering* **23**, 79-95, doi:10.1002/bit.260230107 (1981).

177   Tharakan, J. P. & Chau, P. C. A radial flow hollow fiber bioreactor for the large-scale culture of mammalian cells. *Biotechnology and bioengineering* **28**, 329-342 (1986).

178   Kelsey, L. J., Pillarella, M. R. & Zydney, A. L. Theoretical analysis of convective flow profiels in a hollow-fiber membrane bioreactor. *Chemical Engineering Science* **45**, 3211-3220 (1990).

179   Potter, K. *et al.* Cartilage formation in a hollow fiber bioreactor studied by proton magnetic resonance microscopy. *Matrix Biology* **17**, 513-523 (1998).

180   Piret, J. M. & Cooney, C. L. Model of oxygen transport limitations in hollow fiber bioreactors. *Biotechnology and bioengineering* **37**, 80-92 (1991).

181   Warburg, O. & Minami, S. Versuche an überlebendem carcinom-gewebe. *Journal of Molecular Medicine* **2**, 776-777 (1923).

182   Martin, Y. & Vermette, P. Bioreactors for tissue mass culture: design, characterization, and recent advances. *Biomaterials* **26**, 7481-7503 (2005).

183   Strathmann, H. & Kock, K. The formation mechanism of phase inversion membranes. *Desalination* **21**, 241-255, doi:https://doi.org/10.1016/S0011-9164(00)88244-2 (1977).

184   Tanaka, T. & Lloyd, D. R. Formation of poly(l-lactic acid) microfiltration membranes via thermally induced phase separation. *Journal of Membrane Science* **238**, 65-73, doi:http://dx.doi.org/10.1016/j.memsci.2004.03.020 (2004).

185   Mannella, G. A., Carfì Pavia, F., Conoscenti, G., La Carrubba, V. & Brucato, V. Evidence of mechanisms occurring in thermally induced phase separation of polymeric systems. *Journal of Polymer Science Part B: Polymer Physics* **52**, 979-983, doi:10.1002/polb.23518 (2014).

186   Guillen, G. R., Pan, Y., Li, M. & Hoek, E. M. V. Preparation and Characterization of Membranes Formed by Nonsolvent Induced Phase Separation: A Review. *Industrial & Engineering Chemistry Research* **50**, 3798-3817, doi:10.1021/ie101928r (2011).

187   Berghmans, S., Berghmans, H. & Meijer, H. E. H. Spinning of hollow porous fibres via the TIPS mechanism. *Journal of Membrane Science* **116**, 171-189, doi:http://dx.doi.org/10.1016/0376-7388(96)00037-3 (1996).

188   Ramakrishna, S., Ma, Z. & Matsurra, T. *Polymer Membranes in Biotechnology: Preparation, Functionalization and Application*. 40-41 (2011).

189   Gad, S. C. *Pharmaceutical Manufacturing Handbook: Production and Processes*. 1104-1105 (John Wiley & Sons, 2008).

190   Goldberg, E. *Handbook of Downstream Processing*. 102 (Springer and Science Business Media, 2012).

191   Latulippe, D. R., Ager, K. & Zydney, A. L. Flux-dependent transmission of supercoiled plasmid DNA through ultrafiltration membranes. *Journal of membrane science* **294**, 169-177 (2007).

192   Dey, T. *Nanotechnology for Water Purification*. 181 (Universal Publishers, 2012).

193   Rohani, R., Hyland, M. & Patterson, D. A refined one-filtration method for aqueous based nanofiltration and ultrafiltration membrane molecular weight cut-off determination using polyethylene glycols. *Journal of Membrane Science* **382**, 278-290 (2011).

194   Tung, K.-L. *et al.* Recent advances in the characterization of membrane morphology. *Current Opinion in Chemical Engineering* **4**, 121-127, doi:http://dx.doi.org/10.1016/j.coche.2014.03.002 (2014).

195   Calvo, J. I., Bottino, A., Capannelli, G. & Hernández, A. Comparison of liquid–liquid displacement porosimetry and scanning electron microscopy image analysis to characterise ultrafiltration track-etched membranes. *Journal of Membrane Science* **239**, 189-197, doi:http://dx.doi.org/10.1016/j.memsci.2004.02.038 (2004).

196   Sanz, J. M. *et al.* Characterization of UF membranes by liquid–liquid displacement porosimetry. *Desalination* **245**, 546-553, doi:http://dx.doi.org/10.1016/j.desal.2009.02.019 (2009).

197   Calvo, J. I. *et al.* Liquid–liquid displacement porometry to estimate the molecular weight cut-off of ultrafiltration membranes. *Desalination* **268**, 174-181, doi:http://dx.doi.org/10.1016/j.desal.2010.10.016 (2011).

198   Calvo, J. I. *et al.* in *Encyclopedia of Membrane Science and Technology*   (John Wiley & Sons, Inc., 2013).

199   Brunauer, S., Emmett, P. H. & Teller, E. Adsorption of gases in multimolecular layers. *Journal of the American chemical society* **60**, 309-319 (1938).

200   Sing, K. The use of nitrogen adsorption for the characterisation of porous materials. *Colloids and Surfaces A: Physicochemical and Engineering Aspects* **187-188**, 3-9, doi:https://doi.org/10.1016/S0927-7757(01)00612-4 (2001).

201   Barrett, E., Joyner, L. & Halenda, P. Computations from nitrogen isotherms. *J Am Chem Soc* **73**, 373-380 (1951).

202   Zamani, F. *et al.* Extending the uppermost pore diameter measureable via Evapoporometry. *Journal of Membrane Science* **524**, 637-643 (2017).

203   Kasukonis, B. *et al.* Codelivery of infusion decellularized skeletal muscle with minced muscle autografts improved recovery from volumetric muscle loss injury in a rat model. *Tissue engineering Part A* **22**, 1151-1163 (2016).

Chapter 2

Cell Derived Extracellular Matrix Fibers Synthesized

Using Sacrificial Hollow Fiber Membranes

Submitted as an original article by:

Kevin Roberts[1], Jacob Schluns[2], Addison Walker[2], Jake D. Jones[2], Kyle P .Quinn[2], Jamie Hestekin[3], and Jeffrey C. Wolchok[2]

[1] Cell and Molecular Biology Program, University of Arkansas

[2] Department of Biomedical Engineering, University of Arkansas

[3] Ralph E Martin Department of Chemical Engineering, University of Arkansas

Corresponding Author:

Jeff Wolchok

125 Engineering Hall

Department of Biomedical Engineering

University of Arkansas

Fayetteville, AR 72701

jwolchok@uark.edu

479 575-2850

Abstract

The therapeutic potential of biological scaffolds as adjuncts to synthetic polymers motivates the engineering of fibers formed using the extracellular matrix (ECM) secreted by cells. To capture the ECM secreted by cells during *in vitro* culture, a solvent degradable hollow fiber membrane (HFM) was created and utilized as a cell culture platform. 3T3 fibroblasts were injected into the narrow (0.986 ± 0.042 mm) lumina of mesoporous polysulfone HFMs and maintained in culture for up to three weeks. Following cell culture, HFMs were dissolved using N-methyl-2-pyrrolidone (NMP) and the accumulated ECM was collected. The ECM retained the filamentous dimensions of the HFM lumen. The process yielded up to 0.89 ± 0.20 mg of ECM for every mm of HFM dissolved. Immunofluorescence, second-harmonic generation microscopy, and tandem mass spectrometry indicated the presence of an array of ECM constituents, including collagen, fibronectin, and proteoglycans, while FTIR spectra suggested thorough HFM material dissolution. Isolated ECM fibers, although fragile, were amenable to handling and exhibited an average elastic modulus of 34.6 ± 15.3 kPa, ultimate tensile strength of 5.2 ± 2.2 kPa, and elongation-at-break of $29\% \pm 18\%$. ECM fibers consisted of an interconnected yet porous ($32.7\% \pm 5.8\%$ open space) network which supported the attachment and *in vitro* proliferation of mammalian cells. ECM fibers were similarly synthesized using muscle and astrocyte cells, suggesting process robustness across different cell types. Ultimately, these ECM fibers could be utilized as an alternative to synthetics for the manufacture of woven meshes targeting wound healing or regenerative medicine applications.

A. Introduction

Woven surgical meshes are extensively utilized for the repair of damaged tissues. Each year over 1 million surgical meshes are implanted worldwide[1]. These meshes are typically fabricated using synthetic polymer fibers, the most common being polypropylene. Biomaterial fibers are highly versatile materials that can be woven into a range of implant geometries (meshes, tubes, ropes) using high throughput fabrication methods developed and routinely used by the textiles industry. However, the dramatic rise in the use of surgical meshes has been matched by a similar rise in serious post-surgical complications and product recalls[2-4]. The complications associated with surgical meshes appear to be a direct consequence of the host response to synthetic polymer implants[5]. Specifically, the aggressive foreign body response, characterized by fibrotic tissue formation combined with the chronic activation of immune cells at the site of implantation, appears to be a serious roadblock to clinical success[6]. In fact, the aggressive fibrotic response directed against implanted synthetic materials requires that surgical meshes be applied only where scarring at the site of implantation can be tolerated. For instance, in cases where woven meshes are used to repair hernias the dense scarring response strengthens the repair site[7]. However, for many regenerative applications (muscle, vessel, nerve), the restoration of native tissue structure is the goal, and therefore the disorganized scarring associated with the foreign body response is a severe disadvantage. Ultimately, while fibers have tremendous potential as the raw material for biomedical implants, synthetic polymer fibers are unlikely to find clinical utility for the repair of non-connective tissue types. For cardiac, vascular, nervous, and muscle tissue repair, the need exists for a biomaterial fiber that can be remodeled by the body's own wound healing machinery.

Extracellular matrix (ECM) is a network of biomolecules secreted by all somatic cells of the body which functions as both a physical support for tissues and a reservoir of chemical cues which guide cell differentiation, migration, and tissue remodeling[8]. ECM is noted for its regenerative capacity, with several clinical studies having demonstrated the efficacy of ECM-based grafts for repair of heart, skin, cartilage, and other tissues[9-12]. Of particular relevance to woven meshes, published evidence suggests that fibers containing extracellular matrix (ECM) molecules mute the foreign body reaction and enhance regeneration[13,14]. Specifically, Badylak and colleagues have shown that ECM-coated synthetic meshes reduced the fraction of pro-inflammatory M1 macrophages at the site of implantation and that this change enhanced tissue remodeling. However, while composite ECM/synthetic fibers may delay a foreign body response, they are unlikely to eliminate it completely. As the ECM degrades and the underlying synthetic material interface is exposed to the immune system, a foreign body reaction will eventually be initiated. We suggest that fiber built entirely from ECM -carrying an arsenal of macromolecules relevant to wound-healing-is a logical next step toward the development of whole ECM meshes which may have clinical utility as an adjunct to synthetic polymers.

To create ECM fibers, our group has previously explored methods to farm the ECM secreted by populations of mammalian cells during growth in culture[15,16]. The creation of ECM fibers is predicated by a simple principle; cells have the ability to produce ECM, and the primary challenge is to develop methods to concentrate and collect the molecules that they secrete. Toward this end, we have explored a technique to facilitate the accumulation of cellsecreted molecules using hollow fiber membranes (HFMs) as a cell culture platform. When the lumen is seeded with cells, the semipermeable HFMs trap the large cells and secreted ECM molecules, but permit the exchange of smaller cell culture nutrients. The application of HFM's

for cell culture is not unique by itself, semipermeable HFM's have been used as platforms for the cultivation, implantation, and immuno-isolation of hepatocytes and pancreatic islet cells[17,18]. What is unique is the sacrificial role of the HFM. Rather than being a permanent component, it instead serves as a temporary platform used to capture and collect cell secreted ECM. Once sufficient ECM has been collected, the synthetic HFM can be dissolved, leaving behind only the accumulated ECM which retains the shape of the lumen. In this study, we describe this novel scheme for the production of ECM fibers using sacrificial HFMs as a cell culture platform, and present the characterization results for several key ECM fiber physical and chemical properties.

B. Materials and Methods

Preparation of Hollow Fiber Membranes

Mesoporous polysulfone HFMs were manufactured using a common dry-jet wet spinning method[19] (Table 1). Polysulfone pellets (35kD, Sigma, St. Louis MO) were dissolved in N-methyl-2-pyrrolidone (NMP, 17.8 w/w%) for three days at 25 °C. Polysulfone (PSF) dope solution and a bore solution of NMP in deionized water (15, w/w%) were extruded through a spinneret (AEI) using pressurized N2. Flow of dope and bore solutions from the spinneret into an air gap and subsequent water bath resulted in precipitation of polysulfone fibers by nonsolvent-induced phase separation (Figure. 1). HFMs were stored in deionized water for three days, with water exchanged once per day for removal of residual solvent.

Cell Culture

To facilitate cell culture, HFMs were sterilized in 70% ethanol for 24 hours and incubated in a solution of bovine plasma fibronectin (20 μg/mL) at 37 °C for one hour, after which they were cut using sterile scissors to lengths of 6 cm for cell-seeding. Frozen NIH/3T3 fibroblasts (ATCC, Manassas, VA), suspensions were thawed, seeded into T-175 flasks, and cultured until

confluent in DMEM/F12 containing 10% (w/v) fetal-bovine serum (FBS), 1% L-glutamine, and 1% penicillin-streptomycin. Confluent cultures were disassociated using 0.25% Trypsin-EDTA prior to centrifugation. Pellets were resuspended in DMEM/F12, with cell density counted using a hemocytometer. Cells were seeded into the lumina of HFMs at a density of approximately 20K cells/cm of fiber length using a sterile 21-gauge needle and syringe.

All cell seeded HFMs were cultured for durations of either one or three weeks in DMEM/F12 supplemented 10% (w/v) FBS, 1% L-glutamine, 1% penicillin-streptomycin, 0.285 mM L-ascorbic acid (Sigma), 0.5 mM L-ascorbic acid 2-phosphate (Sigma), and 5 ng/mL human TGF-β1 (Peprotech, Rocky Hill, NJ). At the completion of the culture period, cell-seeded HFMs were dissolved in 99.5% NMP for three days, with NMP exchanged once per day. The remaining cell-derived material (ECM fiber) was collected, rinsed for 48 hours in DI water, and characterized. A subset of HFMs were seeded and cultivated with rat astrocyte and skeletal muscle fibroblast cells to evaluate process robustness across cell types. Astrocyte and muscle cells were harvested via methods approved by the University of Arkansas Institutional Animal Care and Use Committee (IACUC).

Characterization

Transverse cross-sections of naïve polysulfone HFMs were fractured in liquid nitrogen and imaged by SEM to visualize membrane morphology. HFM inner diameter, outer diameter, and wall thickness were measured from microscope images collected from representative samples (n =10). The pore-size distributions of HFMs were determined using evapoporometry and guided by published protocols[20–22]. HFMs were fixed to plastic test cells (n = 3) using an epoxy resin, immersed in 99.5% isopropanol, and mass loss due to evaporation of isopropanol was measured for 24 hours, from which pore-size distributions were calculated using equations

58

described by Krantz et al[22]. Evapoporometry was chosen as the technique for probing pore size in this investigation, as it avoids the application of significant pressure to a sample, is non-destructive, and has been applied successfully toward the analysis of the selective layers of pores between 4 nm to 365 nm in asymmetric membranes, including hollow fiber membranes similar to those produced in this investigation[23, 24].

The effectiveness of the NMP dissolution method was assessed using attenuated total reflectance Fourier transform infrared spectroscopy (ATR-FTIR) with a resolution of 8 cm−1 and a scanning range of 900–1800 cm−1. ATR-FTIR spectra for representative NIH/3T3 derived ECM fibers, cultured polysulfone HFMs, and naive HFMs were analyzed for the presence of sulfonyl groups and aromatics characteristic of polysulfone, as well as protein characteristic amide bands.

In preparation for characterization, NIH/3T3 derived ECM fibers were decellularized using a detergent based protocol[25]. Samples were rinsed for 90 min in Tris-HCL (10mM, pH8.0) with 1% EDTA and 10KU/ml aprotinin 4°C with agitation. Samples were then soaked in 0.1% sodium dodecyl sulphate (SDS) in Tris-HCL buffer for 24 hours at room temperature with agitation. To remove nuclear remnants samples were then incubated for 3 h in reaction buffer containing 50U/mL deoxyribonuclease I and 1U/mL ribonuclease A in 10mM TrisHCl (pH 7.5) at 37°C with agitation. To assess decellularization effectiveness, treated and control samples (n=3/sample group) were fluorescently stained for the presence of the cytoskeletal protein actin using phalloidin (1:40, Sigma). Cells were counterstained with the nuclear reagent DAPI. Representative decellularized material samples were imaged for comparison to cell-containing controls.

Decellularized NIH/3T3 derived ECM fibers were rinsed in deionized water and weighed. Yields were calculated relative to HFM length (mg/mm). Astrocyte and muscle cell derived ECM fiber yield was similarly measured. To examine the internal structure, hydrated NIH/3T3 ECM fiber samples (n=3) were sectioned (7 μm) with the aid of a cryostat (Leica), mounted onto microscopic slides, stained with hematoxylin and eosin and imaged. From the digital images, the porosity (% open area) was calculated from transverse ECM fiber sections with the aid of image analysis software (ImageJ), through subtraction of freehandbounded pore area from total section area and dividing the difference by total section area to yield porosity. To visualize fiber surface features, NIH/3T3 derived fiber samples were frozen, lyophilized, and imaged using scanning electron microscopy (SEM). The SEM imaging of lyophilized samples was motivated by the anticipated use of freeze-drying to prepare materials for storage and implantation.

HFM and decellularized NIH/3T3 ECM fiber mechanical properties were measured with the aid of a uni-axial mechanical testing device (5994, Instron, Norwood, MA) using techniques familiar to our group[16, 26, 27]. Hydrated (PBS, pH = 7.4) samples (gauge length = 1 cm) were deformed at a constant strain rate of 10%/min until failure using a 1N load cell while load and displacement values were recorded at 10 Hz. Prior to testing, sample (n = 4/sample group) fiber diameter was measured using digital calipers. For each sample, engineering stress versus strain curves were generated from load and elongation data. Strain was determined using grip displacement values. From each curve, the tangent modulus was calculated using a linear fit to the region of the stress-strain curve extending from the end of the toe in region, approximately 10% and 0.5% strain for ECM and HFM fibers respectively, to the point of sample failure. The ultimate strength was calculated as the peak stress achieved by each fiber prior to failure.

NIH/3T3 ECM fibers were assessed for the presence of accumulated ECM constituent proteins by immunofluorescence. Representative fibers were immunoreacted for the presence of cellular fibronectin (Mouse IgM, 1:500, Sigma) followed by the appropriate fluorescently labeled secondaries (1:500, Alexafluor, Life Technologies). Samples were counterstained with the nuclear staining reagent DAPI, and then microscopically imaged using an Eclipse Ci-S microscope with D-FL epifluorescence attachment (Nikon, Tokyo, Japan). The accumulation of organized fibrillary collagen within ECM fiber samples was assessed using label free second harmonic generation microscopy (Ultima Investigator, Bruker Inc., Middleton, WI) [25].

NIH/3T3 ECM fiber proteomic composition was further assessed using tandem mass spectrometry (MS/MS). MS/MS was performed with the aid of the University of Arkansas for Medical Sciences proteomics core facility. Samples were hydrated in acetonitrile, digested with trypsin in 100 mM ammonium bicarbonate at 37°C for 12–16 hours. Tryptic peptides were separated by reverse phase Jupiter Proteo resin (Phenomenex) on a 200×0.075 mm column using a nanoAcquity UPLC system (Waters). Eluted peptides were ionized by electrospray (2.15kV) followed by MS/MS analysis using higher-energy collisional dissociation (HCD) on an Orbitrap Fusion Tribrid mass spectrometer (Thermo Scientific, Waltham, MA) in top-speed data-dependent mode. Proteins were identified by comparison to a proteomics database (Mascot, Matrix Science). Scaffold proteomics software was used to verify MS/MS protein identification, with identifications accepted if established with a less than 1% false discovery rate as determined by Scaffold's local FDR algorithm.

A direct contact assay was employed to assess cellular attachment and proliferation upon ECM fiber materials. In preparation for cytotoxicity assays, decellularized NIH/3T3 ECM fibers (approximate length = 1cm) and unmodified glass coverslips (n = 3/sample group) were

sterilized for 24 hours in 70% ethanol. NIH/3T3 cells were seeded onto each sample at a density

of 10 K cells per sample, and cultured in DMEM-F12 with 10% (w/v) FBS, 1% L-glutamine,

and 1% penicillin-streptomycin. Following 72 hours of culture, samples were assayed for cell

viability and death via Calcein AM (2 μM in PBS) and EthD-1 (4μM in PBS), respectively.

Calcein stained ECM fibers were microscopically imaged and assessed for cell coverage.

In vivo host response was examined using a subcutaneous implant site. In vivo

biocompatibility was assayed at 2 and 6 weeks post-implantation time points. Mature male

Sprague Dawley rats (300+g) were used (Envigo, IN). All surgical procedures were performed

in accordance with protocols approved by the University of Arkansas Institutional Animal Care

and Use Committee. Anesthesia was induced using isoflurane (2–4%) in oxygen. The

subcutaneous implant site was surgically exposed through a 2 cm left-right incision placed

caudal to the scapulae. A subcutaneous pouch was created in each animal by blunt dissection. A

single NIH/3T3 ECM sample was implanted into each pouch (approximate implant size 10mm

diameter). Incisions were closed using surgical adhesive (VetBond, 3M). Following surgery all

animals were housed in the University of Arkansas Central Laboratory Animal Facility. At the

prescribed time-points all animals (n=3/ timepoint) were euthanized via inhalation of carbon

dioxide. The implant site with surrounding soft tissue was harvested, fixed in 4%

paraformaldehyde, paraffin embedded, sectioned (10um), and stained with H&E. Stained

sections were imaged and examined for evidence of inflammation and material degradation.

Statistical Methods

All data are represented as mean and standard deviation. The effect of cell type and culture

duration on ECM fiber yield was evaluated with a two-way ANOVA with interaction term. Post

hoc comparisons were made using Tukey's test. A standard 0.05 level of significance was used for all statistical tests.

C. Results

Hollow fiber membranes (HFMs) fabricated by the dry-jet wet spinning technique (Fig. 1) were of the asymmetric type, with selective inner and outer skin layers supported by a highly porous intermediate layer (Figure. 2). Approximately 100 meters of HFM were fabricated from 300 mL of 17.8 w/w% polysulfone in N-methyl-2-pyrrolidone. Evapoporometry analysis of the HFMs revealed a mesoporous pore size distribution, with an average pore diameter of 39.8 nm $\pm$ 3.9 nm. HFM geometry was consistent both within and between batches, with average inner and outer diameters of 0.986 mm $\pm$ 0.042 mm and 1.29 mm $\pm$ 0.038 mm, respectively.

Material harvested from HFMs cultured with NIH/3T3 fibroblasts, rat skeletal muscle fibroblasts (RSMF), and astrocytes was translucent, showed no visual evidence of residual HFM, and exhibited a continuous filament geometry similar to the diameter and length of the HFMs in which they were cultured (Figure. 3). Fibers were amenable to handling and could be woven into a simple crosshatch pattern in a manner consistent with traditional fiber weaving techniques. HFMs cultured with NIH/3T3 cells for three weeks yielded just under one milligram (0.89 $\pm$ 0.2 mg/mm) of ECM fiber for every mm of HFM seeded. Although still capable of producing continuous fibers, both skeletal muscle fibroblasts and astrocyte cells yielded significantly less ECM fiber material (0.44$\pm$ 0.08 and 0.41$\pm$ 0.04 mg/mm respectively). ECM fiber yield was sensitive to culture duration. 3T3 cells exhibited a 4- fold increase in ECM yield for three weeks versus one week of culture (p = 0.0134). Corresponding increases in yield for skeletal muscle fibroblasts and astrocytes were 2- fold (p = 0.6965) and 4-fold (p= 0.5316), respectively.

Transverse and longitudinal sections of NIH/3T3 ECM fibers (7 μm thickness) revealed a porous yet interconnected network of eosin stained ECM (Figure. 4). ECM fibers exhibited open-cell pores distributed irregularly throughout the sections. Analysis of transverse sections indicated an average interior ECM fiber porosity of 32.7% ± 5.8%. SEM images of lyophilized NIH/3T3 ECM fibers revealed a dense surface skin with a rough filamentous texture that is consistent with the appearance of native tissue ECM. The surface skin also showed evidence of fibril alignment along the longitudinal axis of the ECM fiber. Residual HFM material was not observed.

ATR-FTIR spectra of NIH/3T3 ECM fibers revealed strong absorbance at 1650 cm−1 and 1540 cm−1, consistent with the amide I and II absorbance bands characteristic of proteins (Figure 5)[28]. Comparison of the spectra of isolated ECM fibers to the spectra of cultured and uncultured polysulfone HFMs indicated that the characteristic polysulfone absorbance peaks (1580, 1480, 1236, and 1150 cm−1) were not present in the ECM fiber samples, suggesting effective dissolution of the polysulfone HFM via NMP incubation.

Mechanical testing of HFMs (Figure 6) yielded an average elastic modulus of 10.0 MPa ± 1.82 MPa and an average ultimate strength of 0.717 MPa ± 0.124 MPa. Stress-strain curves for HFMs exhibited linear elastic regions followed by small plastic regions and sharp failure. HFMs stretched to an average of strain of 13% prior to failure. Stress-strain curves for decellularized NIH/3T3 ECM fibers consistently exhibited toe-in regions, typically extending out to 10%, followed by a near linear increase in stress until failure. No significant plastic region was observed. The average elastic modulus and ultimate strength for ECM fibers measured within the linear region were 34.6 ± 15.3 kPa and 5.2 ± 2.2 kPa respectively. On

average, ECM fibers stretched 29% ± 18% in length before failure. The accumulated ECM fibers were notably less stiff and more extensible than the once present HFM scaffolds.

Isolated NIH/3T3 ECM fibers were strongly reactive to antibodies directed against fibronectin (Figure 7). Second harmonic generation imaging also indicated the presence of fibrillary collagen throughout the ECM fibers. MS/MS proteomic analysis identified an array of ECM structural components (Table 2), including collagen I, III, VI, XVIII, fibronectin, fibrillin 1, fibulin 1 and 2, and prolargin. Several matricellular proteins were also present, including EFEMP 1 and 2, thrombospondin 1 and 2, tenascin, and periostin. A complement of proteoglycans was identified as well, including biglycan, decorin, glypican 1 and 6, and versican. Pre-decellularization samples were strongly reactive to phalloidin and DAPI staining, while post-decellularization samples exhibited no specific staining. The gross appearance and handling of ECM fibers was not significantly altered by decellularization, as fibers remained continuous and amenable to handling. When reseeded with cells, the NIH/3T3 ECM fibers supported the attachment and recultivation of NIH/3T3 fibroblasts. Calcein AM staining directed against NIH/3T3 cells indicated that viable cells were distributed densely across the surface of the cultured fibers, reaching confluency within 72 hours (Figure 8). EthD-1 staining indicated a negligible quantity of non-viable cells. No pre-culture treatments (e.g. incubation with fibronectin) were required for adhesion of cells to the ECM fibers.

All implanted animals tolerated the implantation surgery well and gained weight throughout the observation period at a rate (8±2 grams/week) that was not significantly different from un-implanted controls (9±2 grams/week). At 2 weeks post implantation, samples were well incorporated into the surrounding tissue and host cells had densely penetrated the material (Figure 8). There was no evidence of a dense fibrous encapsulation layer surrounding the

implants, nor a necrotic region within it. By 6 weeks post implantation, implant sites showed evidence of elevated cellularity, but it was sharply reduced when compared to 2 week samples, suggesting ongoing implant degradation. There was no evidence of local toxicity nor was there any evidence of multinuclear giant cell formation in regions surrounding the implants at either timepoint.

D. Discussion

In this study, we have developed a process for extracting whole threads of ECM secreted by cells cultured in the lumina of sacrificial HFMs. Our findings suggest that this HFM culture approach is amenable toward the production of filaments of ECM from several cell types, and that these filaments have a composition and structure that may find utility for the repair of fibrous tissues in the form of a surgical mesh. The operating principle of the sacrificial HFM culture method is that ECM produced by cells cultured in the lumina of HFM's can be captured and concentrated by preventing cross-membrane transport of ECM constituents. To our knowledge, this study represents the first time in literature that culture of cells in the lumen of HFMs has been leveraged for the production and extraction of ECM. Evapoporometry data indicate that the pores of the membranes fabricated in this study are substantially smaller than the hydrodynamic radii for ECM components such as collagen I (>80 nm at 37 °C)[29, 30] or high molecular weight hyaluronan (103 nm for mW = 2000 kDa)[31], indicating that these constituents are unlikely to diffuse across the membrane, driving ECM to accumulate in the lumina of the HFMs. Conversely, the small hydrodynamic radii of cell medium constituents such as bovine serum albumin (3.48 nm)[32] suggests that they can diffuse across the membrane wall unimpeded. While an in-depth study of ECM bioseparation was beyond the scope of this investigation, the pore diameter distributions of HFMs, being tunable during the spinning process, may allow for

66

selective retention of desirable ECM constituents such as high molecular weight hyaluronan

(anti-inflammatory) while permeating others (e.g., pro-inflammatory low mW hyaluronan)[33]

Incorporation of ECM components into a fiber geometry is not entirely without precedent.

Alberti and Xu used sheets of decellularized tendon to form fiber-like collagen constructs[34];

another notable advance was made by Onoe et al, wherein hydrogels treated with individual

ECM proteins were seeded with various cell lines to generate long fibers with encapsulated

cells[35]; however, the scaffolding material, being composed of a hydrogel treated with individual

ECM proteins, does not approximate the multimolecular nature of ECM. Past investigations

have demonstrated that subtle aspects of ECM composition play an important role in tissue

regeneration. For example, heparan sulfate proteoglycans (HSPGs) are known to be necessary

for FGF-2 signaling which regulates angiogenesis and the proliferation of satellite cells during

myogenesis[36]. Further, the combination of glycosaminoglycans and structural proteins in

biomaterials have been shown to improve primary muscle cell proliferation, myoblast fusion,

and skin regeneration, as well as bone formation in vivo[37–40]. The literature at large therefore

suggests that the inclusion of an array of key ECM constituents in scaffolds bears clinical

relevance for the regeneration of a range of tissues.

Our data suggest that the ECM fibers isolated in this study are bio-complex;

immunoreaction of ECM fibers with antibodies for key ECM constituents, second-harmonic

generation microscopy, and tandem mass spectrometry appear to demonstrate the

multimolecular nature of this material. Several of the ECM constituents identified in ECM

fibers are critical elements for the regeneration of a broad range of tissues including skeletal

muscle, a target of interest for our group[41]. The fibril- forming collagens I and III found in ECM

fibers are the predominant collagens in skin tendon, bone, and skeletal muscle, and collagen VI

is an important component of the basement membrane surrounding skeletal muscle[42]. Biglycan and decorin, implicated in cutaneous wound healing and key regulators of collagen organization in skeletal muscle-were also identified[43, 44]. Further, some notable secreted factors were present in ECM fibers, including HDGF, IGF-II, and PEDF, playing various roles in liver, bone, and peripheral nerve regeneration[45–48]. While detergent-based decellularization techniques tend to remove various elements of ECM scaffolds, an array of alternative methods exist which may better preserve glycosaminoglycan and growth factor content[49].

Delivery of therapeutic cells for wound-healing, especially progenitor cells, shows unique promise, as their inclusion into implants can promote angiogenesis[50] and diminish the foreign body response to a biomaterial through the downregulation of pro-inflammatory cytokine expression[51]. This, however, presents challenges to scaffold design; the scaffold must obviously exhibit minimum cytotoxicity, but also have properties that serve to retain the desired phenotype of the carried cells, as the absence of cues provided in cell culture may cause them to lose desired characteristics in vivo. It has been observed that cells cultured on substrates coated with tissue-specific ECM better retain their differentiated phenotypes, and that progenitor cells exhibit improved proliferation and retention of differentiation potential on these materials[52, 53]. This suggests that scaffolds composed of whole ECM may find applicability as carriers of therapeutic cells. Although cytocompatibility was not examined with progenitor cells, the ECM fibers produced in this study contain key cell attachment proteins and were supportive of NIH/3T3 cell cultivation, with rapid proliferation leading to confluency in 72 hours and negligible cell death. When taken as a whole, the ECM fibers appear to have desirable cell adhesive properties that could be leveraged to deliver a range of attachment dependent cells. Furthermore, while NMP has known systemic and local toxicity at low concentrations[54, 55], the

in vivo and *in vitro* biocompatibility testing results indicate that the solvent can be washed from the ECM samples prior to implantation.

One of the recognized limitations of first generation ECM fibers is their modest yield and strength when compared to both synthetic polymers and native tissue ECM. To address this shortcoming, next generation fabrication approaches could draw from the rich repertoire of cell culture techniques known to influence in vitro ECM production. Among these, media supplementation with cytokines possessing known ECM stimulatory properties would appear to be a logical first approach. HFM's can be designed with pore diameters that allow the transport of cytokines including, HGF, VEGF, and CTGF into the lumen, while still trapping the larger structural proteins of interest. In addition to cytokines, the addition of crowding-inducing compounds such as dextran sulfate or Ficoll in culture medium has previously been exploited to increase in vitro ECM deposition and organization and may provide a unique synthetic approach toward enhancement of ECM fiber yield[56, 57]. Alternatively the cell itself could be manipulated to modulate ECM production. Recently developed CRISPR/Cas9 gene editing techniques[58, 59] may provide a pathway for the production of "designer" cells with targeted ECM production capabilities. For example, the removal of collagen type I genes may create a cell with enhanced collagen type III production. Similar "knock in" gene editing techniques could be used to selectively increase ECM production[60].

In addition to their use in woven implants, ECM fibers could potentially find utility as the print material in 3-D bio-printing systems[61, 62]. The most common type of printing method, fused deposition, utilizes long filaments to build up an object of interest. We could envision a system in which the synthetic fibers are replaced by ECM fibers, which are then used to print organs and tissues. Furthermore, similar in concept to the various synthetic polymer chemistries

available with traditional 3-D printing systems, it may be possible to print using an assortment of ECM fibers synthesized using vascular, nerve, and cardiac cells. The data presented in this study demonstrate that ECM fibers are producible across several cell types, including 3T3 fibroblasts, rat skeletal muscle fibroblasts, and astrocytes. While differences in ECM fiber composition between each of these cell types were not explored, it is known that the in-vitro production of ECM does vary by cell types. Variations in ECM production between cell types could be exploited to create a pallet ECM fibers with varying compositions. Using such a system, it may be possible to bio-print tissues and organs with heterogeneous structures and compositions (e.g. vascular fibers embedded within dermal fibers). A further benefit of this platform is that human cells could be leveraged for the production of allogeneic grafts while autologous implants could be produced by isolating and culturing the patient's own cells. While impractical for the rapid treatment of acute injuries, patient specific implants may be applicable for the treatment of chronic injuries.

E. Conclusions

The results of this study suggest that:

1. Hollow fiber membrane cell culture is applicable toward the production of continuous threads of ECM.

2. ECM fibers are amenable to handling and can be assembled into multi-fiber meshes.

3. Isolated ECM fibers exhibit a diverse complement of fibrous ECM proteins, proteoglycans, and matricellular factors.

4. ECM fibers support the in-vitro cultivation of fibroblasts and are well tolerated by the host following implantation.

F. Acknowledgements

References

1   Cobb W S, Kercher K W and Heniford B T 2005 The argument for lightweight
       polypropylene mesh in hernia repair Surg. Innov. 12 63–9

2   Lee D et al 2013 Transvaginal mesh kits—how 'serious' are the complications and are
       they reversible? Urology 81 43–8

3   Nosti P A and Iglesia C B 2013 Medicolegal issues surrounding devices and mesh for
       surgical treatment of prolapse and incontinence Clin. Obstet. Gynecol. 56 221–8

4   Unger C A and Barber M D 2015 Vaginal mesh in pelvic reconstructive surgery:
       controversies, current use, and complications Clin. Obstet. Gynecol. 58 740–53

5   Klinge U et al 1999 Foreign body reaction to meshes used for the repair of abdominal
       wall hernias Eur. J. Surg. 165 665–73

6   Williams D F 2008 On the mechanisms of biocompatibility Biomaterials 29 2941–53

7   Ibrahim A M et al 2015 Properties of meshes used in hernia repair: a comprehensive
       review of synthetic and biologic meshes J. Reconstr. Microsurg. 31 83–94

8   Swinehart I T and Badylak S F 2016 Extracellular matrix bioscaffolds in tissue
       remodeling and morphogenesis Dev. Dyn. 245 351–60

9   Barber F A et al 2012 A prospective, randomized evaluation of acellular human dermal
       matrix augmentation for arthroscopic rotator cuff repair Arthroscopy: J. Arthroscopic
       Relat. Surg. 28 8–15

10   Holubec T et al 2015 The use of extracellular matrix patches in cardiac surgery J. Cardiac
       Surg. 30 145–8

11   Juhasz I et al 2010 Long-term followup of dermal substitution with acellular dermal
       implant in burns and postburn scar corrections Dermatol. Res. Pract. 2010 7

12   Mostow E N et al 2005 Effectiveness of an extracellular matrix graft (OASIS Wound
       Matrix) in the treatment of chronic leg ulcers: a randomized clinical trial J. Vasc. Surg. 41
       837–43

13   Faulk D M et al 2014 ECM hydrogel coating mitigates the chronic inflammatory response
       to polypropylene mesh Biomaterials 35 8585–95

14   Wolf M T et al 2014 Macrophage polarization in response to ECM coated polypropylene
       mesh Biomaterials 35 6838–49

15   Hurd S A et al 2015 Development of a biological scaffold engineered using the extracellular matrix secreted by skeletal muscle cells Biomaterials 49 9–17

16   Wolchok J C and Tresco P A 2010 The isolation of cell derived extracellular matrix constructs using sacrificial open-cell foams Biomaterials 31 9595–603

17   Ahmed H M M et al 2017 3D liver membrane system by co-culturing human hepatocytes, sinusoidal endothelial and stellate cells Biofabrication 9 025022

18   Teotia R S et al 2017 Islet encapsulated implantable composite hollow fiber membrane based device: a bioartificial pancreas Mater. Sci. Eng. C 77 857–66

19   Wang L K et al 2010 Membrane and Desalination Technologies (New York: Springer)

20   Akhondi E et al 2014 Evapoporometry determination of pore-size distribution and pore fouling of hollow fiber membranes J. Membr. Sci. 470 334–45

21   Akhondi E et al 2015 Improved design and protocol for evapoporometry determination of the pore-size distribution J. Membr. Sci. 496 334–43

22   Krantz W B et al 2013 Evapoporometry: a novel technique for determining the pore-size distribution of membranes J. Membr. Sci. 438 153–66

23   Zamani F et al 2017 Evapoporometry adaptation to determine the lumen-side pore-size distribution (PSD) of hollow fiber and tubular membranes J. Membr. Sci. 526 1–8

24   Zamani F et al 2017 Extending the uppermost pore diameter measureable via evapoporometry J. Membr. Sci. 524 637–43

25   Mirsadraee S et al 2006 Development and characterization of an acellular human pericardial matrix for tissue engineering Tissue Eng. 12 763–73

26   Lasher R A et al 2010 Design and characterization of a modified T-flask bioreactor for continuous monitoring of engineered tissue stiffness Biotechnol. Prog. 26 857–64

27   Wolchok J C et al 2009 The effect of bioreactor induced vibrational stimulation on extracellular matrix production from human derived fibroblasts Biomaterials 30 327–35

28   Kong J and Yu S 2007 Fourier transform infrared spectroscopic analysis of protein secondary structures Acta Biochim. Biophys. Sin. 39 549–59

29   Liu Y et al 2013 Double thermal transitions of type I collagen in acidic solution J. Biomol. Struct. Dyn. 31 862–73

30   Mu C et al 2007 Temperature induced denaturation of collagen in acidic solution Biopolymers 86 282–7

31   Coleman P J et al 2000 Role of hyaluronan chain length in buffering interstitial flow a cross synovium in rabbits J. Physiol. 526 425–34

32   Axelsson I 1978 Characterization of proteins and other macromolecules by agarose gel chromatography J. Chromatogr. A 152 21–32

33   Petrey A C and de la Motte C A 2014 Hyaluronan, a crucial regulator of inflammation Frontiers Immunol. 5 101

34   Alberti K A and Xu Q 2013 Slicing, stacking and rolling: fabrication of nanostructured collagen constructs from tendon sections Adv. Healthc. Mater. 2 817–21

35   Onoe H et al 2013 Metre-long cell-laden microfibres exhibit tissue morphologies and functions Nat. Mater. 12 584–90

36   Yablonka-Reuveni Z and Rivera A J 1997 Proliferative dynamics and the role of FGF2 during myogenesis of rat satellite cells on isolated fibers Basic Appl. Myol. 7 189–202 PMID: 26052220

37   Rønning S B et al 2013 The combination of glycosaminoglycans and fibrous proteins improves cell proliferation and early differentiation of bovine primary skeletal muscle cells Differentiation 86 13–22

38   Salbach J et al 2012 Regenerative potential of glycosaminoglycans for skin and bone J. Mol. Med. 90 625–35

39   Scuderi N et al 2009 Clinical application of autologous three-cellular cultured skin substitutes based on esterified hyaluronic acid scaffold: our experience In Vivo 23 991–1003

40   Stadlinger B et al 2008 Effect of biological implant surface coatings on bone formation, applying collagen, proteoglycans, glycosaminoglycans and growth factors J. Mater. Sci., Mater. Med. 19 1043–9

41   Ten Broek R W, Grefte S and Von den Hoff J W 2010 Regulatory factors and cell populations involved in skeletal muscle regeneration J. Cell Physiol. 224 7–16

42   Lampe A and Bushby K 2005 Collagen VI related muscle disorders J. Med. Genet. 42 673–85

43   Gillies A R and Lieber R L 2011 Structure and function of the skeletal muscle extracellular matrix Muscle Nerve 44 318–31

44   Jarvelainen H et al 2006 A role for decorin in cutaneous wound healing and angiogenesis Wound Repair Regen. 14 443–52

45   Conover C A et al 2002 Subcutaneous administration of insulin-like growth factor (IGF)-II/IGF binding protein-2 complex stimulates bone formation and prevents loss of bone mineral density in a rat model of disuse osteoporosis Growth Horm. IGF Res. 12 178–83

46   Enomoto H et al 2009 Hepatoma-derived growth factor is induced in liver regeneration Hepatol Res. 39 988–97

47   Erbay E et al 2003 IGF-II transcription in skeletal myogenesis is controlled by mTOR and nutrients J. Cell Biol. 163 931–6

48   Ho T C et al 2015 PEDF-derived peptide promotes skeletal muscle regeneration through its mitogenic effect on muscle progenitor cells Am. J. Physiol. Cell Physiol. 309 C159–68

49   Gilbert T W, Sellaro T L and Badylak S F 2006 Decellularization of tissues and organs Biomaterials 27 3675–83

50   Leeper N J, Hunter A L and Cooke J P 2010 Stem cell therapy for vascular regeneration: adult, embryonic, induced pluripotent stem cells Circulation 122 517–26

51   Swartzlander M D et al 2015 Immunomodulation by mesenchymal stem cells combats the foreign body response to cell-laden synthetic hydrogels Biomaterials 41 79–88

52   Xiong Y et al 2015 Retention of the stemness of mouse adipose-derived stem cells by their expansion on human bone marrow stromal cell-derived extracellular matrix Tissue Eng. A 21 1886–94

53   Zhang Y et al 2009 Tissue-specific extracellular matrix coatings for the promotion of cell proliferation and maintenance of cell phenotype Biomaterials 30 4021–8

54   Malek D E et al 1997 Repeated dose toxicity study (28 days) in rats and mice with N-methylpyrrolidone (NMP) Drug Chem. Toxicol. 20 63–77

55   Solomon H M et al 1995 1-Methyl-2-pyrrolidone (NMP): reproductive and developmental toxicity study by inhalation in the rat Drug Chem. Toxicol. 18 271–93

56   Chen C et al 2011 Applying macromolecular crowding to enhance extracellular matrix deposition and its remodeling in vitro for tissue engineering and cell-based therapies Adv. Drug. Deliv. Rev. 63 277–90

57   Chen C Z et al 2009 The Scar-in-a-Jar: studying potential antifibrotic compounds from the epigenetic to extracellular level in a single well Br. J. Pharmacol. 158 1196–209

58   Peng Y et al 2014 Making designer mutants in model organisms Development 141 4042–54

59   Riordan S M et al 2015 Application of CRISPR/Cas9 for biomedical discoveries Cell
       Biosci. 5 33

60   Wang B et al 2015 Highly efficient CRISPR/HDR-mediated knock-in for mouse
       embryonic stem cells and zygotes Biotechniques 59 201–8

61   Chia H N and Wu B M 2015 Recent advances in 3D printing of biomaterials J. Biol. Eng.
       9 4

62   Ker E D et al 2011 Bioprinting of growth factors onto aligned sub-micron fibrous
       scaffolds for simultaneous control of cell differentiation and alignment Biomaterials 32
       8097–107

G. Appendix

Figure Legend:

Figure 1: Hollow Fiber Membrane Fabrication

Hollow fiber membranes were fabricated using a custom-built dry-jet wet spinning system (A). Polymer and solvent solutions were extruded by pressurized N2 through an annulus and needle internal to a spinneret. Solutions exiting the spinneret (B: arrow) begin to form a nascent hollow fiber membrane by non-solvent induced phase separation via contact with the water bath. Following precipitation, membranes were collected on a motorized take-up wheel (C) at a rate of 2.2 meters per minute, producing 100 meters of membrane in 45 minutes.

Figure 2: Membrane Structure and Pore Size Distribution

Transverse SEM micrographs (A and B) of representative HFF's show a concentric asymmetric membrane with interior and exterior skin layers harboring finger-like pores. Evapoporometric determination of the membranes' pore diameter distribution (mean = 39.8 nm ± 3.9 SD, n = 3) revealed a mesoporous distribution of pores with sizes large enough to permit nutrient transport, but small enough to trap large structural proteins within the HFM lumen.

Figure 3: ECM Fiber Capture, Manipulation, and Yield

Following one or three weeks in culture, cell seeded hollow fiber membranes were (A) dissolved in NMP and the accumulated ECM was collected (green). Cell derived material isolated following dissolution (B) was formed into a continuous filament that could be manipulated into a conceptual weave (C). ECM fibers were collected from all cells types tested. ECM yield (D) was sensitive to both cell type and culture duration. Levels not connected by same letter are significantly different ($p < 0.05$, ANOVA with post hoc Tukey's test).

Figure 4: ECM Fiber Structure

Representative H&E stained images of transverse (A) and longitudinal (B) ECM fiber thin sections (thickness = 7 µm) reveals the porous yet interconnect network of accumulated ECM. SEM micrographs (C and D) of ECM fibers (50x and 1000x, respectively) illustrate the fibers irregular surface with fibrillar features that are suggestive of ECM.

Figure 5: ATR-FTIR Analysis

ATR-FTIR spectra for (a) NIH/3T3-derived ECM fibers, (b) polysulfone HFMs cultured with NIH/3T3 cells for 3 weeks, and (c) uncultured naïve polysulfone HFM were captured using a Spectrum BX FTIR spectrometer with an ATR accessory and a scanning resolution of 8 cm^{-1}. Isolated ECM fibers exhibit strong absorbance in the protein-indicative amide bands, with negligible absorbance for the bands characteristic of polysulfone.

Figure 6: Membrane and ECM Fiber Tensile Properties

Representative HFM stress-strain curve (A), elastic modulus (B) and ultimate strength (C) values for mechanical tested (tensile) HFM samples (mean + SD, n = 3), with representative stress-strain curve (D), elastic modulus (E) and ultimate strength (F) for mechanically tested ECM fibers (mean + SD, n = 3). ECM fiber stress-strain curves were characterized by a toe in region followed by a near linear rise in stress until failure.

Figure 7: ECM Fiber Immunofluorescence and Decellularization

ECM fibers samples were immuno-stained to detect the presence of fibronectin (A), a key cell adhesive protein. Imaging via second--harmonic generation was utilized to detect the presence of fibrillar collagens, key structural proteins. ECM fibers were strongly reactive to both. Nucleus and actin staining of control (C and E) and decellularized ECM fibers (D and F) was used to examine process effectiveness. The SDS based decellularization process appeared to effectively remove cellular debris from ECM fibers without disrupting the continuity of the fibers.

Figure 8: Biocompatibility

Calcein AM cell viability staining of NIH/3T3 fibroblasts seeded and cultured on an isolated ECM fiber for 72 hours. Viable cells were attached to and densely distributed across the surface of the ECM fibers. Stained (H&E) thin sections collected from ECM implanted in Sprague Dawley rats at 2 (B) and 6 weeks (C). Increased cellularity observed within the dorsal subcutaneous implantation site at 2 weeks (*) is largely resolved by 6 weeks (n = 3/timepoint). Scale bar 100 µm unless noted.
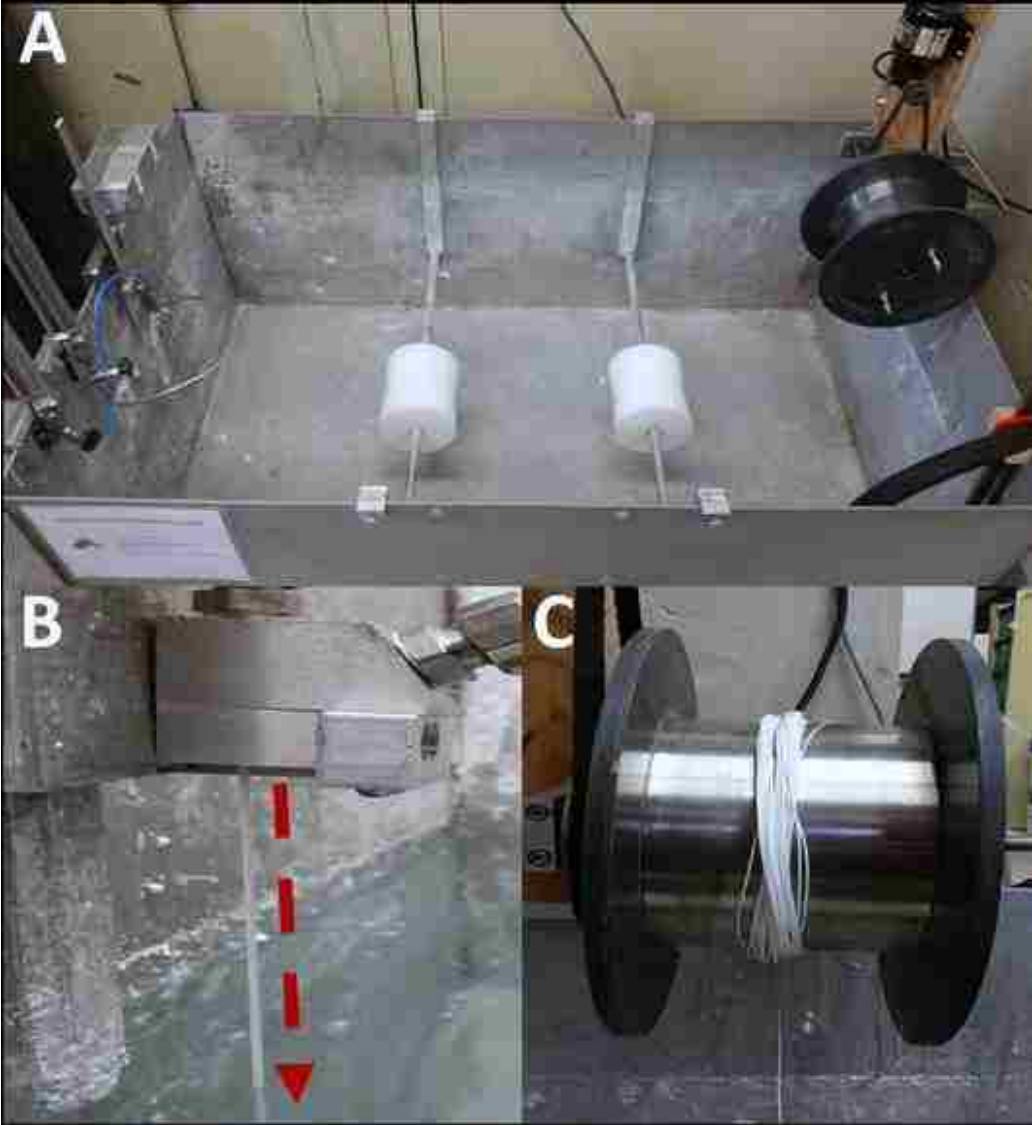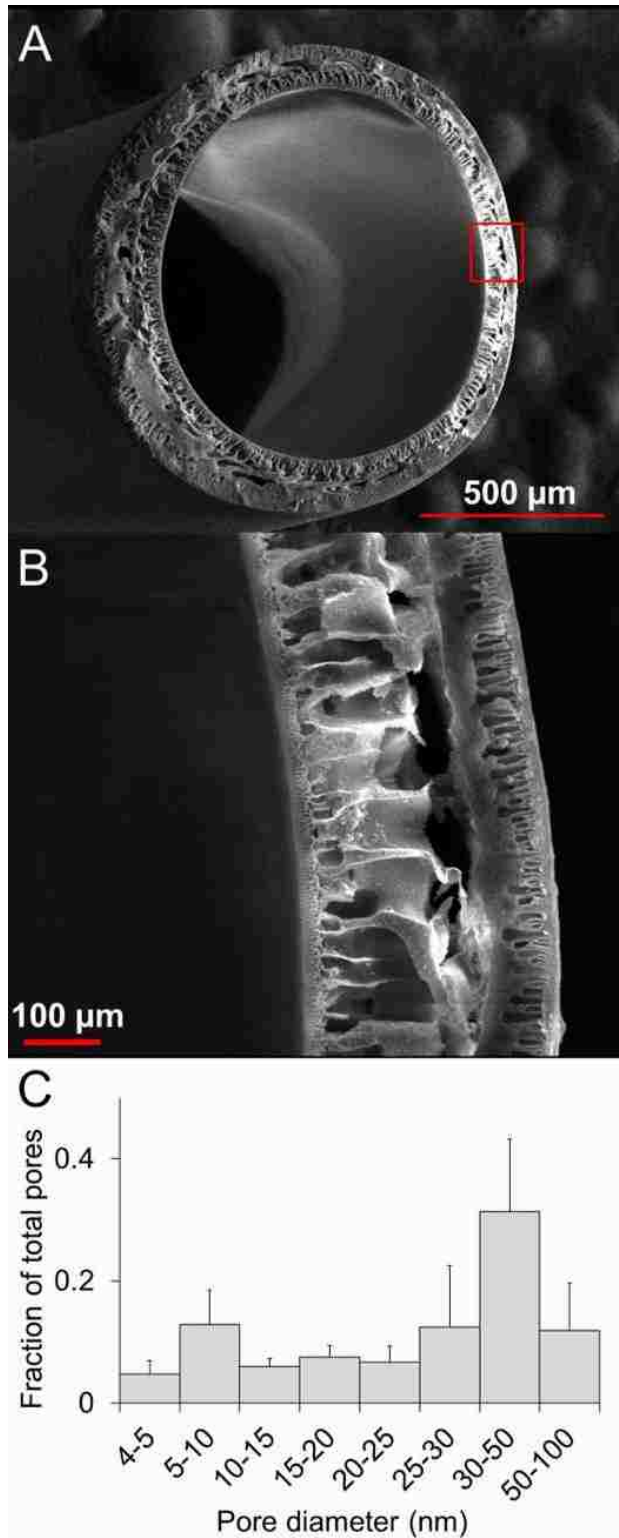
Figures

Figure 1

Figure 2

Figure 3

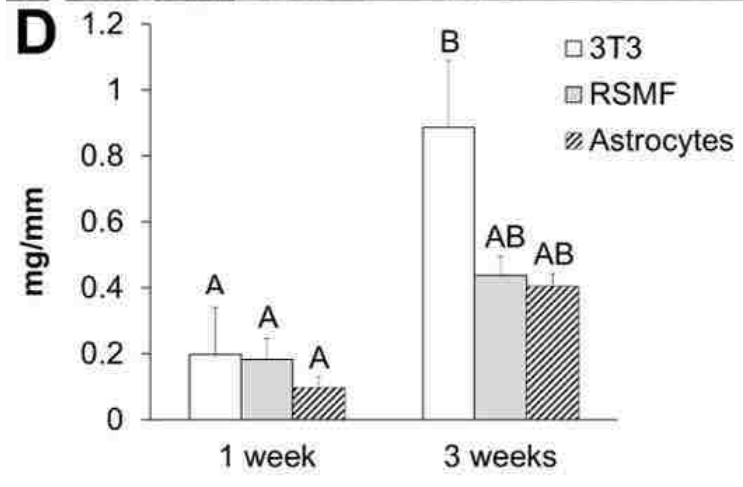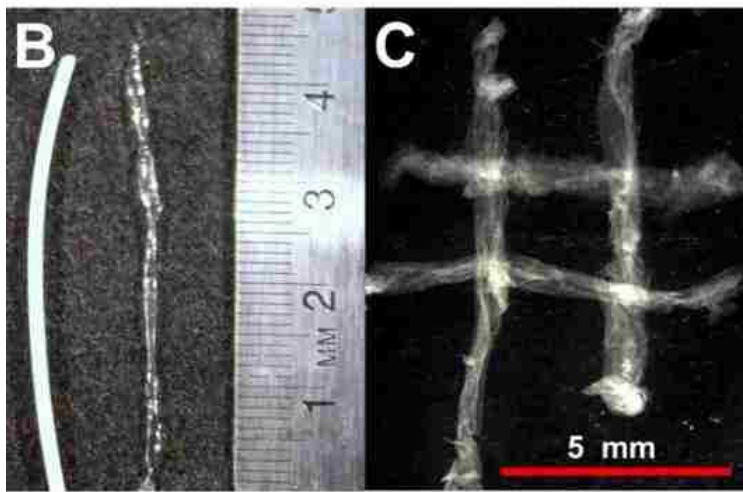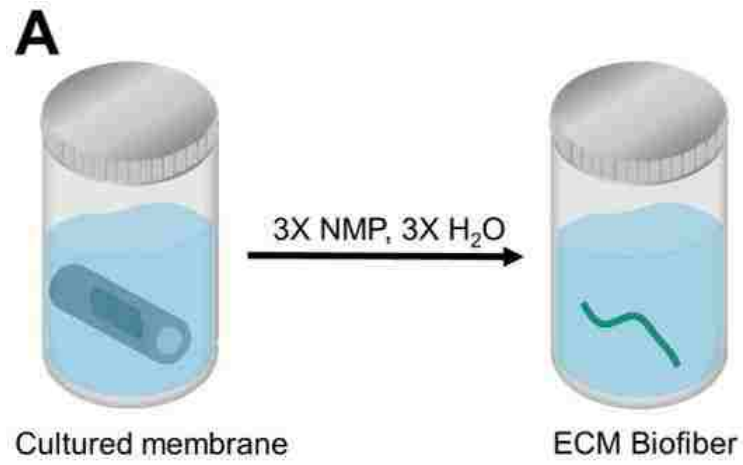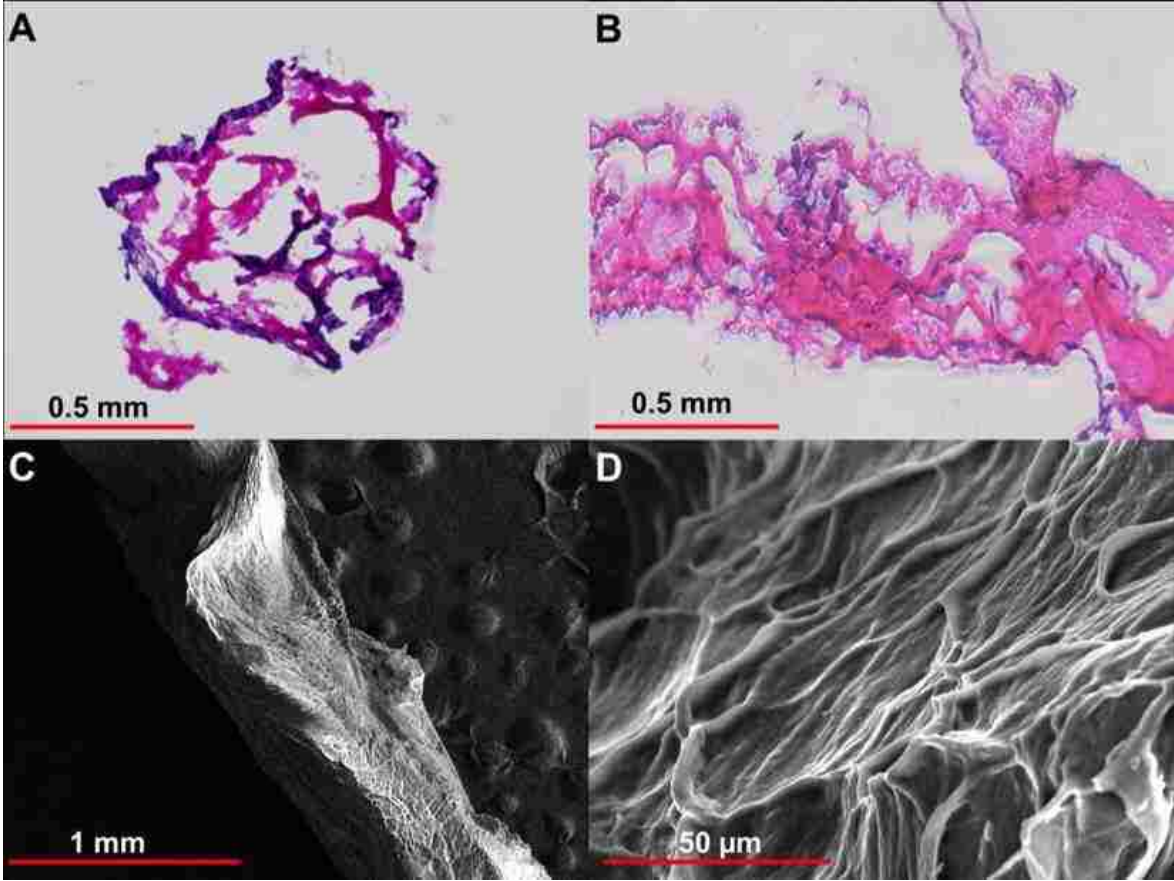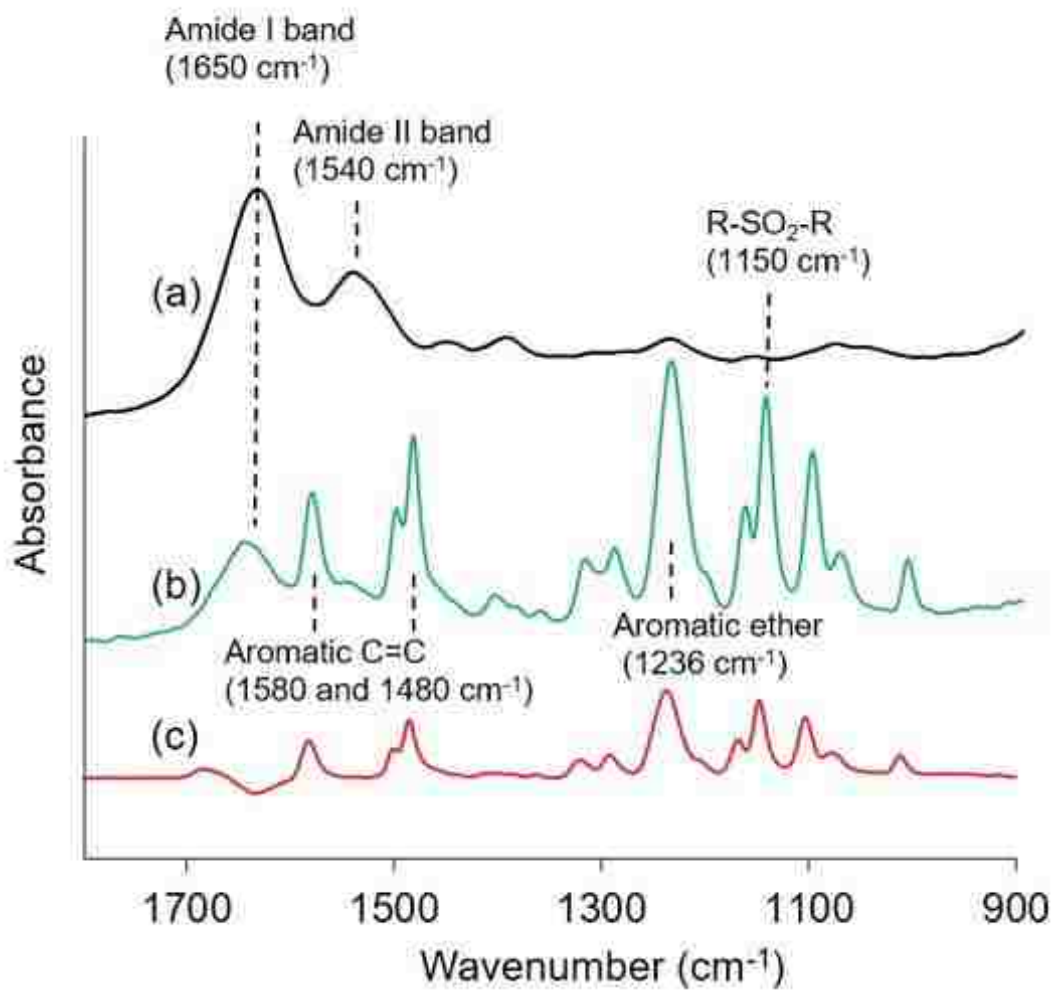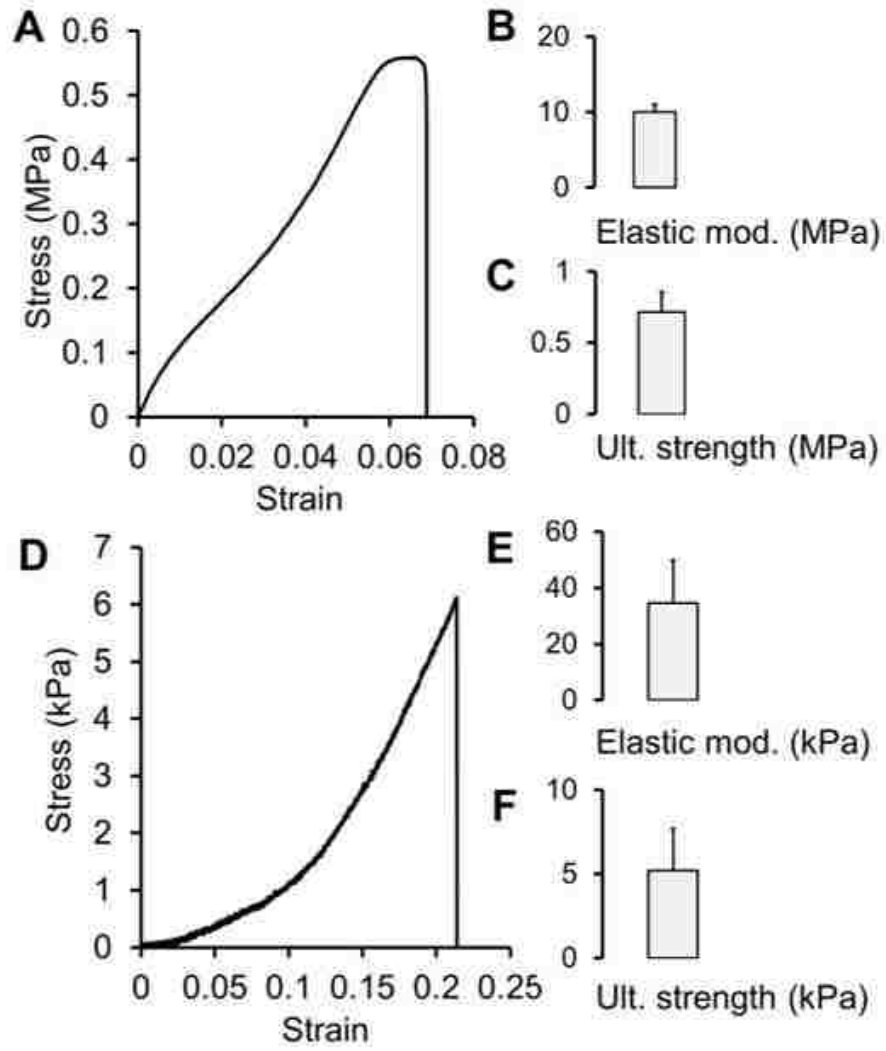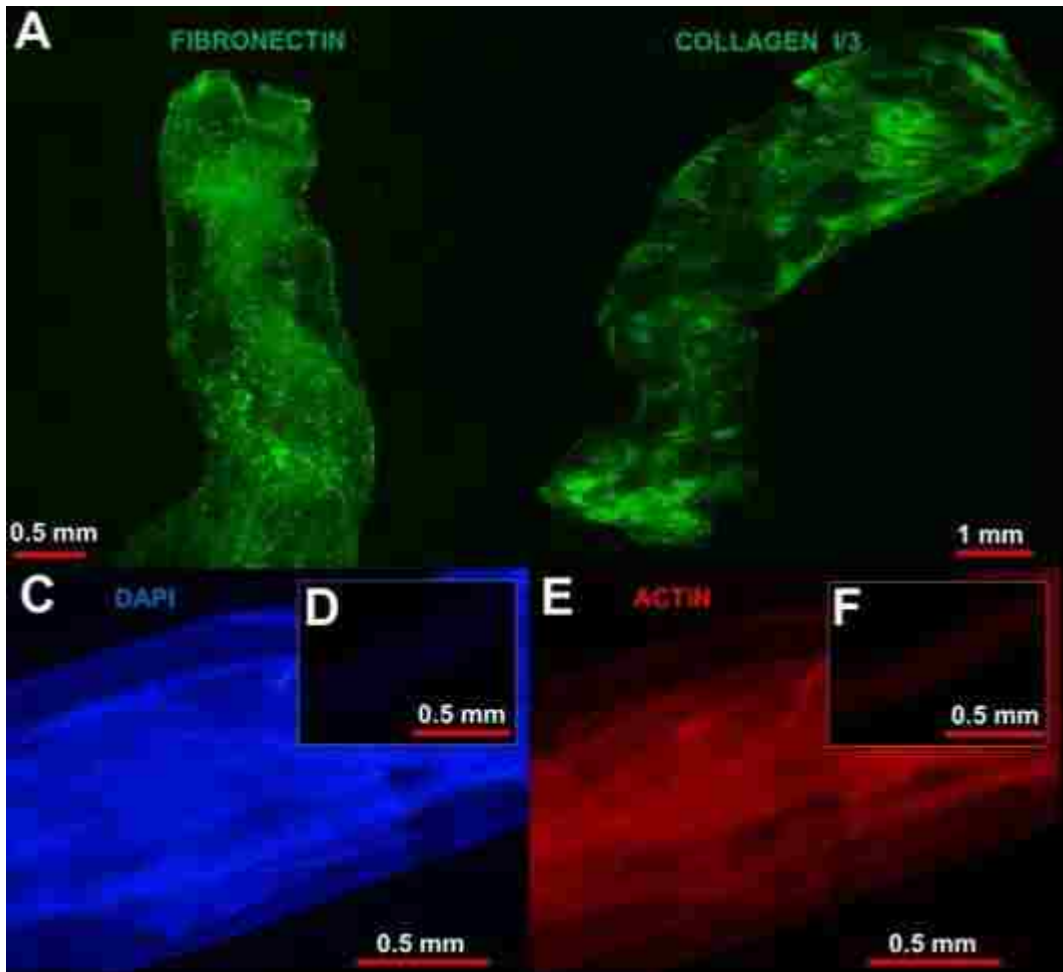Figure 4

Figure 5

Figure 6

Figure 7

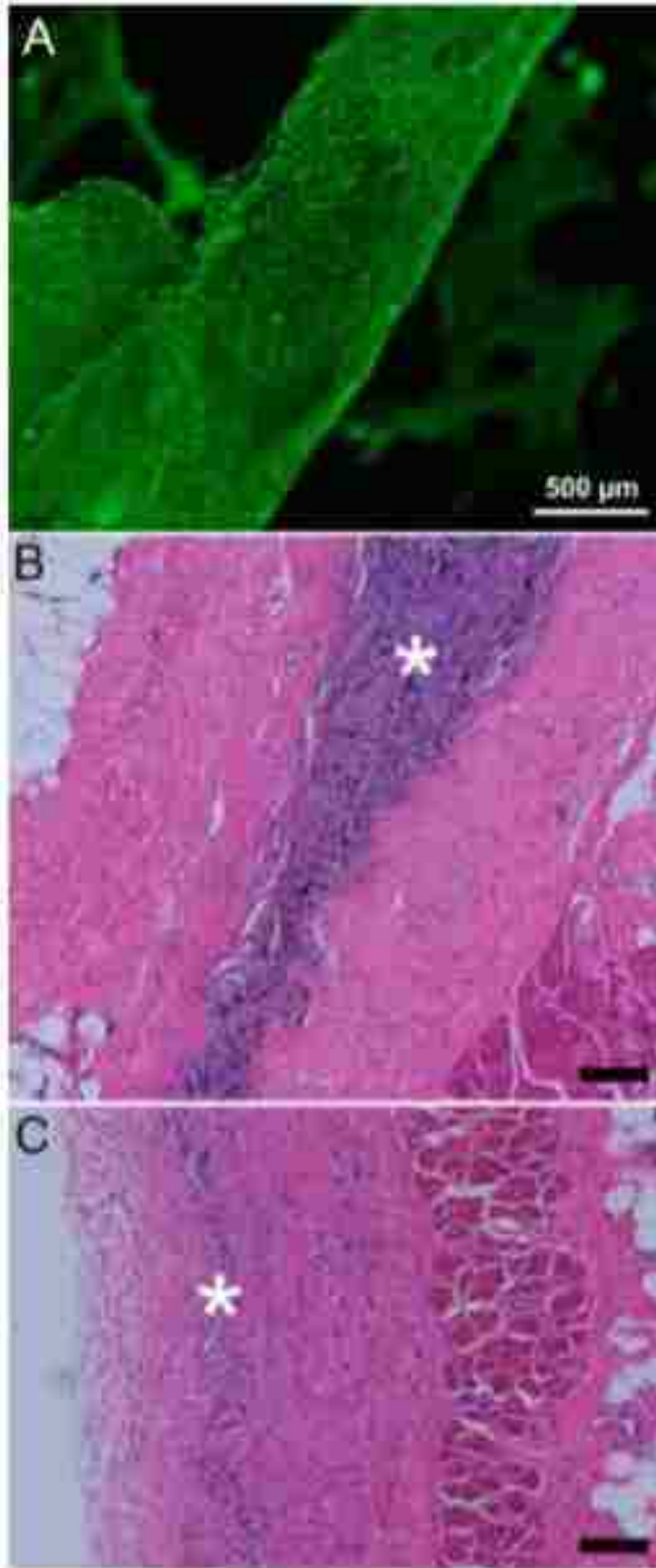Figure 8

Chapter 3

Production of Extracellular Matrix Fibers via Sacrificial

Hollow Fiber Membrane Cell Culture

Submitted as an original article by:

Kevin Roberts[1], John Kim[2], Shelby White, Jamie Hestekin[3], and Jeffrey C. Wolchok[2]

[1] Cell and Molecular Biology Program, University of Arkansas

[2] Department of Biomedical Engineering, University of Arkansas

[3] Ralph E Martin Department of Chemical Engineering, University of Arkansas

Corresponding Author:

Jeff Wolchok

125 Engineering Hall

Department of Biomedical Engineering

University of Arkansas

Fayetteville, AR 72701

jwolchok@uark.edu

Abstract

Engineered scaffolds derived from extracellular matrix (ECM) have driven significant interest in medicine for their potential in expediting wound closure and healing. Extraction of extracellular matrix from fibrogenic cell cultures *in vitro* has potential for generation of ECM from human- and potentially patient-specific cell lines, minimizing the presence of xenogeneic epitopes which has hindered the clinical success of some existing ECM products. A significant challenge in *in vitro* production of ECM suitable for implantation is that ECM production by cell culture is typically of relatively low yield. In this work, protocols are described for the production of ECM by cells cultured within sacrificial hollow fiber membrane scaffolds. Hollow fiber membranes are cultured with fibroblast cell lines in a conventional cell medium and dissolved after cell culture to yield continuous threads of ECM. The resulting ECM fibers produced by this method can be decellularized and lyophilized, rendering it suitable for storage and implantation.

A. Introduction

Implantable surgical scaffolds are a fixture of wound repair, with over one million synthetic polymer meshes implanted worldwide each year for abdominal wall repair alone[1]. However, following implantation the synthetic materials polymers traditionally used in the fabrication of these scaffolds tend to provoke a foreign body response, resulting in inflammation deleterious to the function of the implant and scarring of tissue[2]. Further, as the predominant synthetic mesh materials (*i.e.,* polypropylene) are not appreciably remodeled by the body, they are generally applicable to tissues where scarring can be tolerated, limiting their clinical usefulness toward the treatment of tissues with higher-order function such as muscle. While there are many surgical mesh products which have been applied with clinical success, recent manufacturer recalls of synthetic surgical meshes and complications from interspecies tissue implants highlight the importance of maximizing implant biocompatibility, prompting the FDA to tighten regulations on surgical mesh manufacturers[3,4]. Implantation of scaffolds derived from patients' own tissues reduces this immune response, but can result in significant donor-site morbidity[5]. Extracellular matrix (ECM) scaffolds produced *in vitro* are a possible alternative, as decellularized ECM scaffolds exhibit excellent biocompatibility, particularly in the case of autologous ECM implants[6].

Because of the limited availability of patient tissue to harvest for autologous implantation and the risk of impeding function at the donor site, the ability to produce ECM scaffolds *in vitro* from the culture of human cell lines or, if possible, a patient's own cells is an attractive alternative. The primary challenges in the manufacture of substantial amounts of ECM *in vitro* is the sequestration of these difficult-to-capture molecules. In previous work, we have demonstrated that ECM can be produced by culturing ECM-secreting fibroblasts in sacrificial polymeric foams that are dissolved after the culture period to yield ECM which can be decellularized for

implantation[7,8,9,10]. As ECM produced in foams tend to adopt the internal architecture of the foams, hollow fiber membranes (HFMs) were explored as a sacrificial scaffold for production of threads of ECM. Described herein are methods tasked for lab scale manufacturing of cell culture quality hollow fiber membranes and the extraction of bulk extracellular matrix fibers from the same following a period of fibroblast culture. This static culture approach is readily adoptable by laboratories containing standard mammalian cell culture equipment. ECM produced by this approach could be applied toward a variety of clinical applications.

B. Protocol

1. Production of Extracellular Matrix Using Sacrificial Hollow Fiber Membranes

CAUTION: N-methyl-2-pyrrolidone is an irritating solvent and reproductive toxicant. Exposure to NMP may cause irritation to the skin, eyes, nose, and throat. Solvent-resistant personal protective equipment should be used when handling NMP. Use of NMP should be performed within a fume hood.

1.1. Preparation of polysulfone polymer solution for hollow fiber membranes

1.1.1. Weigh 70 g of polysulfone pellets (molecular weight of 35 kD) in a weigh boat using an analytical balance.

1.1.2. Transfer 314 mL (323.3 g) of N-methyl-2-pyrrolidone (NMP) to a clean borosilicate flask.

1.1.3. Place a stir bar in the flask with NMP and place flask onto stirrer. Set the stirrer to a moderate rate of rotation.

1.1.4. Use a dry funnel to slowly insert the prepared 70 g of polysulfone into the flask with NMP.

1.1.5. Allow the polymer "dope" solution to stir for three days at room temperature, or until homogenized.

1.2. Setting concentricity and cleaning of the hollow fiber membrane spinneret

Note: Spinnerets are commercially available; correct spinneret dimensions are critical to successful membrane fabrication and are listed in the **Table of Materials**. Handle the spinneret very gently, as the spinneret needle is particularly fragile.

1.2.1. Use a screwdriver or drill with an appropriate screwdriver bit to carefully disassemble the spinneret.

1.2.2. Gently flow acetone through the inlet and outlet of the spinneret, collecting any acetone and residual polymer in a glass beaker for disposal.

1.2.3. Secure the upper body of the spinneret with the needle facing upward in a table vise.

1.2.4. Place the outlet (bottom) body of the spinneret onto the upper body.

1.2.5. Move the outlet body of the spinneret laterally while holding the upper body fixed on the vise until the spinneret needle is directly in the center of the outlet body.

1.2.6. Carefully and slowly reinsert the screws connecting the two bodies of the spinneret while ensuring that the needle visible at the spinneret outlet remains centered.

1.3. Fabrication of polysulfone hollow fiber membranes

1.3.1. Prepare a "bore solution" containing 45 mL of N-methyl-2-pyrrolidone and 255 mL of deionized water, forming a 15% mixture of NMP with deionized water.

1.3.2. Mount a concentric hollow fiber membrane spinneret 8 cm above the surface of a room-temperature tap water bath.

1.3.3. Connect the polymer inlet of the spinneret and the bore inlet of the spinneret to two separate steel pressure vessels having an inner volume of at least 350 mL. Both vessels must have check valves at their outlets.

1.3.4. Connect each of the pressure vessels to the regulators of separate N_2 gas cylinders

1.3.5. Use a funnel to insert the prepared dope solution (~315 mL) into the pressure vessel connected to the polymer inlet of the spinneret. Ensure that the top of the vessel is tightly sealed.

1.3.6. Use a funnel to insert the prepared bore solution (300 mL) into the pressure vessel connected to the bore inlet of the spinneret. Ensure that the top of the vessel is tightly sealed.

1.3.7. Open the check valve for the bore vessel first, then the polymer vessel second. If the spinneret is sufficiently clean, the bore solution will begin to stream out of the spinneret outlet.

1.3.8. Pressurize both vessels to 1 PSI. Visually confirm that both polymer and bore solutions are exiting the spinneret, with a continuous white filament precipitating as the combined streams contact the water bath.

1.3.9. Use long forceps to guide the nascent fiber under the rollers in the center of the bath, and then wind the nascent fiber around a rotating wheel connected to a motor.

1.3.10. Set the take-up wheel and motor to rotate at a rate of approximately two meters per minute.

1.3.11. Make minor adjustments to the regulators or take-up wheel speed as needed until a steady-state flow is achieved. The nascent fiber should form a 90° angle with the surface of the water bath.

1.3.12. Close the N_2 cylinder regulators and pressure vessel check valves and disengage the take-up wheel motor after all polymer and bore solution has been extruded from the vessels.

1.3.13. Remove the prepared hollow fiber membranes and place them into a deionized water bath for three days, exchanging deionized water once per day to remove residual solvent.

1.3.14. Sterilize the hollow fiber membranes by autoclaving them at 121 °C for 30 minutes or by immersing them for one day in 70% ethanol.

1.4. Cell seeding of hollow fiber membranes

Note: All cell culture procedures should be performed within a biosafety cabinet.

1.4.1. Treat the hollow fiber membranes with a 20 µg/mL solution of bovine plasma fibronectin in PBS (pH = 7.4) to promote cell attachment.

1.4.1.1. Weigh 1 mg of powdered bovine plasma fibronectin in a weigh boat and dissolve it in 1 mL of sterile PBS (pH = 7.4) in a sterile 1.5 mL microcentrifuge tube.

1.4.1.2. Incubate the 1 mg/mL bovine plasma fibronectin solution in the incubator for 30 minutes. Add the solution to 49 mL of sterile PBS in a sterile 50 mL conical centrifuge tube.

1.4.1.3. Incubate the fibers in the prepared 50 mL of bovine plasma fibronectin in an incubator at 37 °C with 5% CO_2 for 1 hour. Recollect the fibronectin solution for later use and store in a sterile 50 mL conical centrifuge tube at 4 °C.

1.4.2. Use sterile microscissors to cut the fibers to desired length (<6 cm).

1.4.3. Seed fibroblast cells directly into the lumina of the hollow fiber membranes at a seeding density of 100,000 cells per fiber using a 21-gauge needle with 1 mL syringe.

Note: A practicable target for preparing the cell-suspension for loading in the syringe is a suspension density of 100,000 cells for every 30 microliters of medium.

1.4.4. Place six seeded fibers into a 6 cm diameter Petri dish. Allow the seeded fibers to incubate at 37 °C with 5% CO_2 for five minutes.

1.4.5. Remove the seeded fibers from incubation and culture them for up to 3 weeks in DMEM/F-12 containing final concentrations of 50 µg/mL L-ascorbic acid and 150 µg/mL L-ascorbic acid 2-phosphate (freshly prepared and sterile filtered), 5 ng/mL TGF-ß1 (from sterile filtered aliquots stored at -20 °C), and 1% penicillin-streptomycin in a 6 cm Petri dish within a 5% CO_2 incubator at 37 °C. Exchange cell medium every two days.

1.5. Extraction of extracellular matrix from cultured hollow fiber membranes

1.5.1. Place cultured fibers into individual scintillation vial using forceps.

1.5.2. Place up to 5 mL of NMP into each vial using a glass pipette.

1.5.3. Immerse the hollow fibers in NMP, performing a total of three exchanges of NMP. Slowly aspirate the old NMP using a 1 mL pipette to prevent tearing of extracted ECM.

Note: When adding fresh NMP, it is helpful to tilt the vial and allow the NMP run down the sides, otherwise the remaining ECM scaffold is subjected to shear which may cause tearing.

1.5.4. Remove NMP and rinsed the resulting ECM thread 3 times in deionized water.

1.5.5. Cut a 1/32-inch thick sheet of silicone rubber to a length of 3 inches, width of 1 inch and cut an 8 mm by 4 mm rectangular mold in the center of the length of rubber.

1.5.6. Place the prepared piece of rubber onto a standard 3-inch by 1-inch microscopy slide and autoclave at 121 °C for 30 minutes.

1.5.7. Lay each ECM fiber side by side in the 8 mm by 4 mm silicone mold until there is no visible open space.

1.5.8. Place the mold into a 50 mL conical centrifuge tube and freeze at -80°C until completely frozen.

1.5.9. Lyophilize frozen ECM mesh overnight or until completely dry. Store the mesh at 4°C until ready for decellularization.

2. Decellularization of Extracellular Matrix

2.1. Prepare a solution of 1% (w/w%) sodium dodecyl sulfate (SDS) in deionized water.

2.2. Incubate extracted extracellular matrix in the mold in 1% SDS for 24 hours at room temperature on a rocker with gentle agitation.

2.3. Rinse extracted extracellular matrix three times in sterile phosphate-buffered saline (PBS) with gentle agitation, using 3 mL of PBS per rinse.

Note: Rinses should be performed gently to minimize tearing of prepared scaffolds.

2.4. Prepare 1 L of DNAse/RNAse digestion buffer.

Note: DNAse/RNAse digestion buffer may be stored for several months at 4°C.

2.4.1. Weigh 1.54 g of Tris HCl, 308 mg of $MgCl_2$, and 56 mg of $CaCl_2$ in separate weigh boats.

2.4.2. Combine Tris HCl, $MgCl_2$, and $CaCl_2$ with 1 L of deionized water in a large flask with a stir bar and stir until all components are dissolved.

2.4.3. Sterile filter the digestion buffer with a 0.22 µm filter into a sterile 1 L borosilicate bottle and store at 4°C.

2.5. Prepare 5 mL of DNAse/RNAse digestion solution.

Note: Digestion solution should be used within 24 hours of preparation.

2.5.1. Weigh 0.125 mg (50 kU) of DNAse I in a weigh boat and add to 5 mL of digestion buffer.

2.5.2. Add 75 µL of RNAse A stock solution to the digestion buffer.

2.6. Add 32 µL of the digestion solution to each prepared mold and incubate at 4°C for 6 hours.

2.7. Aspirate the digestion solution and rinse three times in sterile PBS.

2.8. Aspirate the PBS and incubate scaffolds overnight in 10% penicillin-streptomycin in PBS at 4°C.

2.9. Aspirate the penicillin-streptomycin and rinse scaffolds three times in sterile PBS.

2.10. Place the mold into a 50 mL conical centrifuge tube and freeze at -80°C.

2.11. Lyophilize the decellularized ECM mesh overnight or until completely dry.

2.12. Transfer the lyophilized scaffolds within a biosafety hood to a sterile container at 4°C pending use.

C. Results

Successful production of extracellular matrix from sacrificial scaffolds is contingent on appropriate scaffold fabrication, cell culture, and solvent rinse procedures. Fabrication of the hollow fiber membranes is performed using a dry-jet wet-spinning system assembled from commercially available components (**Figure 1**) which uses extrusion of polymer solution through the annulus of a commercially available steel spinneret (inner diameter = 0.8 mm, outer diameter = 1.6 mm) to generate a nascent tube of polymer solution which precipitates into a hollow fiber membrane upon contact with a water bath.

An example process for ECM extraction from HFMs is illustrated in **Figure 2**. **Figure 3A** shows a transverse cross-section of polysulfone HFMs fabricated under this protocol, exhibiting outer and inner layers of finger-like pores characteristic of an asymmetric membrane. In this protocol, cells are seeded specifically in the inner lumen of the membrane and cultured in 6 cm diameter Petri dishes (**Figure 3B**), with cells tending to proliferate on all surfaces of the membrane. Cultured membranes can then be subjected to batch NMP and deionized water rinsing in standard glass scintillation vials (**Figure 3C**), producing translucent threads of ECM (**Figure 3D**). ECM-producing cells remain viable inside HFMs throughout the 3-week period of culture (**Figure 4**).

HFMs cultured for three weeks with primary rat skeletal muscle fibroblasts (RSMF) were dissolved via three exchanges of N-methyl-2-pyrrolidone, after which they were rinsed three times in deionized water. The extracted matrix, normally being translucent in appearance when hydrated (**Figure 5A**), will tend to cloud upon hydration if not subjected to appropriate solvent

rinsing due to the presence of residual polymer. It should also be noted that the ECM remaining

after dissolution of the membrane is somewhat fragile, requiring care in handling with fine

forceps. ECM fibers assembled into meshes and then lyophilized exhibit an off-white color and

fibrous appearance with a gross longitudinal alignment (**Figure 5B**).

D. Discussion

The processes described enable the production of bulk ECM biomaterials *in vitro* using

hollow fiber membranes cast by a dry-jet wet spinning system allowing for inexpensive bulk

production of membranes as well as standard cell culture equipment. While the membranes

fabricated in this protocol are intended for use in cell culture, the system described can also be

adapted for the production of membranes for separation purposes, with pore size distribution and

hollow fiber dimensions tunable by varying spinneret dimensions, polymer used, dope and bore

flow rate, take-up speed, and environmental conditions.[13] Though the protocol detailed employs

hollow fiber membranes, in principle any dissolvable cell culture scaffold with appropriate

transport properties such as open cell foams could be used, as demonstrated in previous work[7-9].

This general approach appears useful for the production of ECM scaffolds by sacrificial

scaffolds which can more faithfully mimic the internal architecture of tissues. Implants produced

by this protocol in particular exhibit a gross alignment (**Figure 5B**), which may be of particular

benefit toward the reconstruction of highly aligned tissues such as tendons, ligaments and

skeletal muscle.

Regular exchange of medium and, in particular, supplementation of medium with

ascorbic acid and TGF- ß; is crucial to production of ECM, as ascorbic acid is an essential

enzyme in collagen biosynthesis, and TGF- ß; induces the synthesis of several ECM proteins[10].

Additionally, thorough rinsing of ECM with NMP must be performed, otherwise residual

polymer will remain in the extracted ECM, appearing as a white film during water rinses. Care

must be taken to not overly agitate ECM during membrane dissolution, as it is relatively fragile.

Collected ECM scaffolds intended for implantation must be subjected to a decellularization step

as described to remove xenogeneic epitopes to minimize a potential host foreign body response.

The significance of this technique lies in its production of a biocomplex scaffold of whole

extracellular matrix which can be remodeled by the body's own wound-healing processes. By

using this approach to produce ECM from cells specific to a target species, it may be possible to

minimize the foreign body response which hinders the clinical effectiveness of this class of

biomaterials; by using cells specific to an individual, the foreign body response may be lessened

further. This approach also allows for the production of ECM targeted toward particular tissues,

with recent reports suggesting that tissue-specific ECM may be particularly effective in certain

applications[12]. As this protocol allows for production of ECM across various cell lines, implants

combining ECM from several cell types (*e.g.* muscle, nervous, endothelial) could be used to

tailor implants to more faithfully approximate the structure and chemical complexity of target

tissues. While the ECM meshes presented here were originally intended as scaffolds for wound

repair, they may also have use as platforms for investigations into cell-ECM interactions,

durotaxis, and biosensing. In particular, this approach lends the investigator the ability to

produce ECM from specific cell types of interest which may allow for new insights into the

biological significance of tissue-specific ECM structure, composition and function.

Potential improvements to the ECM production techniques presented here could include

scale-up via the use of dynamic and pre-conditioning bioreactors as well as exploration of

alternative sacrificial scaffold materials and architectures. In particular, transition to a solventless

scaffold removal process would improve the safety of the extraction process; sacrificial scaffolds

composed of materials which are degradable by enzymes, such as regenerated cellulose, may allow for solventless ECM extraction[14]. While the tensile strength of these materials is below those of synthetic materials, there exist several avenues for improvement of these scaffolds, including exploration of various culture conditions, media formulations, and sacrificial scaffold geometries. Recent genetic engineering advances could be leveraged to produce pro-fibrotic cell lines, which in combination with platforms for ECM capture could enable the production of scaffolds satisfying clinical demands. Further, existing dynamic culture systems such as continuous flow-loop hollow fiber membrane bioreactors facilitate high rates of nutrient exchange conducive to greater and more rapid ECM production, and may be of particular interest in leveraging this technique for production of larger quantities of ECM for biological research and clinical use.

E. Acknowledgements

Table 1: Table of Specific Materials

Material	Supplier	Catalog Number	Comments
1/32 inch thick silicone rubber	Grainger	B01LXJULOM	
20 mL Scintillation Vials	VWR	66022-004	With attached white urea cap and cork foil liner
3 inch by 1 inch microscopy slides	VWR	75799-268	
4 °C refrigerator	Thermo Fisher	FRGG2304D	Any commercial 4C refrigerator will suffice.
50 mL conical tubes	VWR	21008-178	
6-well cell culture plates	VWR	10062-892	Alternative brands may be used
Acetone	VWR	E646	Alternative brands may be used
Bore vessel	McMaster-Carr	89785K867	6 ft 316 steel tubing
Bovine Plasma Fibronectin	Thermo Fisher	33010018	Comes as 1 mg of lyophilized protein
CaCl₂	VWR/Amresco	97062-590	
Cell Culture Incubator w/ CO₂			Any appropriate CO2-supplied mammalian cell incubator will suffice.
Disposable Serological Pipets	VWR	14673-208	Alternative brands may be used
DMEM/F-12, HEPES	Thermo Fisher	11330032	Warm in water bath at 37°C for 30 minutes prior to use
DNase I	Sigma-Aldrich	DN25-10MG	
Dope vessel	McMaster-Carr	89785K867	6 ft 316 steel tubing
Ethanol	VWR	BDH1160	Dilute to 70% for sterilization
Fetal Bovine Serum, qualified, US origin - Gibco	Thermo Fisher	26140079	Mix with growth media at 10% concentration (50mL in 500mL media)
Four 1/4-inch to 1" reducing unions	Swagelok	SS-1610-6-4	One reducing union for each inlet and outlet of each vessel

Table 1: Table of Specific Materials

Material	Supplier	Catalog Number	Comments
Freeze-dryer/lyophilizer	Labconco	117 (A653	Any lyophilizer will suffice.
Hexagonal Antistatic Polystyrene Weighing Dishes	VWR	89106-752	Any weigh boat will suffice
Hollow fiber membrane immersion bath			34L polypropylene tubs may be used or large bath containers can be fabricated from welded steel sheets
Hollow Fiber Membrane Spinneret	AEI	http://www.aei-spinnerets.com/specifications.html	Made to order. Inner diameter = 0.8 mm, outer diameter = 1.6 mm
Hot plate/stirrer	VWR	97042-634	
Human TGF-β1	PeproTech	100-21	
L-Ascorbic acid	Sigma-Aldrich	A4544-25G	
L-Ascorbic acid 2-phosphate	Sigma-Aldrich	A8960-5G	
L-glutamine (200 mM) - Gibco	Thermo Fisher	25030081	Mix with growth media at 1% concentration (5mL in 500mL media)
MgCl2	VWR/Alfa Aesar	AA12315-A1	
Minus 80 Freezer	Thermo Fisher	UXF40086A	Any commercial -80C freezer will suffice.
N2 gas cylinders (two)			
NIH/3T3 cells	ATCC	CRL-1658	Alternative fibrogenic cell lines may be used.
N-methyl-2-pyrrolidone	VWR	BDH1141	Alternative brands may be used

Table 1: Table of Specific Materials

Material	Supplier	Catalog Number	Comments
Penicillin/Streptomycin Solution	Thermo Fisher	15140122	Mix with growth media at 0.1% concentration (0.5 mL in 500mL media)
Polysulfone	Sigma-Aldrich	428302	Any polysulfone with an average Mw of 35,000 daltons may be used
Portable Pipet-Aid Pipetting Device - Drummond	VWR	53498-103	Alternative brands may be used
PTFE tubing (1/4-inch inner diameter)	McMaster-Carr	52315K24	Alternative brands may be used.
Rat skeletal muscle fibroblasts			Independently isolated from rat skeletal muscle. Alternative fibrogenic cell lines may be used.
RNase A	Sigma-Aldrich	R4642	
Silicone sheet	McMaster-Carr	1460N28	
Take-up motor	Greartisan	B071GTTSV3	200 RPM DC Motor
Tris HCl	VWR/Amresco	97063-756	
Two needle valves	Swagelok	SS-1RS4	

References

1   Cobb, W. S., Kercher, K. W. & Heniford, B. T. The argument for lightweight polypropylene mesh in hernia repair. *Surgical Innovation.* **12** (1), 63-69 (2005).

2   Morais, J. M., Papadimitrakopoulos, F. & Burgess, D. J. Biomaterials/Tissue Interactions: Possible Solutions to Overcome Foreign Body Response. *The AAPS Journal.* **12** (2), 188-196, doi:10.1208/s12248-010-9175-3, (2010).

3   Simon, P. *et al.* Early failure of the tissue engineered porcine heart valve SYNERGRAFT® in pediatric patients. *European Journal of Cardio-Thoracic Surgery.* **23** (6), 1002-1006, doi:10.1016/s1010-7940(03)00094-0, (2003).

4   *FDA strengthens requirements for surgical mesh for the transvaginal repair of pelvic organ prolapse to address safety risks*. (Food and Drug Administration, 2016).

5   Kartus, J., Movin, T. & Karlsson, J. Donor-site morbidity and anterior knee problems after anterior cruciate ligament reconstruction using autografts. *Arthroscopy: The Journal of Arthroscopic & Related Surgery.* **17** (9), 971-980, doi:http://dx.doi.org/10.1053/jars.2001.28979, (2001).

6   Lu, H., Hoshiba, T., Kawazoe, N. & Chen, G. Autologous extracellular matrix scaffolds for tissue engineering. *Biomaterials.* **32** (10), 2489-2499, doi:http://dx.doi.org/10.1016/j.biomaterials.2010.12.016, (2011).

7   Wolchok, J. C. & Tresco, P. A. The isolation of cell derived extracellular matrix constructs using sacrificial open-cell foams. *Biomaterials.* **31** (36), 9595-9603, doi:http://dx.doi.org/10.1016/j.biomaterials.2010.08.072, (2010).

8   Roberts, K., Schluns, J., Walker, A., Jones, J. D., Quinn, K. P., Hestekin, J., & Wolchok, J. C.. Cell derived extracellular matrix fibers synthesized using sacrificial hollow fiber membranes. *Biomedical Materials*, *13*(1), (2017)

9   Hurd, S. A., Bhatti, N. M., Walker, A. M., Kasukonis, B. M. & Wolchok, J. C. Development of a biological scaffold engineered using the extracellular matrix secreted by skeletal muscle cells. *Biomaterials.* **49** 9-17, doi:http://dx.doi.org/10.1016/j.biomaterials.2015.01.027, (2015).

10   Kasukonis, B. M., Kim, J. T., Washington, T. A. & Wolchok, J. C. Development of an infusion bioreactor for the accelerated preparation of decellularized skeletal muscle scaffolds. *Biotechnology Progress.* **32** (3), 745-755, doi:10.1002/btpr.2257, (2016).

11   Murad, S. *et al.* Regulation of collagen synthesis by ascorbic acid. *Proceedings of the National Academy of Sciences of the United States of America.* **78** (5), 2879-2882 (1981).

12   Zhang, Y. *et al.* Tissue-specific extracellular matrix coatings for the promotion of cell proliferation and maintenance of cell phenotype. *Biomaterials.* **30** (23-24), 4021-4028, doi:10.1016/j.biomaterials.2009.04.005, (2009).

13.   Feng, C. Y., Khulbe, K. C., Matsuura, T., & Ismail, A. F. Recent progresses in polymeric hollow fiber membrane preparation, characterization and applications. *Separation and Purification Technology*. **111**, 43-71 (2013)

14.   Domb, A. J., Kost, J. & Wiseman, D. *Handbook of Biodegradable Polymers*. (CRC Press, 1998).

G. Appendix

Figure Legend:

Figure 1: Illustrated process flow for casting hollow fiber membranes

Hollow fiber membranes are manufactured using the ubiquitous non-solvent induced phase separation method (NIPS) using a system prepared from commercially available components listed in the table of specific materials. Polysulfone in NMP (17.8 w/w%) and NMP bore solutions (15 w/w% NMP in water) are extruded from separate stainless steel vessels by pressurized N_2 into a spinneret, generating a nascent hollow fiber membrane at the spinneret outlet which fully precipitates upon contact with the tap water precipitation bath. Nascent hollow fiber is manually guided under and over guides and allowed to collect on a rotating motorized take-up wheel at a rate of 2.3 meters per minute.

Figure 2: Illustrated production of ECM from cultured hollow fiber membranes

Hollow fiber membranes are seeded with fibroblasts and cultured for three weeks, followed by exchange of NMP 3x and exchange of deionized water 3x.

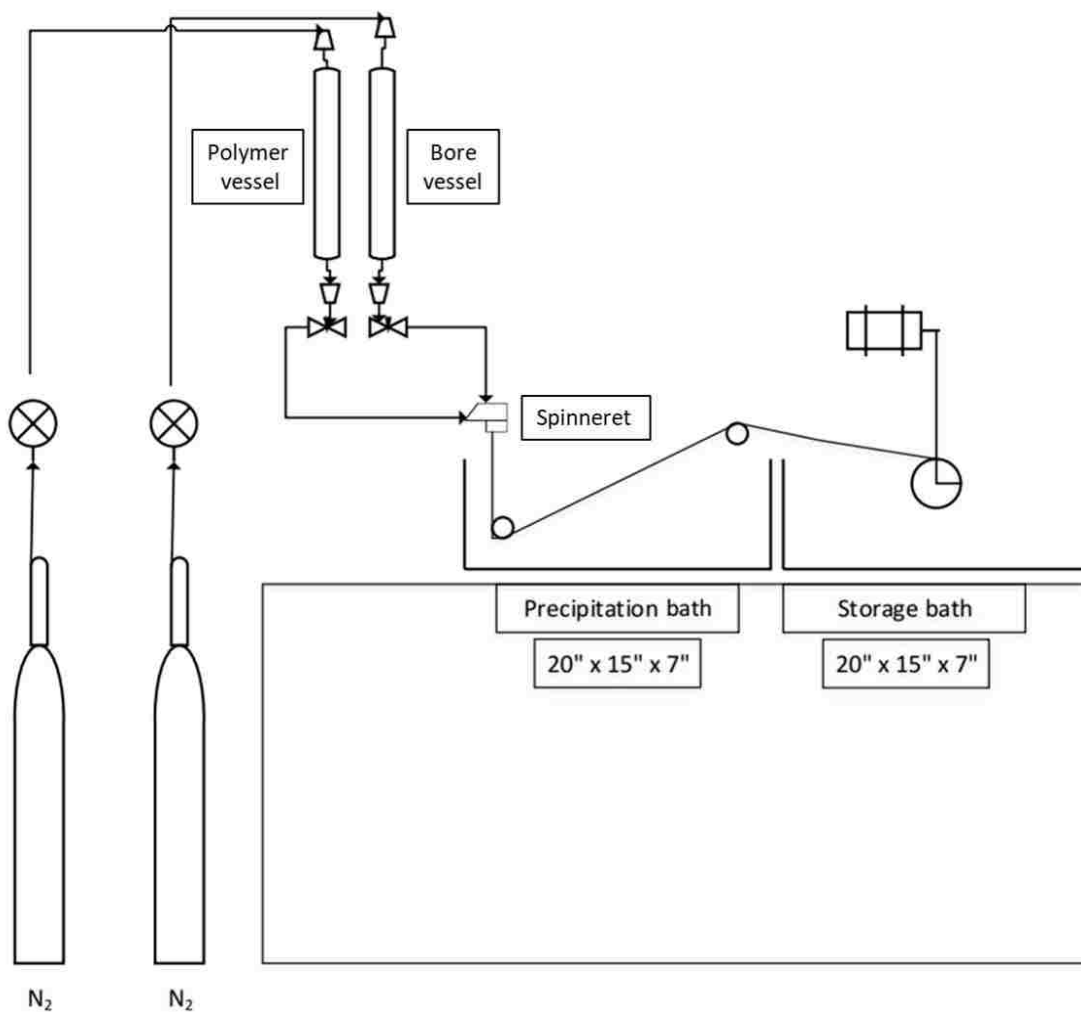## Figure 3: Culture and extraction of ECM

Asymmetric mesoporous hollow fiber membranes **(A)** were cultured for three weeks with RSMF cells in DMEM/F-12 with supplemented ascorbic acid and TGF-ß; **(B)**. Cultured hollow fibers (**C, D** top) were dissolved via 3 exchanges in n-methyl-2-pyrrolidone then rinsed three times in deionized water, resulting in continuous threads of ECM (**D**, bottom). High magnification scanning electron microscopy micrograph of the ECM fiber surface **(E)**.

Figure 4: Cell viability on hollow fiber membranes

Representative hollow fiber membranes cultured with RSMF cells for three weeks were longitudinally sectioned using a fine razor to reveal the luminal surface of the HFMs and subjected to live-dead staining with Calcein AM and EthD-1. Viability staining revealed a confluent layer of viable cells with negligible EthD-1 fluorescence.

Figure 5: Assembly of ECM implant

Individual extracellular matrix threads (n = 30) derived from culture of RSMF cells were placed lengthwise into a silicone mold **(A)** and decellularized by 1% SDS followed by treatment with DNAse I, RNAse A, and penicillin-streptomycin. Decellularized ECM was then lyophilized, yielding an off-white mesh with a fibrous appearance and longitudinal architecture **(B)**.

Polymer vessel

Bore vessel

Spinneret

Precipitation bath
20" x 15" x 7"

Storage bath
20" x 15" x 7"

N₂   N₂

Lab bench, minimum dimensions: L = 4 ft, W = 2 ft

Figure 1

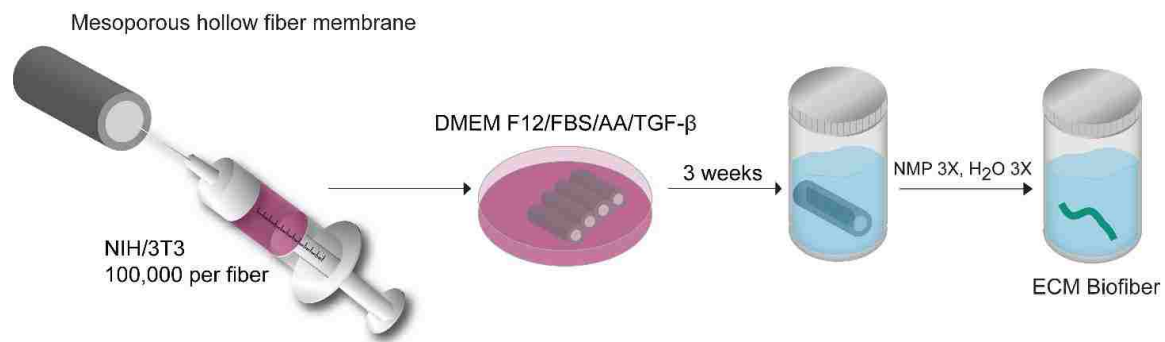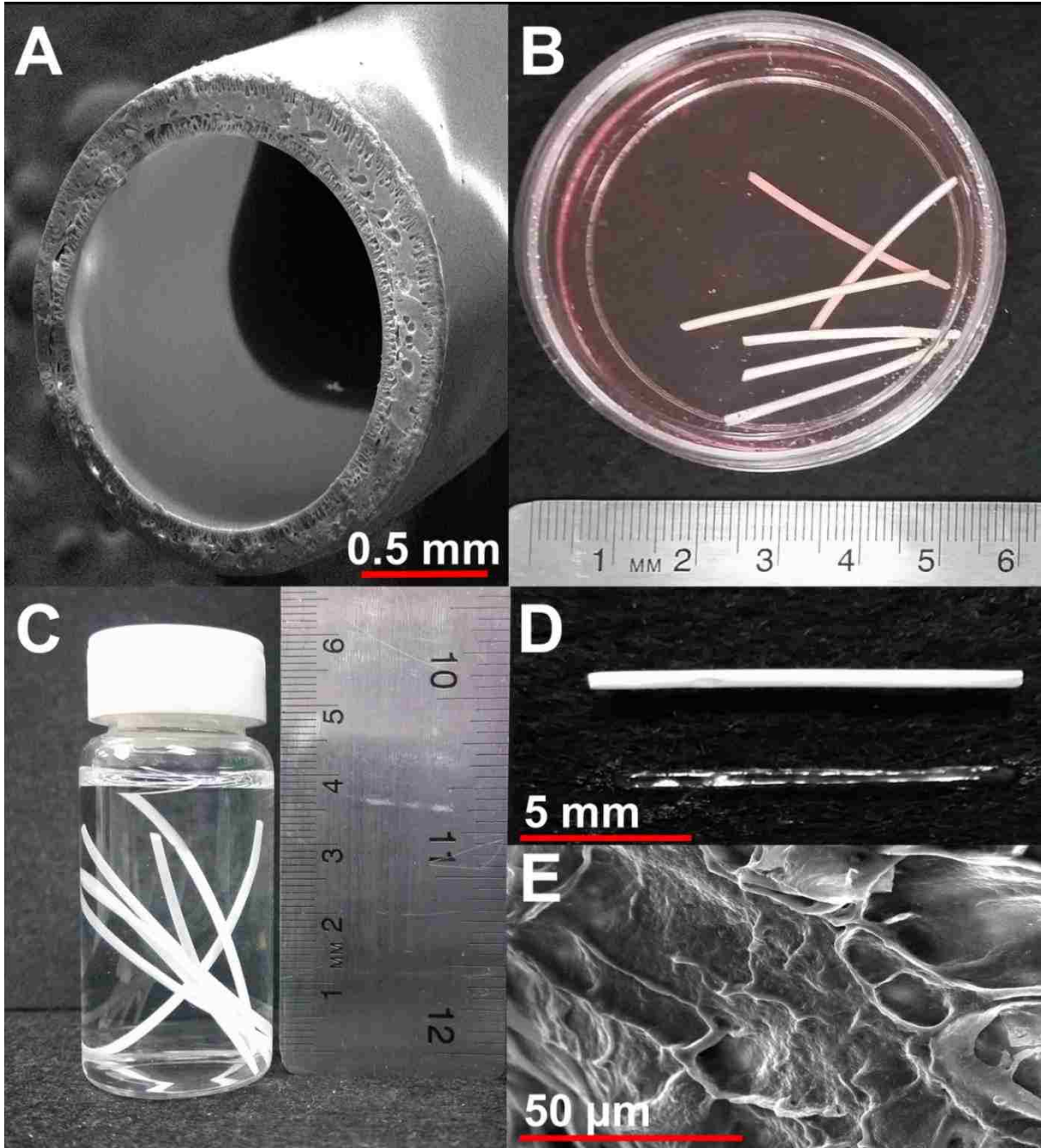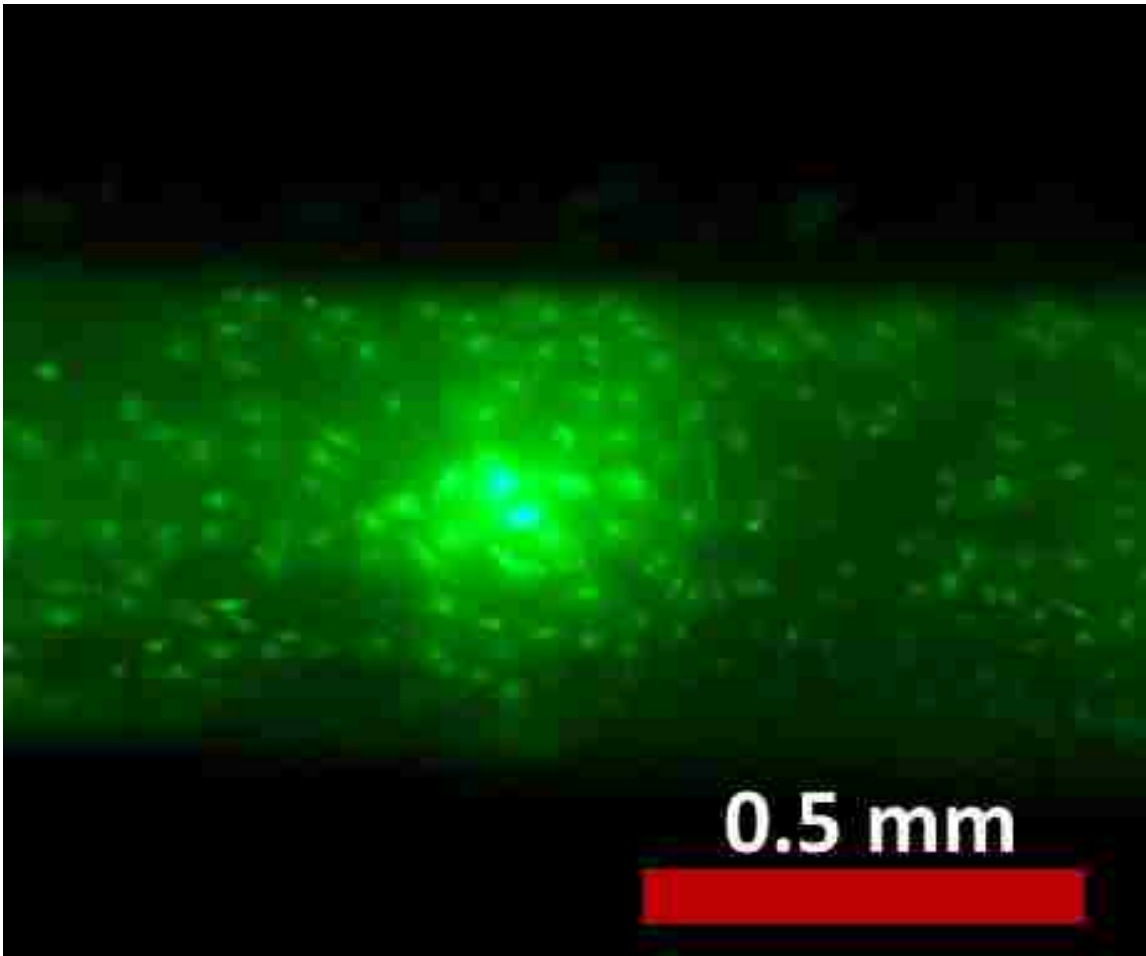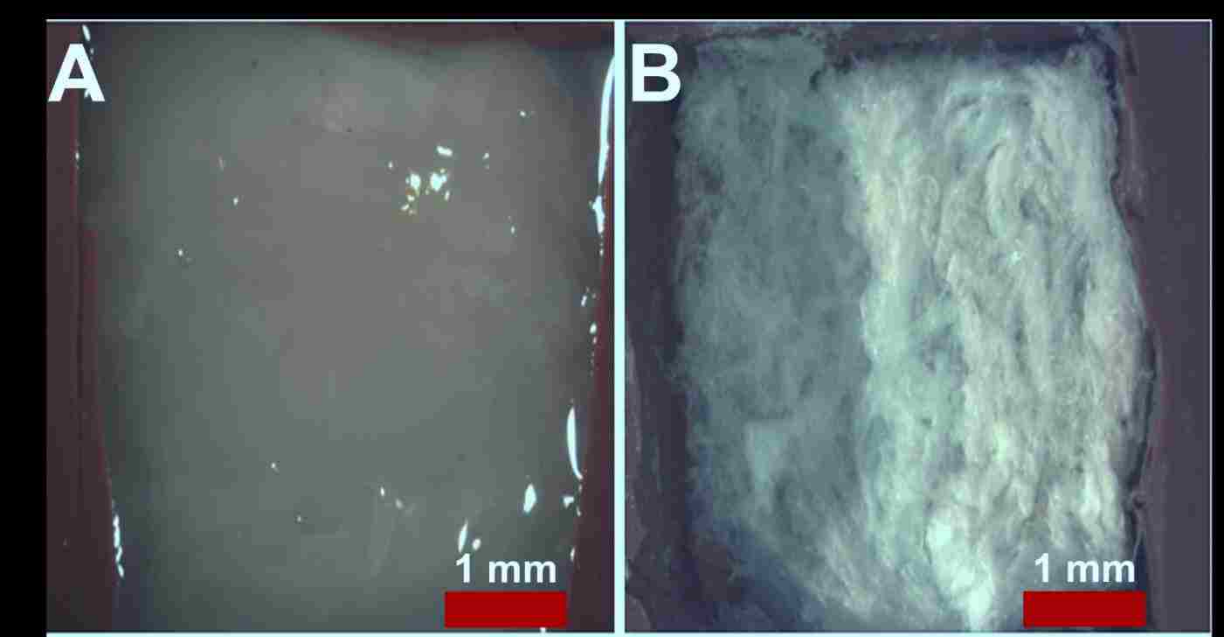Figure 2

Figure 3

Figure 4

Figure 5

Chapter 4

Evapore: A Python GUI Tool for Evapoporometry Data Processing

To be submitted as an <u>original article</u> by:

Kevin Roberts[1], Victoria Klaus[2], Mojtaba Abolhassani[2], Jeffrey C. Wolchok[3], Lauren Greenlee[2], and Jamie Hestekin[2]

[1] Cell and Molecular Biology Program, University of Arkansas, Fayetteville, AR

[2] Ralph E Martin Department of Chemical Engineering, University of Arkansas, Fayetteville, AR

[3] Department of Biomedical Engineering, University of Arkansas, Fayetteville, AR

Corresponding Author:

Jamie Hestekin

BELL Engineering Rm 3190

Ralph E. Martin Department of Chemical Engineering

University of Arkansas

Fayetteville, AR 72701

jhestekin@uark.edu

479-575-3492

Abstract

Evapoporometry is a promising emerging method of pore diameter characterization with particular applicability toward characterization of mesoporous materials. The evapoporometric approach is notable for requiring relatively inexpensive and ubiquitous laboratory equipment relative to other pore characterization methods; however, to date the method has largely been relegated to groups dedicated to membrane characterization due to the nontrivial data analysis involved. In an effort to extend the use of this promising method beyond membrane specialists, we demonstrate a free open-source software aid for standardizing evapoporometry data analysis and assess its applicability for pore size of macroreticular ion exchange resins as well as estimation of surface area, a key property of interdisciplinary interest.

Introduction

The performance of porous materials used in separations processes is dictated primarily by their pore size distributions, making accurate characterization of pore size a critical aspect of the manufacturing process.[1] In particular, mesoporous materials have broad application in industry as ultrafiltration membranes, catalysts, adsorbents, and drug carriers, where consistent performance requires tight control of pore size distribution, porosity, and surface area.[2,3] A variety of techniques exist to characterize pore diameter, by direct methods –such as electron microscopy- or indirect such as mercury porosimetry.[4] However, image analysis of pore size is performed on very small portions of the sample which may not be truly representative of the whole, while methods based on liquid displacement or gas adsorption often require rather expensive equipment and significant technical expertise on the part of the investigator. Further, methods such as mercury porosimetry require application of high pressures for detection of small pores which can affect the structure of the sample during measurement.[5]

Evapoporometry (EP) is a relatively new method for indirect determination of pore diameter distribution based on the Kelvin equation, which relates vapor pressure to the curvature of liquid-gas interfaces within liquid-filled pores.[6] Unlike gas adsorption/desorption or permporometry which characterize capillary condensation within pores[7], evapoporometry relies on the measurement of the isothermal evaporation of a fluid from filled pores of a sample contained within a cylindrical test cell, with evacuation of liquid from larger pores preceding that of smaller pores due to increasing vapor pressure depression as pore size decreases. Krantz *et al* developed a mass transfer model demonstrating that the Kelvin equation can be rearranged to calculate pore diameter directly from the evaporation rate of fluid from pores[6,8,9] via:

Equation 1

$$d = -\frac{4yV}{RT\ln\frac{W_{A0}}{W_{A0}^{\circ}}}$$

Where y is the surface tension of the liquid within the pores, V is the vapor molar volume, R is the universal gas constant, T is absolute temperature, W_{A0} is the evaporation rate of liquid from pores, and W_{A0}° is the evaporation rate of the fluid layer initially present above the sample. Fisher and Israelachvili found the Kelvin equation to be valid for menisci with a mean radius of curvature > 4 nm[10], a finding later validated by Mitropoulos[11]. While the evaporating liquid most used in evapoporometry studies has been 2-propanol, the use of fluids with a higher surface tension and liquid molar volume have been found to allow for characterization of pore diameters up to 365 nm.[9] Unique to evapoporometry is the capability to evaluate the pore size distribution of samples across a range of fluids without the application of pressure, enabling the investigator to predict the separation properties of the sample in different liquid media.

Despite the promising agreement of evapoporometry-measured pore diameter distributions with competing methods, evapoporometry has thus far largely been applied to ideal well-characterized samples such as commercial asymmetric Anopore membranes[6,9], having regular pore and support structures allowing for a correction of evaporative mass-loss data necessary for highly asymmetric membranes.[12,13] In contrast, the irregular substructure[14] of solvent-cast asymmetric membranes precludes this asymmetry correction, making the method most appropriate as a tool for detecting relative changes in pore diameter distribution, as in the case of fouled asymmetric membranes.[15]

In this work, we present an open-source standalone Python application for data analysis (Evapore), and assess the capability of software-aided evapoporometry for characterizing the pore

size distributions of asymmetric anodisc membranes macroreticular ion exchange resins, ubiquitous in water softening, purification, and catalysis.[16,17] It is anticipated that the availability of a software platform for EP analysis will encourage the adoption of this useful adjunct to gold-standard pore measuring techniques, and that its application toward nonclassical porous materials may yield fruitful insights for studies outside of the field of membrane research.

Methods

Evapoporometry

An EP apparatus comprising a custom-fabricated PTFE test cell, analytical balance, and laptop interfaced to the balance by RS232-USB was assembled as described previously (**Figure 1**).[8] Samples were immersed in an evaporating fluid for 2 hours, then sealed into the test cell with a liberal application of vacuum grease on the periphery of the test cell to ensure one-dimensional mass transfer, with several drops of fluid added above the sample to produce a free-standing layer. 2-propanol was selected as the evaporating fluid due to its nonwetting properties as well as its use in previous EP publications. Activated carbon was placed in scintillation vials surrounding the weighing plate as a desiccant to minimize the retention of volatile fluid in atmosphere. An XS105 balance (Mettler Toledo; Greifensee, Switzerland) with a resolution of $10\,\mu g$ was used to monitor evaporative mass loss over time under stable ambient temperature.

Scanning Electron Microscopy

Visualization of sample surface morphology was achieved through direct use of a Nova Nanolab 200 following sputter-coating with gold-palladium before and after immersion for 2 hours in 99% 2-propanol.

Data analysis

An open-source standalone program (Evapore) with a graphic user interface was developed in Python 3.7 to automate evapoporometry data analysis in order to minimize user error and ensure reproducibility. With source code and executable files available at github.com/RobertsEng/Evapore, the program proceeds as follows:

1. The user is prompted by a dialog to load a headerless .XLSX file with the first column containing evaporative mass loss data for a test cell containing a fluid-saturated sample and an additional small layer of fluid overlying the sample.

2. The user is prompted to input parameters related to the acquisition of gravimetric data for a layer of volatile fluid evaporating from an otherwise empty test cell, including the fluid used, absolute temperature, and time interval between acquisition of mass measurements.

3. The mass column is subjected to a moving average ($i = 20$) to minimize the effect of noise on the calculated pore diameter distribution.

4. The evaporation rate (g/s) is calculated from the slope of a mass versus time array.

5. An interactive plot of evaporation rate versus time is rendered to the user, prompting them to select the initial x-axis values at which the period of constant evaporation occurs (W_{A0}), corresponding to evaporation of the layer of fluid overlying the sample. The evaporation rates are converted to mol/s via division by the molecular weight of the fluid used. An average evaporation rate (W_{A0}) and standard deviation for this period are then calculated.

6. W_{A0} is used to determine the start point at which evaporation of fluid from the pores of the sample begins, corresponding to the first point on the graph at which $W_A < W_A - 3\sigma$. A horizontal line with height equal to this evaporation value is overlaid on the graph to guide the user.

7. The pore diameter corresponding to each instantaneous evaporation rate is computed using equation 2.

8. Instantaneously measured pore diameters are grouped into bins with a width of 5 nm. The percentage of pore-evaporated mass for each bin is used to determine an average pore size by the Bachmann-Anderson-Gurvitsch rule. The user is prompted to save pore diameter data in .CSV format and an interactive graph of pore size distribution is rendered.

Surface area of samples was assessed using the Bachmann-Anderson-Gurvitsch rule relating total pore volume to surface area, generally applied to materials with cylindrical, rigid, and well-defined pores[18-22]:

Equation 2

$D = 4V/S$

Where D is mean pore diameter, V is specific pore volume (m^3/g), and S is specific surface area in m^2/g. Mean EP pore diameter is substituted for D and the liquid volume of fluid evaporated during the pore draining period is substituted for V, allowing for calculation of specific surface area. Here, a specific volume derived from the density of the EP fluid used and mass lost during pore draining are substituted for V as an analog for specific pore volume.

N_2 Adsorption-Desorption

Comparison of evapoporometry surface area measurements for Amberlyst-15 ion exchange resin was enabled by analysis of the resin in an Autosorb iQ automated gas sorption analyzer and data processing in ASiqwin software (Quantachrome). Samples were degassed at 100 °C for 21 hours prior to measurement.

Statistical methods

All statistical analysis was performed in Graphpad Prism v8.0.1 (Graphpad Software, San Diego). ANOVA with post-hoc Tukey's test was used for all significance testing between groups ($\alpha = 0.05$). Quantitative data are presented as mean $\pm$ standard deviation.

Results

Scanning electron microscopy of anodisc membranes revealed highly ordered and dense pore structures for Anodisc membranes consistent with literature (**Figure 3A)** with an irregular and scattered pore structure for Amberlyst 15 ion exchange resin beads. Imaging of membranes and ion exchange resin following a 2-hour immersion in 2-propanol resulted in no evident changes to surface morphology.

Evapoporometric analysis of pore diameter for Anodisc 13, Amberlyst 15, and Anodisc 47 samples yielded mean pore diameters of 24.9 ± 2.7 nm, 30.1 ± 3.0 nm, and 108 ± 1.1 nm, respectively (**Figure 4A**). Linear regression analysis of evapoporometric pore determination against nominal manufacturer-reported mean N_2 adsorption-assessed pore diameter revealed a strong agreement ($R^2 = 99.37$) and significantly non-zero slope ($p < 0.0001$) (**Figure 4B**). Representative pore diameter distributions for ANO-13, AMB-15, and ANO-47 ranged from the 5-35 nm, 10-85 nm, and 5-300 nm bins, respectively. One-way ANOVA indicated significant differences within the diameter dataset ($p < 0.0001$), with a post-hoc Tukey's test indicating significant differences in diameter across ANO-13 versus ANO-47 ($p < 0.0001$) and AMB-15 versus ANO-47 ($p<0.0001$).

Estimation of surface area by application of the Bachmann-Anderson-Gurvitsch rule for Anodisc 13, Amberlyst 15, and Anodisc 47 samples indicated approximate specific surface areas of 203 ± 37 m^2/g, 123 ± 4.62 m^2/g, and 2.69 ± 1.42 m^2/g, respectively (**Figure 5**). One-way

ANOVA indicated significant differences across the dataset (p = 0.0002), with post-hoc Tukey's test indicating significant differences across all comparisons (p = 0.0131 for ANO-13 v AMB-15, p = 0.0001 for ANO-13 vs ANO-47, and p = 0.0025 for AMB-15 v ANO-47). Measurement of Amberlyst-15 surface area by Brunauer–Emmett–Teller analysis of N_2 adsorption-desorption indicated a surface area of 42.5 m^2/g, identical to widely reported BET analysis of this material[23], suggesting an overestimation of specific surface area by evapoporometry.

Discussion

In this work we have evaluated the accuracy and precision of a standalone software application in analysis of Evapoporometry data for pore diameter distribution and surface area characterization for porous materials, including an ion exchange resin with a macroscale geometry substantially different from synthetic membranes analyzed in previous reports. While evapoporometry exhibits the advantages of limited equipment expense and straightforward experimental protocol, the data analysis involves a series of nontrivial data analysis steps including graphical analysis which leads to variation in final results between individual investigators. While an element of graphical analysis still exists in Evapore data processing in terms of the selection of the initial steady-state region of evaporation, the relative standardization of the process and automation of remaining steps minimizes between-user variation and enables rapid reanalysis.

While previous reports have investigated evapoporometry as a general method of pore diameter determination in the context of idealized alumina membranes there is substantial interdisciplinary interest in the determination of pore diameter distribution for more irregular materials such as nonsolvent-induced phase separation-cast membranes, macroporous ion exchange resins, electronspun nanofibrous meshes, as well as soils, where pore size distribution

can be used to predict properties ranging from gas diffusion to soil productivity[24] (with the advantage that such samples can be analyzed by natural evaporation of water). We demonstrate that a semi-automated software-based analysis allows for fine determination of pore size for mesoporous materials, but notably with a lesser variation in comparison to previous reports for membranes of identical nominal pore size. It is additionally shown that evapoporometry faithfully reproduces the nominal mean pore diameter for Amberlyst 15, a macroporous ion exchange resin, with

We further demonstrate that while expected trends in surface area between different samples are reflected in relative terms in the evapoporometric determination of surface area via the Gurvitsch-rule, evapoporometry appears to substantially overestimate surface area compared to BET, indicating at present that the method appears unsuitable for determination of absolute surface area. Finer exploration of mathematical models applicable to EP may yield insights to reduce discrepancies between EP and gold-standard methods.

Combination of this software-aided approach with open-source data acquisition technology is anticipated to reduce the financial, time, and personnel costs of pore size analysis and reduce the barrier of entry for investigators interested in mesoporous pore size and surface area properties but for whom existing methods are cost-prohibitive or otherwise inappropriate. The Evapore software tool developed in this tool is publicly available in both original source and executable form at https://github.com/RobertsEng/Evapore.

Author Disclosure Statement:

The authors report no competing financial interests.

References

1   Mulder, J. *Basic principles of membrane technology*. (Springer Science & Business Media, 2012).

2   Purkait, M. K. & Singh, R. *Membrane Technology in Separation Science*. (CRC Press, 2018).

3   Zeman & Zydney, A. L. *Microfiltration and ultrafiltration: principles and applications*. (CRC Press, 1996).

4   Lowell, S., Shields, J. E. & Thomas, M. A. *Characterization of porous solids and powders surface area, pore size and density*. (Springer, 2011).

5   Giesche, H. Mercury porosimetry: a general (practical) overview. *Particle & particle systems characterization* **23**, 9-19 (2006).

6   Krantz, W. B., Greenberg, A. R., Kujundzic, E., Yeo, A. & Hosseini, S. S. Evapoporometry: A novel technique for determining the pore-size distribution of membranes. *Journal of membrane science* **438**, 153-166 (2013).

7   Evans, R., Marconi, U. M. B. & Tarazona, P. Capillary condensation and adsorption in cylindrical and slit-like pores. *Journal of the Chemical Society, Faraday Transactions 2: Molecular and Chemical Physics* **82**, 1763-1787 (1986).

8   Akhondi, E., Zamani, F., Chew, J. W., Krantz, W. B. & Fane, A. G. Improved design and protocol for evapoporometry determination of the pore-size distribution. *Journal of Membrane Science* **496**, 334-343, doi:https://doi.org/10.1016/j.memsci.2015.09.013 (2015).

9   Zamani, F. *et al.* Extending the uppermost pore diameter measureable via Evapoporometry. *Journal of Membrane Science* **524**, 637-643 (2017).

10   Fisher, L. R. & Israelachvili, J. N. Experimental studies on the applicability of the Kelvin equation to highly curved concave menisci. *Journal of Colloid and Interface Science* **80**, 528-541, doi:https://doi.org/10.1016/0021-9797(81)90212-5 (1981).

11   Mitropoulos, A. C. The Kelvin equation. *Journal of Colloid and Interface Science* **317**, 643-648, doi:https://doi.org/10.1016/j.jcis.2007.10.001 (2008).

12   Hernandez, A. *et al.* Surface structure of microporous membranes by computerized SEM image analysis applied to Anopore filters. *Journal of membrane science* **137**, 89-97 (1997).

13   Palacio, L., Pradanos, P., Calvo, J. & Hernandez, A. Porosity measurements by a gas penetration method and other techniques applied to membrane characterization. *Thin Solid Films* **348**, 22-29 (1999).

14   Bungay, J. K. *Synthetic Membranes:: Science, Engineering and Applications*. Vol. 181 (Springer Science & Business Media, 2012).

15   Ladewig, B. & Al-Shaeli, M. N. Z. *Fundamentals of membrane bioreactors*. (Springer, 2017).

16   Alexandratos, S. D. Ion-Exchange Resins: A Retrospective from Industrial and Engineering Chemistry Research. *Industrial & Engineering Chemistry Research* **48**, 388-398, doi:10.1021/ie801242v (2009).

17   Harmer, M. A. & Sun, Q. Solid acid catalysis using ion-exchange resins. *Applied Catalysis A: General* **221**, 45-62, doi:https://doi.org/10.1016/S0926-860X(01)00794-3 (2001).

18   Bachmann, W. Über einige Bestimmungen des Hohlraumvolumens im Gel der Kieselsäure. *Zeitschrift für anorganische Chemie* **79**, 202-208 (1912).

19   Anderson, J. Structure of silicic acid gels. *Z Physik Chem* **88**, 191-228 (1914).

20   Gurvitsch, L. Physicochemical attractive force. *J Phys Chem Soc Russ* **47**, 805-827 (1915).

21   Gregg, S. J. & Sing, K. S. W. *Adsorption, surface area and porosity*. (Academic Press, 1982).

22   Sliwinska, L. & Davis, B. H. The Gurvitsch Rule: An Example of a Rule Misnamed? *Ambix* **34**, 81-88, doi:10.1179/amb.1987.34.2.81 (1987).

23   Kunin, R., Meitzner, E., Oline, J., Fisher, S. & Frisch, N. Characterization of amberlyst 15. macroreticular sulfonic acid cation exchange resin. *Industrial & Engineering Chemistry Product Research and Development* **1**, 140-144 (1962).

24   Houston, A. N. *et al.* Quantification of the pore size distribution of soils: Assessment of existing software using tomographic and synthetic 3D images. *Geoderma* **299**, 73-82, doi:https://doi.org/10.1016/j.geoderma.2017.03.025 (2017).

Appendix

Figure Legend:

Figure 1: Illustrated evapoporometry workflow
Samples were immersed in volatile fluid (2-propanol) for two hours to ensure complete saturation and pore filling, then secured to the base of a custom-fabricated PTFE test cell (ID = 35 mm). A small amount of volatile fluid (<500 µL) was further added to the bottom of the test cell overlying the sample to produce a standing layer of fluid. Evaporative mass loss from the test cell is then monitored at stable ambient temperature (25 °C) using an analytical balance with a resolution of 10 µg. Raw mass and acquisition time data were input into a standalone python application to yield mean pore diameter, pore diameter distribution, and estimated surface area.

Figure 2: Standardization of data processing in Python enables rapid and facile

interpretation of evapoporometry mass loss data

A standalone windows-executable Python application with graphic user interface (Evapore) was developed for evapoporometry data analysis wherein the user is prompted to (a) specify the evaporating fluid used, the constant temperature at which the mass loss experiment was conducted, as well as the data acquisition interval from the analytical balance used. The user loads a headerless .XLSX file containing mass data in the first column, after which Evapore renders an interactive graph (b) where the user is prompted to select the period of steady-state evaporation corresponding to evaporation of the fluid layer overlying the sample. Evapore then displays threshold value of evaporation rate at which pore draining is considered to begin (c, red line), and the user selects the first data point that is continuous with the remainder of the curve. Based on the physical properties of the fluid used, temperature, and acquisition interval, Evapore computes both an average pore diameter and pore diameter distribution which are rendered to the user, with the user prompted to save final result data in .CSV format, compatible with most statistical software.

Figure 3: Surface morphology of assessed porous materials
Evapoporometric pore size data were assessed for (a) Anodisc membranes with a nominal mean pore diameter of 100 nm and (b) Amberlyst 15 ion exchange resin beads with nominal mean pore diameter of 30 nm.

Figure 4: Assessment of pore diameter agrees with nominal properties of porous materials
(a) Evaporometric mean pore diameters assessed by Evapore correlate strongly (B) with nominal reported N_2 adsorption pore diameters (slope significantly different from zero, $p < 0.0001$), with pore diameter distributions for (c) Anodisc 13 membranes, (d) Amberlyst 15 ion exchange resin, and (e) Anodisc 47 membranes.

Figure 5: Estimation of material surface area by evapoporometry

Assessment of material surface area by evapoporometry via the Bachmann-Anderson-Gurvitsch rule demonstrated the expected inverse trend of surface area relative to pore diameter, but appears to overestimate surface area relative to BET ($\dagger$, 42.5 m^2/g for Amberlyst 15 ion exchange resin).
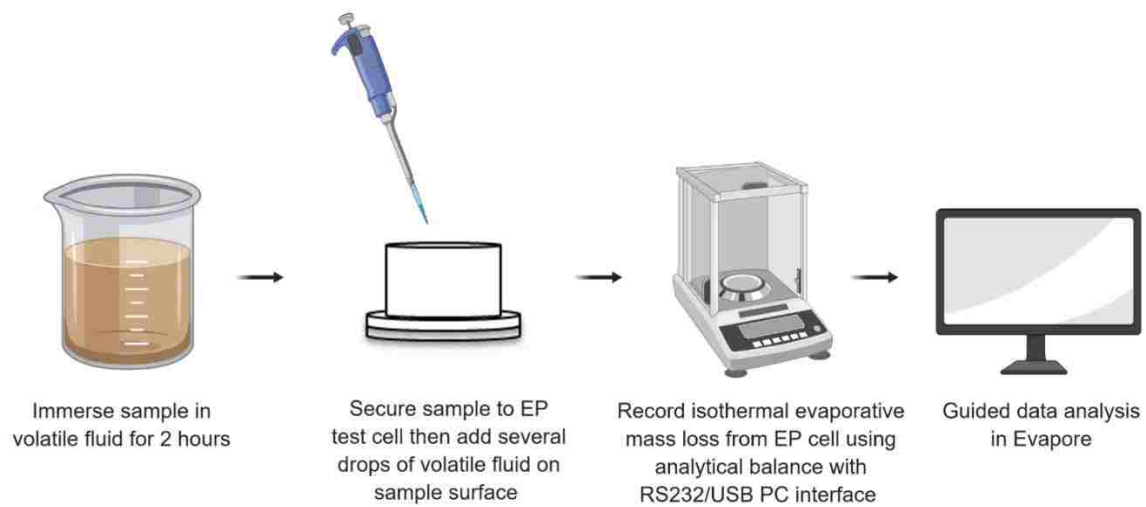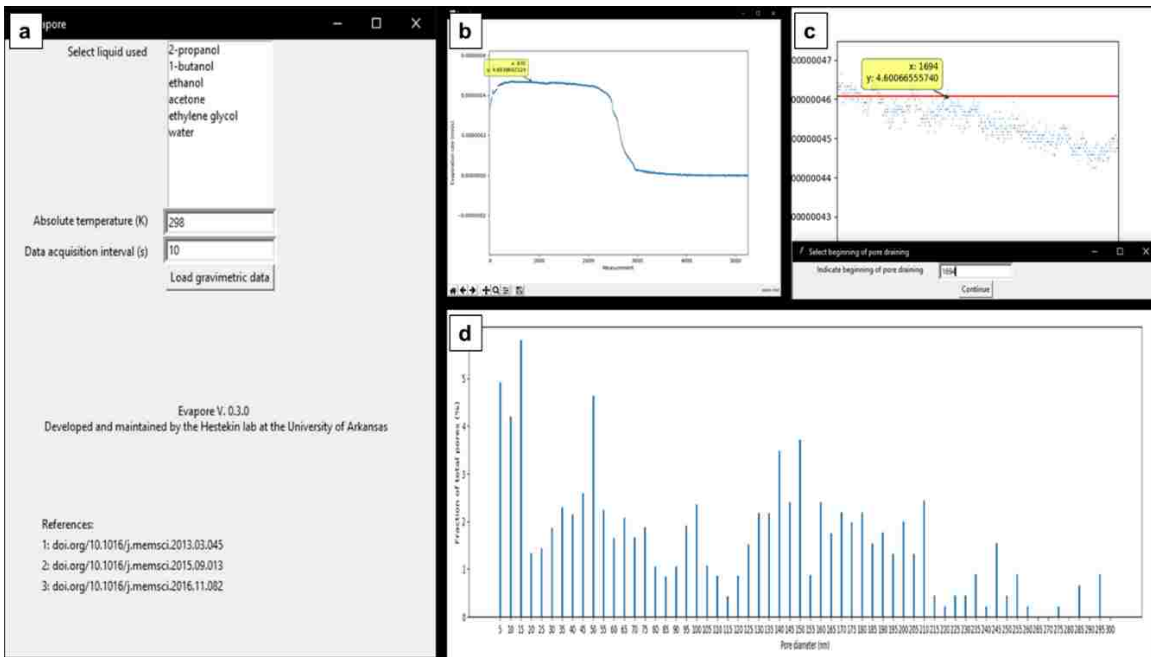
Immerse sample in volatile fluid for 2 hours

Secure sample to EP test cell then add several drops of volatile fluid on sample surface

Record isothermal evaporative mass loss from EP cell using analytical balance with RS232/USB PC interface

Guided data analysis in Evapore
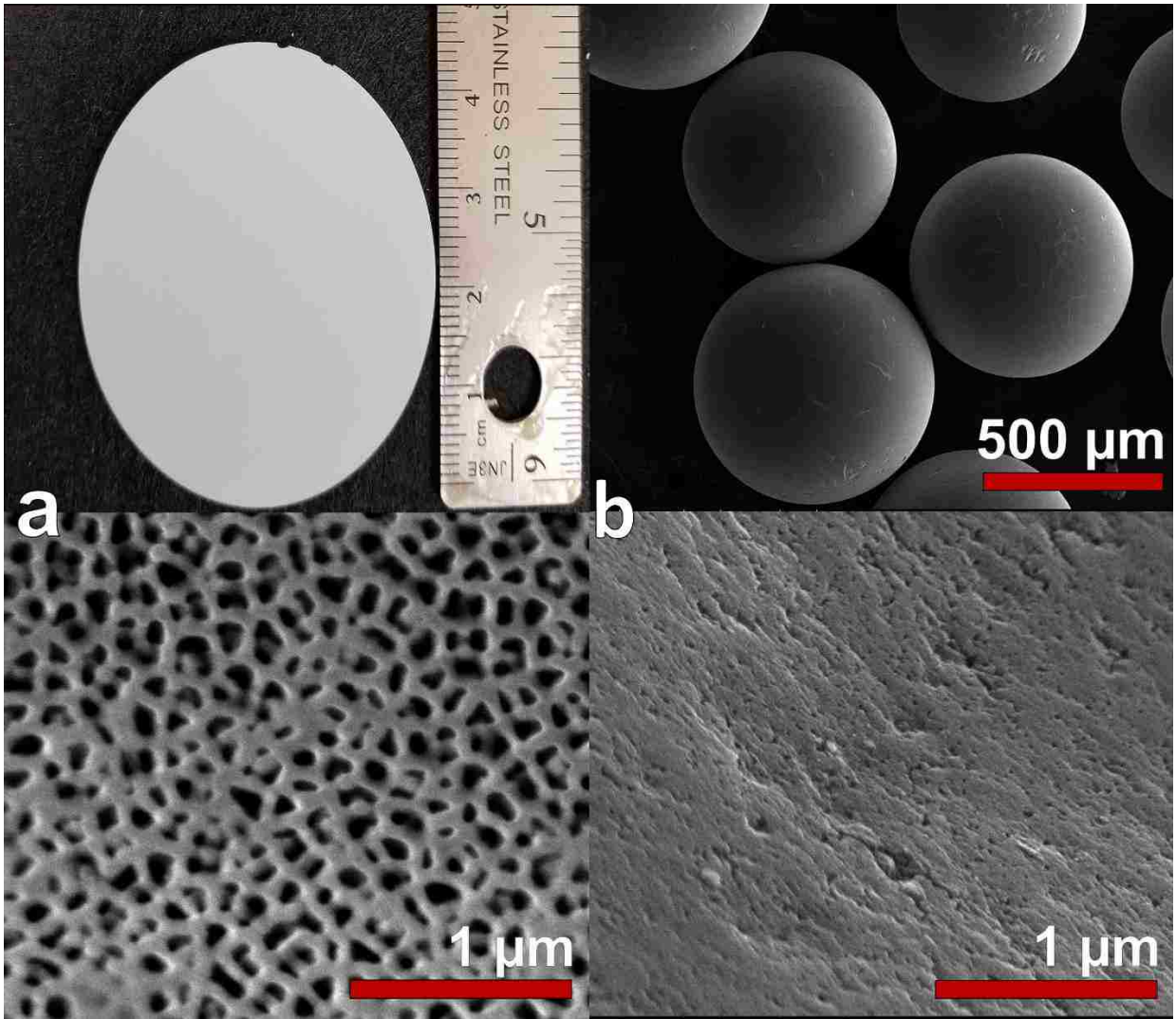
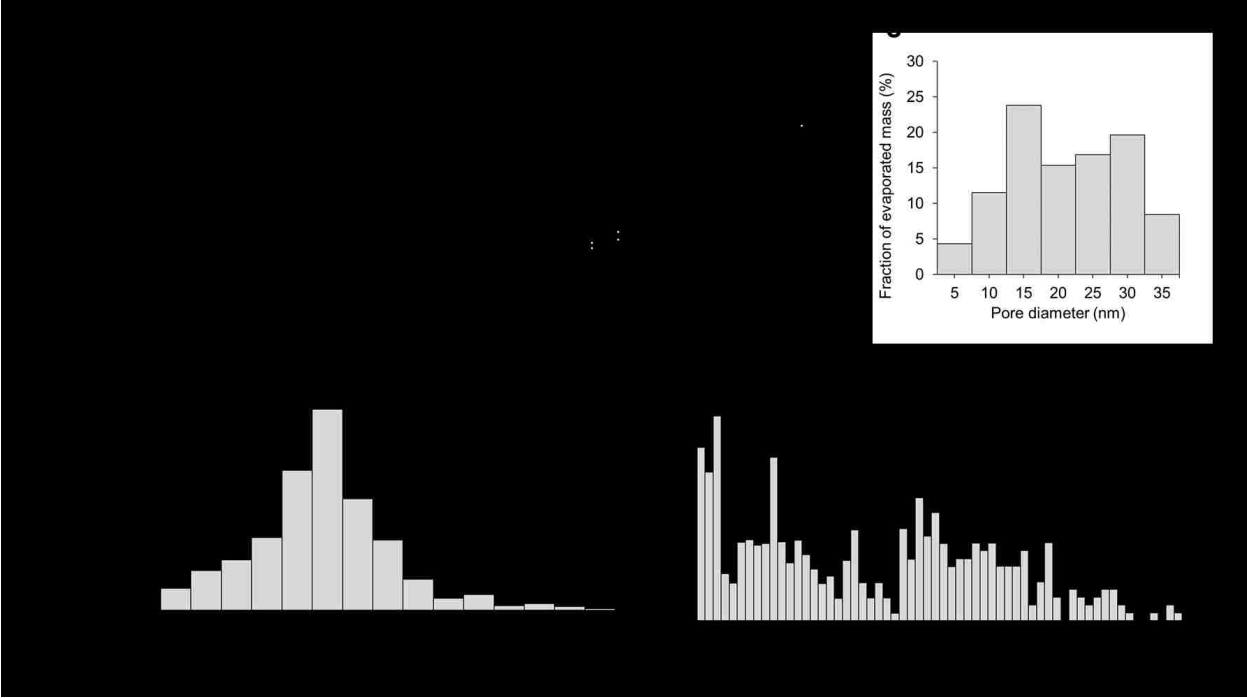Figure 1

Figure 2

a

b

500 µm

1 µm

1 µm

Figure 3

Figure 4

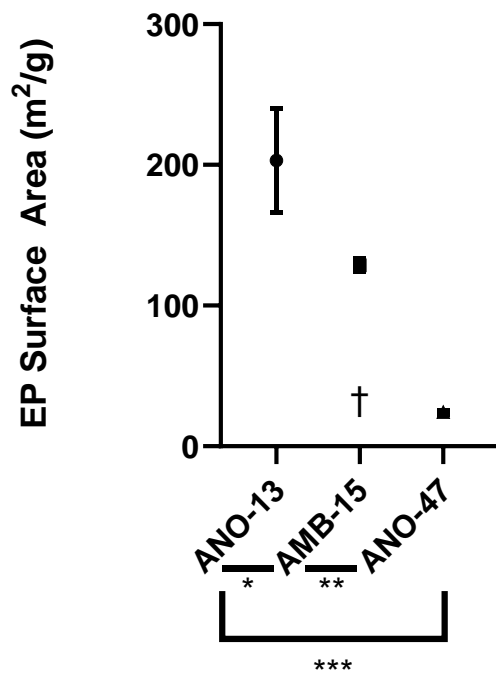Figure 5

Chapter 5

Transcriptome profiling of volumetric muscle loss repair strategies reveals synergetic neuroregenerative signaling

Kevin Roberts[1], John Kim[2], Grady Dunlap[2], Jamie Hestekin[3], and Jeffrey C. Wolchok[2]

[1] Cell and Molecular Biology Program, University of Arkansas, Fayetteville, AR

[2] Department of Biomedical Engineering, University of Arkansas, Fayetteville, AR

[3] Ralph E Martin Department of Chemical Engineering, University of Arkansas, Fayetteville, AR

Corresponding Author:

Jeff Wolchok

125 Engineering Hall

Department of Biomedical Engineering

University of Arkansas

Fayetteville, AR 72701

jwolchok@uark.edu

479 575-2850

Abstract

Volumetric muscle loss overwhelms skeletal muscle's ordinarily capable regenerative machinery, resulting in fibrosis and severe functional deficits which have defied clinical repair strategies. In this manuscript we pair the early *in vivo* functional response to treatment of volumetric muscle loss injury using three separate implant strategies to the global transcriptome response for each group. We demonstrate that an implant comprising an allogeneic decellularized skeletal muscle scaffold seeded with autologous minced muscle expedites functional recovery from volumetric muscle loss concurrent with a remarkable increase in neuritogenesis and axon guidance transcription in the early period following injury and repair, with an unexpected absence of coordinated myogenic transcription. Importantly, these responses are observed only when both scaffolding and cellular components are delivered, with the combinatorial group recovering 54.7% of the contractile force lost to injury at two weeks post-injury, compared to -11.8% and 11.3% among groups receiving minced muscle or scaffolding only, respectively. The functional recovery and transcriptome profile observed with this treatment strategy demonstrate an unexplored yet critical synergy between scaffolding and cells during muscle regeneration and invites exploration of the underappreciated role of peripheral neuroregeneration in volumetric muscle loss.

A. Introduction

Skeletal muscle exhibits an innate ability to regenerate small amounts of functional tissue following minor traumas including strains and contusions.[1] The immediate response to mild muscle injury consists of partial necrosis of damaged myofibers and their degradation by neutrophils, followed by migration of macrophages to the injury which continue to degrade necrotic tissue.[2] Hepatocyte growth factor released from injured muscle matrix promotes satellite cells residing between myofibers to reenter cell cycle, proliferate, and migrate to sites of injury as myoblasts, after which they undergo fusion to form nascent myofibers.[3-5] Over the course of several days, the community of macrophages present will shift toward a range of phenotypes secreting signals promoting myoblast differentiation and connective tissue deposition by fibroblasts.[6] Alternatively, in the case of volumetric muscle loss (VML), satellite cell recruitment and differentiation are overwhelmed by inflammatory signaling and the destruction of the basal lamina, leaving fibroblasts as the predominant cell population in the wound during the repair and remodeling phase. Consequently, VML injuries result in the formation of non-contractile scar tissue which prevents the intrusion of nascent myofibers, contributing to a permanent deficit in muscle force.

There exists no consensus on a standard of care for regenerating lost muscle, due to a lack of proven therapies and the heterogeneous presentation of VML injuries. Exploratory biomaterials for treatment of VML generally attempt to inhibit fibrosis and promote myoblast differentiation; typically composed of decellularized skeletal muscle (DSM) or porcine small intestinal submucosa, use of these scaffolds in isolation has yielded mixed results.[7-11] Particularly promising in preclinical study are combinatorial therapies in which precursor cells are combined with tissue scaffolds fitted to the geometry of the wound and directly implanted.[12-15] One such

cell delivery method of interest to our group and others[16-22] is the use of minced muscle sourced from small portions of autologous donor muscle, a clinically translatable source of precursor cells.[23] Cells from minced muscle (MM) autografts contribute directly to fiber regeneration following VML, yet have achieved only modest functional recovery when used in isolation.[24] What is especially intriguing are the functional improvements that can be achieved when a DSM matrix and MM autograft are used in combination. Founded on the premise that the matrix provides an enabling substrate for regeneration by codelivered cells while minimizing the amount of donor tissue required, this implant strategy has recovered half of muscle force lost to VML in preclinical models[25].

The breadth of molecular modes by which these combinatorial therapies may coordinate force recovery remains unclear, particularly during the early weeks following injury. The lower level of recovery occurring in the presence of allogeneic matrix or minced muscle alone emphasizes the importance of a multifactorial approach to VML treatment, and suggests a biomolecular synergy between these components which to date has not been explored in depth. Here we profile the transcriptome-wide responses of VML-injured tissue to scaffolding and cell delivery strategies in isolation and combination to better assess early regulatory changes potentially mediating differences observed in functional outcome between implant schemes. Clarifying the effects of these therapies on the complex inflammatory, fibrotic, and regenerative networks in the early period following injury contributes to a foundational understanding of VML pathobiology upon which to further refine VML repair strategies for the clinic.

B. Results

Minced muscle-loaded decellularized muscle improves early VML functional outcome

Ablation of the rat tibialis anterior resulted in defects clearly visible at 3 and 14 days post injury (DPI) (**Figures 1** and **2**). While no clear differences were noted in the gross appearance of VML and MM-treated muscles, DSM and DSM+MM implants remained intact in the site of the defect, with the DSM+MM appearing better integrated with the muscle than DSM. No significant differences in animal growth were observed. Masses of excised TA muscles were statistically indistinguishable from excised contralateral uninjured TA across all groups at 3 DPI, while the mean mass of VML and MM-treated TA were significantly lower relative to normal at 14 DPI (78.5% of normal mass with $p = 0.0181$ and 80.6% of normal mass with $p = 0.0351$, respectively).

Unrepaired, repaired, and uninjured contralateral limbs were assessed for peak tetanic force output at both time points. At 3 DPI, MM and DSM+MM -treated groups exhibited significantly lower force output (N/kg body weight) than uninjured contralateral muscles (64.2% and 41.6% of uninjured limb force, respectively). Unrepaired, MM, and DSM treatments exhibited significantly lower force output (N/kg bw) at 14 DPI relative to uninjured muscles (53.6%, 48.2%, and 58.8% of uninjured limb force, respectively) while muscles treated with minced muscle loaded onto decellularized muscle matrix (DSM+MM) exhibited a force outcome not statistically different from uninjured limbs (79% of normal limb force, $p = 0.0648$) (**Figure 2B**).

Muscle transcriptomes vary sharply with repair strategy at two weeks post-injury

Analysis of RNA-seq data in EdgeR revealed a cumulative total of 2686 differentially expressed genes (DEGs) across all groups relative to controls (**Figure 3**). A broadly similar pattern of gene expression was observed across all groups at 3 DPI, with the notable exception of a marked downregulation of a broad array of macromolecule metabolism genes within the MM group (Figure 3B-C). The 3 DPI muscle transcriptomes were otherwise largely dominated by upregulation of genes categorized by gene ontology enrichment analysis as related to cell migration and regulation of the immune response.

Gene expression within the unrepaired and MM-repaired groups at 14 DPI demonstrated a broad return to baseline levels. The VML14 group exhibited upregulation of 52 genes, 2 of which (LIPG and RPLP1) were unique to this group. Of the remaining 50 transcripts, gene ontology enrichment identified 22 associated with cell differentiation and 6 related to skeletal muscle tissue development. The MM14 group demonstrated upregulation of only 2 transcripts, CAV1 and SCD. CAV1 –the only transcript commonly upregulated among all 14 DPI groups- is a key constituent of caveolae, a subtype of lipid raft involved in transmembrane signaling[26], endocytosis[27], mechanoprotection across several cell types[28], and sarcolemmal organization.[29] SCD encodes the rate-limiting enzyme for the synthesis of monounsaturated fatty acids, is associated with fat metabolism and deposition of fat in skeletal muscle[30], and is notably the only differentially expressed gene upregulated in all groups regardless of time point.[31]

While the DSM14 and DSM+MM14 groups demonstrated differential expression of 832 genes largely related to the acute inflammatory response also differentially expressed by all 3 DPI groups, 52 DEGs were shared only by DSM14, with 90 DEGs unique to DSM+MM14 alone. Extracellular matrix organization, cell surface receptor signaling, and axonogenesis gene

ontology categories comprise 8, 17, and 6 of the 52 DEGs shared by these two groups, respectively. Regulation of cell communication, anatomical structure morphogenesis, and membrane protein localization comprised the major gene ontology categories overrepresented among the 90 DEGs unique to DSM+MM14. The DSM14 and DSM+MM14 groups each exhibited remarkable upregulation of transcripts with some role in cell movement annotated by IPA, with 424 and 540 cell movement DEGs, respectively.

Myogenesis and angiogenesis transcription are generally unaffected by VML repair

Assessment of all groups for the classic markers of precursor cell myogenesis indicate a lack of coordinated myogenesis signaling with the exception of an observation of upregulated MYF5 and MYOG within the DSM group relative to uninjured controls at 14 DPI (p = 0.004 and p = 0.0130, respectively). (**Figure 4A-B**) Assessment for angiogenesis markers indicate nonexpression across all groups for the angiogenic VEGFa and no consistent differential expression for associated angiogenic transcripts. (**Figure 4C-D**) Ingenuity Pathway Analysis predicted no significant changes to myogenesis or angiogenesis at the pathway level.

Profound upregulation of ECM and phagocytosis transcripts persists in DSM and DSM+MM repair

Transcripts for many well-described matrix structural constituents and enzymes, including fibrillary collagens, collagen nucleators, and matrix metalloproteinases, were consistently found by EdgeR to be profoundly upregulated in both the DSM and DSM+MM groups at 14 DPI (**Figure 5**). Ingenuity Pathway Analysis identified significant upregulation within the hepatic fibrosis canonical pathway for each (p = 1.04E-14 with 39 DEGs and 5.13E-18 with 49 DEGs, respectively). IPA also identified a general upregulation of transcripts with some role in fibrogenesis for the DSM (p = 2.87E-19 with 89 DEGs) and DSM+MM (p = 3.57E-

27 with 119 DEGs) groups at this timepoint, respectively. Upregulation of the *Fcγ* receptor-mediated phagocytosis pathway was further identified (p = 1.62E-13 with 26 DEGs and p = 1.83E-13 with 29 DEGs, respectively, **Figure 6**). Further, the Cell Movement category of transcripts was found by Ingenuity Pathway Analysis (IPA) to be significantly upregulated for all groups at 3 DPI and the DSM (p = 2.06E-80) and DSM+MM (p = 5.26E-101) groups at 14 DPI.

Expression of neuritogenesis and axonogenesis associated genes is upregulated in DSM+MM repair of VML

Ingenuity Pathway Analysis identified significant upregulation (p = 2.96E-03) of the Neuritogenesis Diseases and Functions annotation within the DSM+MM group at 14 DPI, with six genes predicted to be upregulating neuritogenesis. (**Figure 7A-B**). These include RELN, S100B, AHRGEF25, DLG4, GEM, and PMP22, all of which are known to be associated with neurite outgrowth.[32-37] The DSM-only group also exhibited significant upregulation of ARHGEF25, which has also been shown to promote skeletal muscle regeneration in mouse tibialis anterior,[38] while other groups were insignificant for all neuritogenesis related transcripts at the 14 DPI timepoint. Further, Gene ontology enrichment analysis revealed 6 additional genes upregulated in both the DSM14 and DSM+MM14 groups related to axonogenesis, including ROBO2, BRSK1, MT3, RND2, DCX, and DIXDC1 (**Figure 7C-D**). In particular the binding of ROBO2 receptor with its ligand Slit2 is necessary for the normal bundling of nascent axons during muscle innervation.[39] When the $\log_2$FC threshold for calling differential expression was lowered to 1.0, IPA identified substantial changes in the Axonal Guidance Signaling canonical pathway in several groups, with 185, 182, 139, and 121 differentially expressed genes in the 3 DPI VML, MM, DSM, and DSM+MM groups, respectively. In contrast, at 14 DPI changes in

axonal guidance signaling were observed only in the DSM and DSM+MM groups, with 78 and 116 differentially expressed genes, respectively.

C. Discussion

In this work we have profiled the global transcriptome expression of the tibialis anterior cell community in response to volumetric muscle loss (VML) and subsequent biomaterials-based repair strategies. A standard of care for VML remains elusive; implantation of autologous minced muscle grafts is capable of promoting some degree of repair but requires prohibitively large amounts of donor tissue for extensive VML wounds. An emerging alternative is the use of extracellular matrix scaffolds; however, many of those piloted in the literature thus far have mixed impacts on functional outcome. Intriguingly, the application of autologous minced muscle (MM) pastes to decellularized muscle matrix (DSM) prior to implantation has been shown to restore half of the peak contractile force lost to VML (81% of uninjured peak contractile force vs 62%), while other minced muscle or ECM grafts result in only modest improvement to force outcomes.[25] Our observation of significant functional recovery (79% of uninjured limb force) in groups treated with DSM+MM at 14 days post-injury corroborates this finding and further suggests that a substantial fraction of force recovery mediated by this combinatorial repair occurs relatively early in the wound-healing process, a novel finding not seen in previous investigations potentially due to assessment of recovery at extended time points (8+ weeks post-injury). Our data suggest that neither the MM or DSM components in isolation are sufficient to facilitate this expeditious force recovery; it is only when combined that they act synergistically to restore force in this manner.

Intriguingly, confounding the force recovery seen with DSM+MM repair is the observation of no coordinated changes in myogenesis nor angiogenesis signaling, suggesting that

the recovery observed is unlikely to be mediated by myofiber regeneration alone. Chen and Walters have suggested that muscle-derived ECM mediates force recovery in part through the provision of a physical bridge through which force can be transmitted across the site of injury.[40] Corona *et al* further show that relative to untreated VML injuries, implantation of muscle ECM biases collagen deposition toward the defect site rather than intramuscular deposition and prevents reductions in fiber cross-sectional area, suggesting a protective effect of implanted muscle ECM against muscle atrophy following injury.[41] Our data indicate that the DSM component causes substantial and persistent upregulation of transcripts for the chief fibrillary collagens, collagen nucleators[42], as well as collagen-degrading matrix metalloproteinases, all participants in the remodeling of ECM.[43] This combined with the profound upregulation of phagocytosis and cell movement related genes illustrates a complex environment within the wound in the weeks following VML; while decellularized skeletal muscle has been shown to promote myogenesis by acting as a substrate for satellite cell migration and differentiation,[44] the absence of myogenic signaling, early onset of force recovery within the DSM+MM group, and statistically significant force deficit observed for the DSM-only group in this study suggest that non-myogenic processes are contributing to VML recovery in the case of DSM+MM repair.

Our observation of substantial upregulation of neuritogenesis and axonogenesis related transcripts suggests a possible neurologic involvement in the efficacy of DSM+MM repair of VML. Further, when the $\log_2$(FC) threshold for calling differential gene expression is lowered from 1.5 to 1, IPA detected 116 differentially expressed genes in the DSM+MM14 group within the Axon Guidance Signaling canonical pathway. Further, the significant deficits in terminal muscle mass, contractile force, and lack of neuroregenerative transcription among unrepaired and minced muscle repaired groups are consistent with the phenomenon of denervation-induced

muscle atrophy.[45] While most VML investigations in the literature have focused on the influence of myofiber atrophy, myogenesis, or immune involvement, Corona *et al* recently demonstrated that VML results in chronic axotomy of ~69% of motoneurons innervating the tibialis anterior, concurrent with a large deficit in muscle force.[46,47] Crucially, it is shown that while motoneurons within the muscle are dramatically affected by VML, this is not accompanied by death of associated CNS neurons, suggesting that promoting the innate ability of peripheral nerves to regenerate within the muscle may improve the functional outcome of VML. Further, Given that skeletal muscle following denervation is host to a variety of cells including Schwann cells[48], it may be the case that Schwann cells from the minced muscle graft are better able to participate in functional axonogenesis when combined with the DSM substrate which bridges normal muscle with the wound. As with normal muscle, the DSM exhibits a longitudinally aligned character; several studies suggest that scaffold alignment is a key factor in expediting axonogenesis[49-52] with a recent finding that treatment of VML with a combination of aligned scaffolds and rehabilitative exercise increases the formation of mature neuromuscular junctions.[53] Further study is required to better ascertain whether the aligned character of muscle matrix combined with autologous minced muscle may mediate functionally relevant nerve regeneration following VML.

Our observation of prolonged phagocytosis related transcription suggests a significant presence of macrophages or other phagocytic cell types at the implant site. While the recruitment of macrophages as part of the acute wound response and foreign body response to implants are well described, direct participation of these cells in a variety of regenerative processes are becoming better appreciated.[54,55] Intriguingly, Stratton *et al* recently demonstrated that macrophages regulate Schwann cell function during regeneration, with ablation of macrophages

associated with the injury site resulting in marked reductions in conduction velocity and remyelination mediated by the absence of macrophage-derived GAS6.[56] Recent research suggests that aligned scaffolds contribute to peripheral nerve regeneration by polarizing macrophages toward a pro-regenerative phenotype, enhancing the proliferation and migration of Schwann cells, again suggesting a potential role for the aligned character of minced muscle coated DSM in mediating force recovery in VML.[57]

Our data suggest the involvement of several key neuritogenesis, axonogenesis, and axon guidance transcripts in VML repair in the early period following injury; interrogation of these and other factors influencing nerve regeneration within injured skeletal muscle is relatively unexplored, and may yield fruitful targets exploitable by a combination of drug and biomaterials-based therapies. Studies of global transcriptome expression have revealed that the cellular community of skeletal muscle expresses a massive quantity of alternatively spliced transcripts, the identities and quantities of which change substantially during the course of myogenesis.[58] The levels of these isoforms are determined largely by the splicing event –not by changes in transcription- resulting in these changes being unassessed in standard differential expression analyses.[59] Clearly, functional analysis of alternatively spliced isoforms expressed in skeletal muscle during injury and intervention will develop a fuller understanding of muscle pathobiology and repair. It is anticipated that investigations in this area will benefit greatly from high sequencing depth and the application of cell sorting technologies for emerging single-cell RNA sequencing (scRNA-seq), potentially allowing for the crucial distinction of expression between the many cell types present in the muscle during injury and wound-healing.

Ultimately, VML injuries exhibit significant heterogeneity. Therefore, a range of clinical strategies incorporating effective biomaterials, drugs, and physical rehabilitation will be required

to best address the complications of this challenging condition. As the expense of RNA-sequencing technologies decreases and the ease of downstream data analysis increases, whole transcriptome expression profiling will be an invaluable tool in guiding the development of promising therapies for the treatment of VML.

D. Methods

Animals

26 Sprague Dawley rats (pre-surgical mass ~350 g) were used in this study. Buprenorphine (0.1 mL at 0.3 mg/mL) was administered to all rats subcutaneously for postoperative analgesia and access to Rimadyl was provided at up to 1 mg per day for seven days post-injury. Food and water were provided *ad libitum*. All animal procedures were approved by the Institutional Animal Care and Use Committee of the University of Arkansas.

Injury and repair

VML injuries were created in rats using an established VML model.[60] Briefly, Lateral incisions were made on the lower left legs of Sprague Dawley rats weighing ~350 g, separating skin and fascia to expose the TA muscle. An 8 mm biopsy punch was used to remove muscle tissue (~100 mg) from the middle third of the TA to a depth of 3 mm. Subsets of rats underwent repair of VML injury with autologous minced muscle grafts (MM), SDS/DNase I/RNase A decellularized skeletal muscle prepared from rat tibialis anterior (DSM), and a combination of DSM and MM (DSM+MM). MM autografts were prepared during surgery by mincing the biopsied tissue using microscissors. Fascia and skin were closed using interrupted stiches with 6-0 Vicryl sutures. Buprenorphine every administered subcutaneously every eight hours for post-operative analgesia.

Functional assessment

Peak tetanic contractile force of injured and contralateral normal limbs was measured *in situ* at three days and fourteen days post-injury as previously described.[25] Briefly, peroneal nerves of anesthetized rats were stimulated (150 Hz, 0.1 ms pulse width, 400 ms pulse train) by an S88 pulse stimulator (Grass Technologies, West Warwick) to induce contraction of the tibialis anterior muscle. Measurement of raw force output (N) was enabled by securing the foot of the limb to a force transducer system (Aurora Scientific, Ontario) with surgical tape. Peak tetanic force for each limb was calculated by the mean of three contractions and normalized to animal mass (N/kg body weight).

RNA preparation and sequencing

TA muscles were harvested from euthanized rats at three days and fourteen days post-injury, snap frozen on liquid nitrogen, and stored at -80°C pending RNA isolation. Tissues were thawed and homogenized for 15 s at room temperature. Total RNA was isolated using the Purelink RNA Mini Kit (ThermoFisher). RNA concentration was determined by nanodrop spectrophotometry, with RNA quality (28S/18s >2, RIN >7) confirmed using a Tapestation (Agilent Technologies). cDNA libraries were sequenced on the BGISeq-500 platform to a mean depth of 20,000,000 reads per library.

RNA-seq data analysis

RNA sequencing reads were mapped to the *Rattus norvegicus* genome (RGSC build 6.0) from USCS using the 2-pass STAR protocol[61]. Reads were quantified using FeatureCounts[62], followed by analysis of differential expression and normalization in edgeR[63]. Differential expression was called using a false discovery rate (FDR) cutoff of 0.05 and absolute minimum fold change of 1.5. Visualization of group intersections for differential gene expression was performed using UpsetR[64]. Enrichment analysis of gene sets was performed against the

Biological Process Gene Ontology and KEGG databases in ShinyGO.[65] Pathway level analysis was also performed using Ingenuity Pathway Analysis (Qiagen)[66].

Statistics

Statistical analyses for assessment of muscle force were performed using Prism 7 (Graphpad, La Jolla, California), using repeated measures ANOVA with post-hoc Dunnett's test. Assessment of significance for differential gene expression was performed using EdgeR with TMM normalization of read counts and adjustment of p-values for multiple comparisons by the Benjamini-Hochberg procedure. Significance was accepted at $P \leq 0.05$ (*) $P \leq 0.01$ (**), $P \leq 0.001$ (***), and $P \leq 0.0001$ (****). Quantitative data are displayed as mean + standard deviation.

Data availability

All RNA-sequencing files were deposited in the Gene Expression Omnibus (https://www.ncbi.nlm.nih.gov/geo/) under accession number GSE125896. All other data supporting the findings of this study are available from the authors upon reasonable request.

Acknowledgements

References

1   Larouche, J., Greising, S. M., Corona, B. T. & Aguilar, C. A. Robust inflammatory and fibrotic signaling following volumetric muscle loss: a barrier to muscle regeneration. *Cell Death & Disease* **9**, 409, doi:10.1038/s41419-018-0455-7 (2018).

2   Tidball, J. G. Regulation of muscle growth and regeneration by the immune system. *Nature Reviews Immunology* **17**, 165, doi:10.1038/nri.2016.150 (2017).

3   Allen, R. E., Sheehan, S. M., Taylor, R. G., Kendall, T. L. & Rice, G. M. Hepatocyte growth factor activates quiescent skeletal muscle satellite cells in vitro. *Journal of cellular physiology* **165**, 307-312 (1995).

4   Sheehan, S. M., Tatsumi, R., Temm-Grove, C. J. & Allen, R. E. HGF is an autocrine growth factor for skeletal muscle satellite cells in vitro. *Muscle & Nerve: Official Journal of the American Association of Electrodiagnostic Medicine* **23**, 239-245 (2000).

5   Tatsumi, R., Anderson, J. E., Nevoret, C. J., Halevy, O. & Allen, R. E. HGF/SF is present in normal adult skeletal muscle and is capable of activating satellite cells. *Developmental biology* **194**, 114-128, doi:10.1006/dbio.1997.8803 (1998).

6   Arnold, L. *et al.* Inflammatory monocytes recruited after skeletal muscle injury switch into antiinflammatory macrophages to support myogenesis. *Journal of Experimental Medicine* **204**, 1057-1069 (2007).

7   Dziki, J. *et al.* An acellular biologic scaffold treatment for volumetric muscle loss: results of a 13-patient cohort study. *Npj Regenerative Medicine* **1**, 16008, doi:10.1038/npjregenmed.2016.8

          https://www.nature.com/articles/npjregenmed20168#supplementary-information (2016).
8   Aurora, A., Corona, B. T. & Walters, T. J. A porcine urinary bladder matrix does not recapitulate the spatiotemporal macrophage response of muscle regeneration after volumetric muscle loss injury. *Cells Tissues Organs* **202**, 189-201 (2016).

9   Ma, J., Sahoo, S., Baker, A. R. & Derwin, K. A. Investigating muscle regeneration with a dermis/small intestinal submucosa scaffold in a rat full-thickness abdominal wall defect model. *Journal of Biomedical Materials Research Part B: Applied Biomaterials* **103**, 355-364, doi:doi:10.1002/jbm.b.33166 (2015).

10   Corona, B. T., Ward, C. L., Baker, H. B., Walters, T. J. & Christ, G. J. Implantation of in vitro tissue engineered muscle repair constructs and bladder acellular matrices partially restore in vivo skeletal muscle function in a rat model of volumetric muscle loss injury. *Tissue Engineering Part A* **20**, 705-715 (2013).

11   L'Heureux, N. & Letourneur, D. Clinical translation of tissue-engineered constructs for severe leg injuries. *Annals of translational medicine* **3**, 134-134, doi:10.3978/j.issn.2305-5839.2015.05.03 (2015).

12   Quarta, M. *et al.* Biomechanics show stem cell necessity for effective treatment of volumetric muscle loss using bioengineered constructs. *npj Regenerative Medicine* **3**, 18, doi:10.1038/s41536-018-0057-0 (2018).

13   Li, M.-T. *et al.* Skeletal Myoblast-Seeded Vascularized Tissue Scaffolds in the Treatment of a Large Volumetric Muscle Defect in the Rat Biceps Femoris Muscle. *Tissue Engineering Part A* **23**, 989-1000 (2017).

14   Merritt, E. K. *et al.* Repair of traumatic skeletal muscle injury with bone-marrow-derived mesenchymal stem cells seeded on extracellular matrix. *Tissue Engineering Part A* **16**, 2871-2881 (2010).

15   Machingal, M. A. *et al.* A tissue-engineered muscle repair construct for functional restoration of an irrecoverable muscle injury in a murine model. *Tissue Engineering Part A* **17**, 2291-2303 (2011).

16   Corona, B. T. *et al.* Autologous minced muscle grafts: a tissue engineering therapy for the volumetric loss of skeletal muscle. *American Journal of Physiology-Cell Physiology* **305**, C761-C775 (2013).

17   Rivera, J. Restoring Function after Volumetric Muscle Loss: Extracellular Matrix Allograft or Minced Muscle Autograft. (The Geneva Foundation Tacoma United States, 2017).

18   Gräs, S., Klarskov, N. & Lose, G. Intraurethral Injection of Autologous Minced Skeletal Muscle: A Simple Surgical Treatment for Stress Urinary Incontinence. *The Journal of Urology* **192**, 850-855, doi:https://doi.org/10.1016/j.juro.2014.04.005 (2014).

19   Goldman, S. M. & Corona, B. T. Co-delivery of micronized urinary bladder matrix damps regenerative capacity of minced muscle grafts in the treatment of volumetric muscle loss injuries. *PloS one* **12**, e0186593 (2017).

20   Ward, C. L. *et al.* Autologous minced muscle grafts improve muscle strength in a porcine model of volumetric muscle loss injury. *Journal of orthopaedic trauma* **30**, e396-e403 (2016).

21   Sarrafian, T. L., Bodine, S. C., Murphy, B., Grayson, J. K. & Stover, S. M. Extracellular matrix scaffolds for treatment of large volume muscle injuries: A review. *Veterinary Surgery* **47**, 524-535, doi:doi:10.1111/vsu.12787 (2018).

22   Corona, B. T., Rivera, J. C., Wenke, J. C. & Greising, S. M. Tacrolimus as an adjunct to autologous minced muscle grafts for the repair of a volumetric muscle loss injury. *Journal of Experimental Orthopaedics* **4**, 36, doi:10.1186/s40634-017-0112-6 (2017).

23   M., Y., T., N., M., I., N., A. & M., O. Evaluation of autologous skeletal muscle-derived factors for regenerative medicine applications. *Bone & Joint Research* **6**, 277-283, doi:10.1302/2046-3758.65.bjr-2016-0187.r1 (2017).

24   Corona, B. T., Henderson, B. E. P., Ward, C. L. & Greising, S. M. Contribution of minced muscle graft progenitor cells to muscle fiber formation after volumetric muscle loss injury in wild-type and immune deficient mice. *Physiological reports* **5**, e13249, doi:10.14814/phy2.13249 (2017).

25   Kasukonis, B. *et al.* Codelivery of infusion decellularized skeletal muscle with minced muscle autografts improved recovery from volumetric muscle loss injury in a rat model. *Tissue engineering Part A* **22**, 1151-1163 (2016).

26   Schwencke, C., Braun-Dullaeus, R. C., Wunderlich, C. & Strasser, R. H. Caveolae and caveolin in transmembrane signaling: Implications for human disease. *Cardiovascular research* **70**, 42-49 (2006).

27   Wang, X. M., Kim, H. P., Song, R. & Choi, A. M. K. Caveolin-1 confers antiinflammatory effects in murine macrophages via the MKK3/p38 MAPK pathway. *American journal of respiratory cell and molecular biology* **34**, 434-442, doi:10.1165/rcmb.2005-0376OC (2006).

28   Cheng, J. P. X. & Nichols, B. J. Caveolae: One Function or Many? *Trends in Cell Biology* **26**, 177-189, doi:https://doi.org/10.1016/j.tcb.2015.10.010 (2016).

29   Lo, H. P. *et al.* The caveolin–cavin system plays a conserved and critical role in mechanoprotection of skeletal muscle. *The Journal of Cell Biology* **210**, 833-849, doi:10.1083/jcb.201501046 (2015).

30   Jiang, Z. *et al.* Significant associations of stearoyl-CoA desaturase (SCD1) gene with fat deposition and composition in skeletal muscle. *International journal of biological sciences* **4**, 345-351 (2008).

31   Hodson, L. & Fielding, B. A. Stearoyl-CoA desaturase: rogue or innocent bystander? *Progress in Lipid Research* **52**, 15-42, doi:https://doi.org/10.1016/j.plipres.2012.08.002 (2013).

32   Yagi, T. & Takeichi, M. Cadherin superfamily genes: functions, genomic organization, and neurologic diversity. *Genes & development* **14**, 1169-1180 (2000).

33   Reeves, R. H. *et al.* Astrocytosis and axonal proliferation in the hippocampus of S100b transgenic mice. *Proceedings of the National Academy of Sciences* **91**, 5359-5363 (1994).

34   El-Husseini, A. E.-D., Schnell, E., Chetkovich, D. M., Nicoll, R. A. & Bredt, D. S. PSD-95 involvement in maturation of excitatory synapses. *Science* **290**, 1364-1368 (2000).

35   Leone, A. *et al.* The Gem GTP-binding protein promotes morphological differentiation in neuroblastoma. *Oncogene* **20**, 3217 (2001).

36   Bryan, B. *et al.* GEFT, a Rho-family guanine nucleotide exchange factor, regulates neurite outgrowth and dendritic spine formation. *Journal of Biological Chemistry* (2004).

37   Adlkofer, K. *et al.* Heterozygous peripheral myelin protein 22-deficient mice are affected by a progressive demyelinating tomaculous neuropathy. *Journal of Neuroscience* **17**, 4662-4671 (1997).

38   Bryan, B. A. *et al.* Modulation of muscle regeneration, myogenesis, and adipogenesis by the Rho family guanine nucleotide exchange factor GEFT. *Molecular and cellular biology* **25**, 11089-11101 (2005).

39   Jaworski, A. & Tessier-Lavigne, M. Autocrine/juxtaparacrine regulation of axon fasciculation by Slit-Robo signaling. *Nature neuroscience* **15**, 367-369, doi:10.1038/nn.3037 (2012).

40   Chen, X. K. & Walters, T. J. Muscle-derived decellularised extracellular matrix improves functional recovery in a rat latissimus dorsi muscle defect model. *Journal of plastic, reconstructive & aesthetic surgery : JPRAS* **66**, 1750-1758, doi:10.1016/j.bjps.2013.07.037 (2013).

41   Corona, B. T. *et al.* The promotion of a functional fibrosis in skeletal muscle with volumetric muscle loss injury following the transplantation of muscle-ECM. *Biomaterials* **34**, 3324-3335, doi:10.1016/j.biomaterials.2013.01.061 (2013).

42   Kadler, K. E., Hill, A. & Canty-Laird, E. G. Collagen fibrillogenesis: fibronectin, integrins, and minor collagens as organizers and nucleators. *Current Opinion in Cell Biology* **20**, 495-501, doi:https://doi.org/10.1016/j.ceb.2008.06.008 (2008).

43   Caley, M. P., Martins, V. L. C. & O'Toole, E. A. Metalloproteinases and Wound Healing. *Advances in wound care* **4**, 225-234, doi:10.1089/wound.2014.0581 (2015).

44   Urciuolo, A. *et al.* Decellularised skeletal muscles allow functional muscle regeneration by promoting host cell migration. *Scientific Reports* **8**, 8398, doi:10.1038/s41598-018-26371-y (2018).

45   Jackman, R. W. & Kandarian, S. C. The molecular basis of skeletal muscle atrophy. *American Journal of Physiology-Cell Physiology* **287**, C834-C843, doi:10.1152/ajpcell.00579.2003 (2004).

46   Corona, B. T. *et al.* Impact of volumetric muscle loss injury on persistent motoneuron axotomy. *Muscle & Nerve* **57**, 799-807, doi:doi:10.1002/mus.26016 (2018).

47   Quarta, M. Volumetric muscle loss: Including nerves into the equation. *Muscle & nerve* **57**, 705-706 (2018).

48   Murray, M. A. & Robbins, N. Cell proliferation in denervated muscle: Identity and origin of dividing cells. *Neuroscience* **7**, 1823-1833, doi:https://doi.org/10.1016/0306-4522(82)90040-9 (1982).

49   Koffler, J. *et al.* Biomimetic 3D-printed scaffolds for spinal cord injury repair. *Nature Medicine*, doi:10.1038/s41591-018-0296-z (2019).

50   Siliang, W. *et al.* Aligned fibrous PVDF-TrFE scaffolds with Schwann cells support neurite extension and myelination in vitro. *Journal of Neural Engineering* **15**, 056010 (2018).

51   Ribeiro-Resende, V. T., Koenig, B., Nichterwitz, S., Oberhoffner, S. & Schlosshauer, B. Strategies for inducing the formation of bands of Büngner in peripheral nerve regeneration. *Biomaterials* **30**, 5251-5259, doi:https://doi.org/10.1016/j.biomaterials.2009.07.007 (2009).

52   Zhang, K., Zheng, H., Liang, S. & Gao, C. Aligned PLLA nanofibrous scaffolds coated with graphene oxide for promoting neural cell growth. *Acta Biomaterialia* **37**, 131-142, doi:https://doi.org/10.1016/j.actbio.2016.04.008 (2016).

53   Nakayama, K. H. *et al.* Rehabilitative exercise and spatially patterned nanofibrillar scaffolds enhance vascularization and innervation following volumetric muscle loss. *npj Regenerative Medicine* **3**, 16, doi:10.1038/s41536-018-0054-3 (2018).

54   Chen, P., Piao, X. & Bonaldo, P. Role of macrophages in Wallerian degeneration and axonal regeneration after peripheral nerve injury. *Acta neuropathologica* **130**, 605-618 (2015).

55   Chen, P. *et al.* Collagen VI regulates peripheral nerve regeneration by modulating macrophage recruitment and polarization. *Acta neuropathologica* **129**, 97-113 (2015).

56   Stratton, J. A. *et al.* Macrophages Regulate Schwann Cell Maturation after Nerve Injury. *Cell Reports* **24**, 2561-2572.e2566, doi:https://doi.org/10.1016/j.celrep.2018.08.004 (2018).

57   Jia, Y. *et al.* Nanofiber arrangement regulates peripheral nerve regeneration through differential modulation of macrophage phenotypes. *Acta Biomaterialia* **83**, 291-301, doi:https://doi.org/10.1016/j.actbio.2018.10.040 (2019).

58   Trapnell, C. *et al.* Transcript assembly and quantification by RNA-Seq reveals unannotated transcripts and isoform switching during cell differentiation. *Nature biotechnology* **28**, 511-515, doi:10.1038/nbt.1621 (2010).

59   Nakka, K., Ghigna, C., Gabellini, D. & Dilworth, F. J. Diversification of the muscle proteome through alternative splicing. *Skeletal Muscle* **8**, 8, doi:10.1186/s13395-018-0152-3 (2018).

60   Wu, X., Corona, B. T., Chen, X. & Walters, T. J. A standardized rat model of volumetric muscle loss injury for the development of tissue engineering therapies. *BioResearch open access* **1**, 280-290 (2012).

61   Dobin, A. *et al.* STAR: ultrafast universal RNA-seq aligner. *Bioinformatics* **29**, 15-21 (2013).

62   Liao, Y., Smyth, G. K. & Shi, W. featureCounts: an efficient general purpose program for assigning sequence reads to genomic features. *Bioinformatics* **30**, 923-930 (2013).

63   Robinson, M. D., McCarthy, D. J. & Smyth, G. K. edgeR: a Bioconductor package for differential expression analysis of digital gene expression data. *Bioinformatics* **26**, 139-140 (2010).

64   Conway, J. R., Lex, A. & Gehlenborg, N. UpSetR: an R package for the visualization of intersecting sets and their properties. *Bioinformatics* **33**, 2938-2940 (2017).

65   Ge, S. & Jung, D. ShinyGO: a graphical enrichment tool for animals and plants. *bioRxiv*, 315150 (2018).

66   Krämer, A., Green, J., Pollard Jr, J. & Tugendreich, S. Causal analysis approaches in ingenuity pathway analysis. *Bioinformatics* **30**, 523-530 (2013).

G. Appendix

Figure Legend:

Figure 1: Creation of VML injuries and subsequent repair strategies.

Rat tibialis anterior muscles were subjected to VML following implant repair strategies including minced muscle (MM), decellularized skeletal muscle (DSM), and a combination of the two (DSM+MM).

Figure 2: Codelivery of decellularized skeletal muscle with minced muscle preserves muscle contractile force.

(**Top**) Gross appearance of tibialis anterior muscles for groups at three and fourteen days post injury (DPI). (**a** and **b**) Tibialis anterior mass (g/kg rat body weight) at three and fourteen DPI, respectively. Electrophysiological measurement of mean peak contractile force of the tibialis anterior for all groups at (**c**) three and (**d**) fourteen DPI, respectively, indicating deficits in functional outcome among VML, MM, and DSM-treated muscles relative to the uninjured contralateral limb at 14 DPI ($p < 0.0001$, < 0.0001, and 0.0003, respectively). DSM+MM exhibited a significant deficit in force at 3 DPI but not 14 DPI. Error bars are presented as $\pm$ standard deviation.

Figure 3: Global transcription within the VML cell community diverges profoundly based on repair strategy.

(**a**) Heatmap of $\log_2 FC$ for all differentially expressed genes (DEGs) across all groups, with hierarchical clustering of gene expression data visualized using one minus Pearson correlation with average linkage. (**b**) Visualization of the top 15 DEG intersections across groups was performed using UpsetR, with (**c**) significantly overrepresented gene sets for the top 3 intersections assessed by querying the Gene Ontology Biological Process database.

Figure 4: Myogenesis and angiogenesis transcription are insensitive to VML repair.

(**a**) Heatmap of $\log_2 FC$ with (**b**) mean $\pm$ standard deviation plots of normalized expression counts for transcript-level markers of myogenesis and (**c**) heatmap of $\log_2 FC$ and (**d**) mean $\pm$ standard deviation plots of normalized expression counts for transcript-level markers of angiogenesis.

Figure 5: Highly upregulated extracellular matrix constituent transcription persists in

DSM and DSM+MM repair.

(**a**) Heatmap of Log_2FC and (**b**) mean ± standard deviation plots of normalized expression counts for extracellular matrix transcripts.

Figure 6: Highly upregulated phagocytosis associated transcription persists in DSM and

DSM+MM repair.

(**a**) Heatmap of Log_2FC and (**b**) mean ± standard deviation plots of normalized expression counts for phagocytosis related transcripts.

Figure 7: **Neuritogenesis and axonogenesis transcription are significantly increased in**

DSM+MM repair

(**a**) Heatmap of Log_2FC with (**b**) mean ± standard deviation plots of normalized expression counts for transcript-level markers of neuritogenesis and (**c**) heatmap of Log_2FC with (**d**) mean ± standard deviation plots of normalized expression counts for transcript-level markers of axonogenesis.

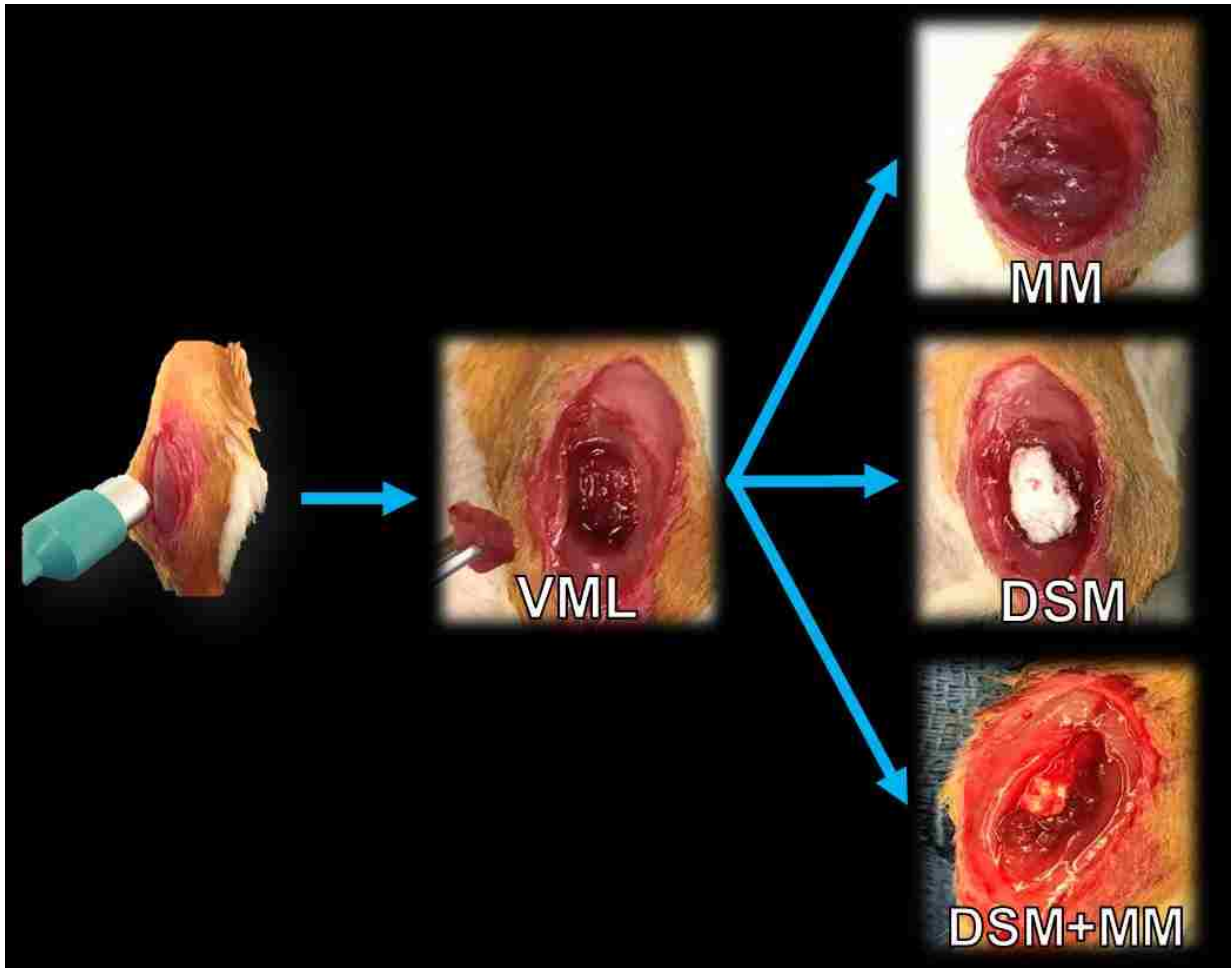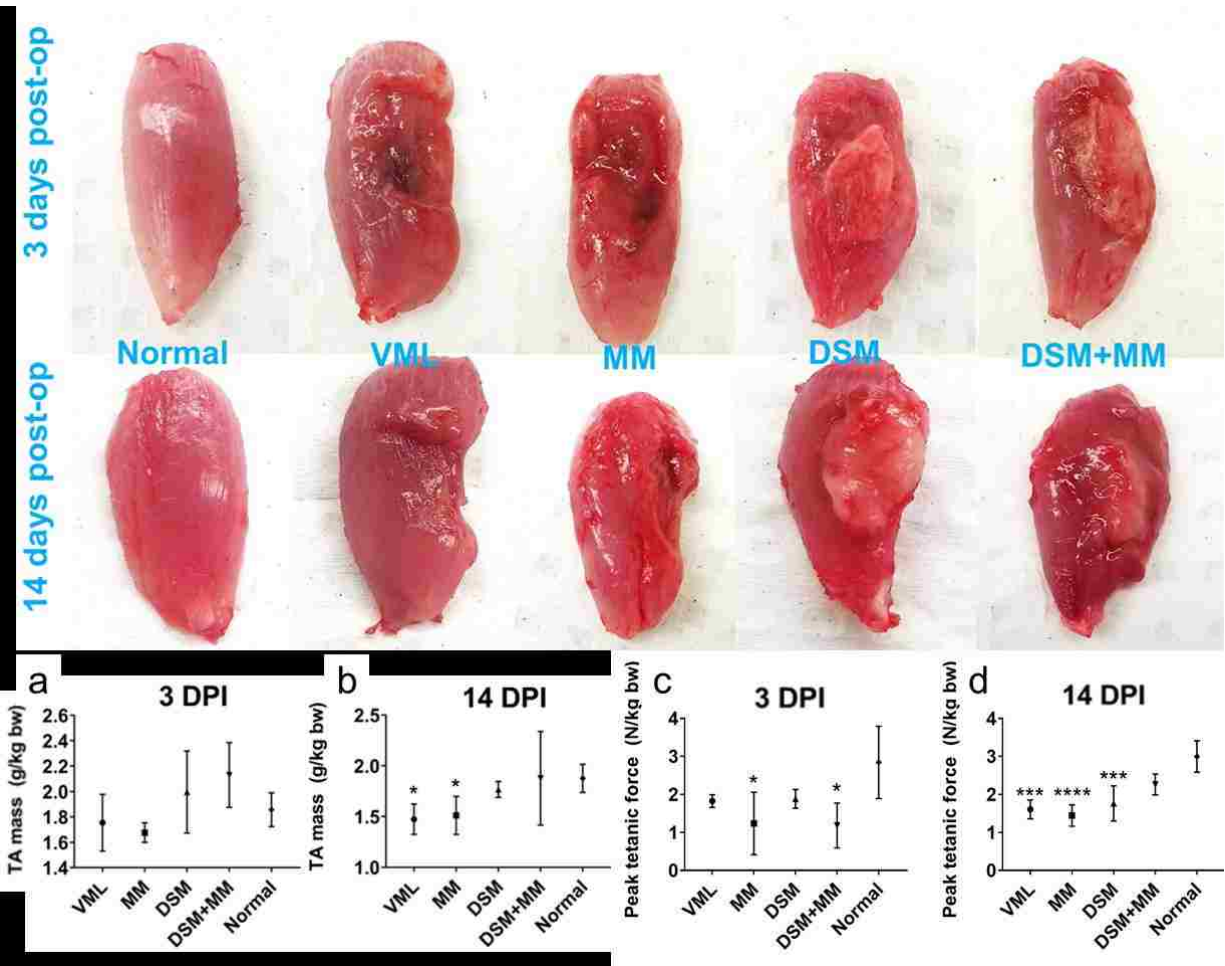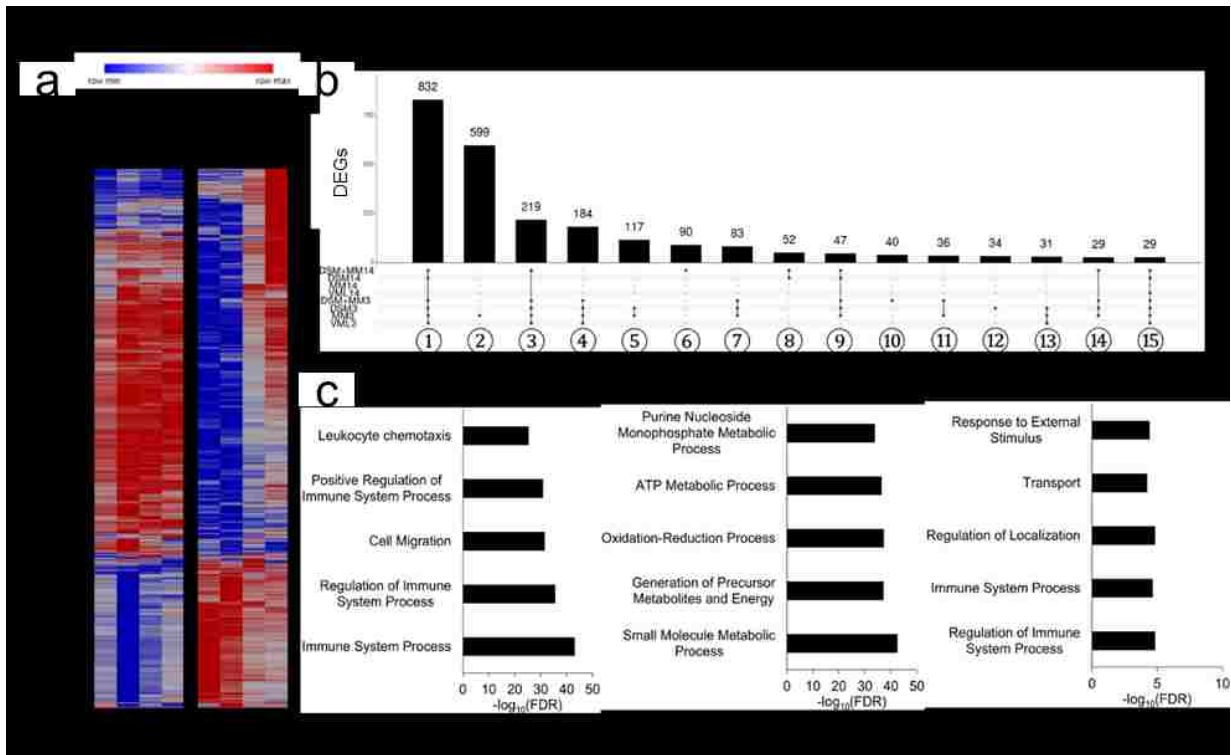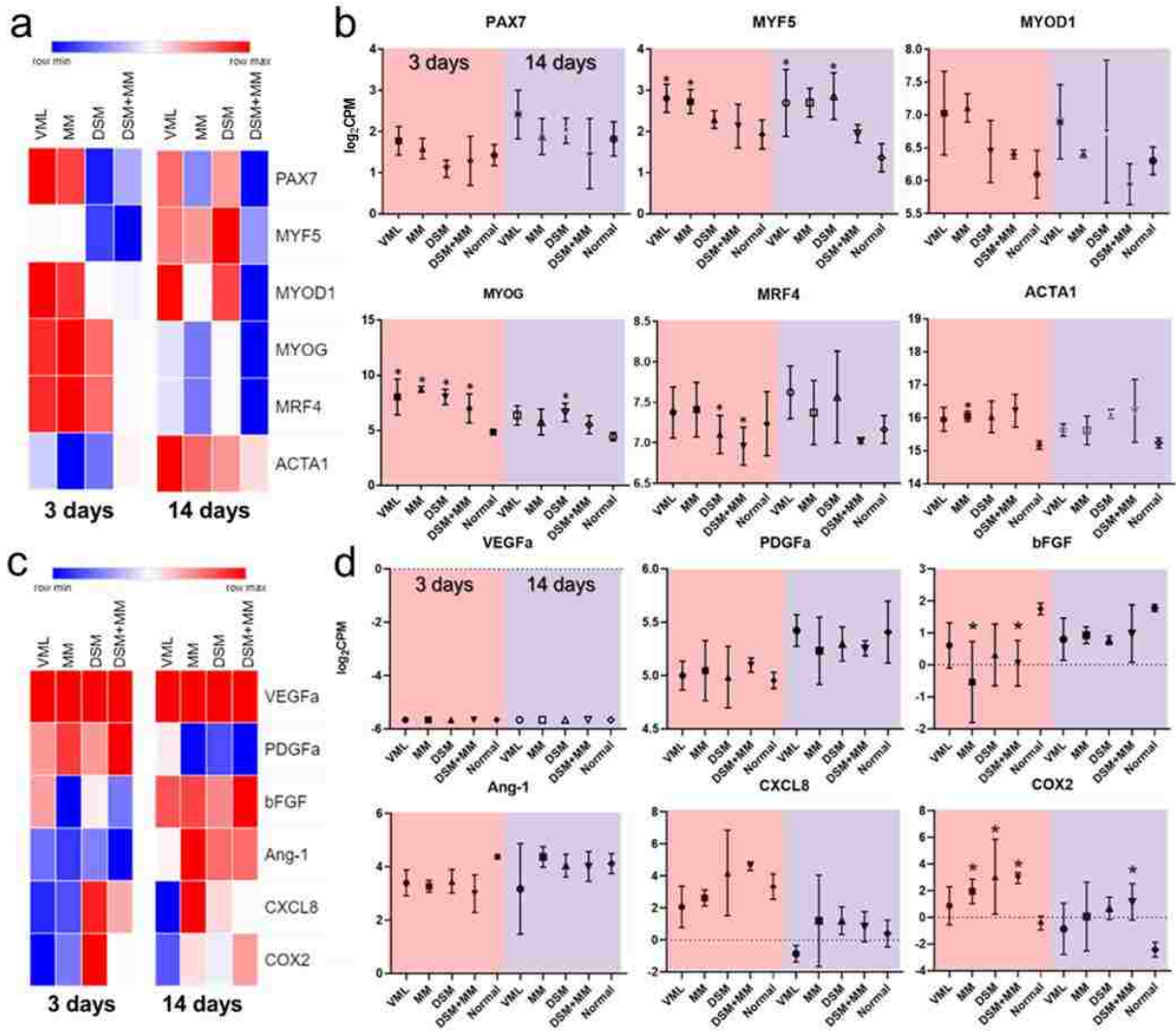Figure 1
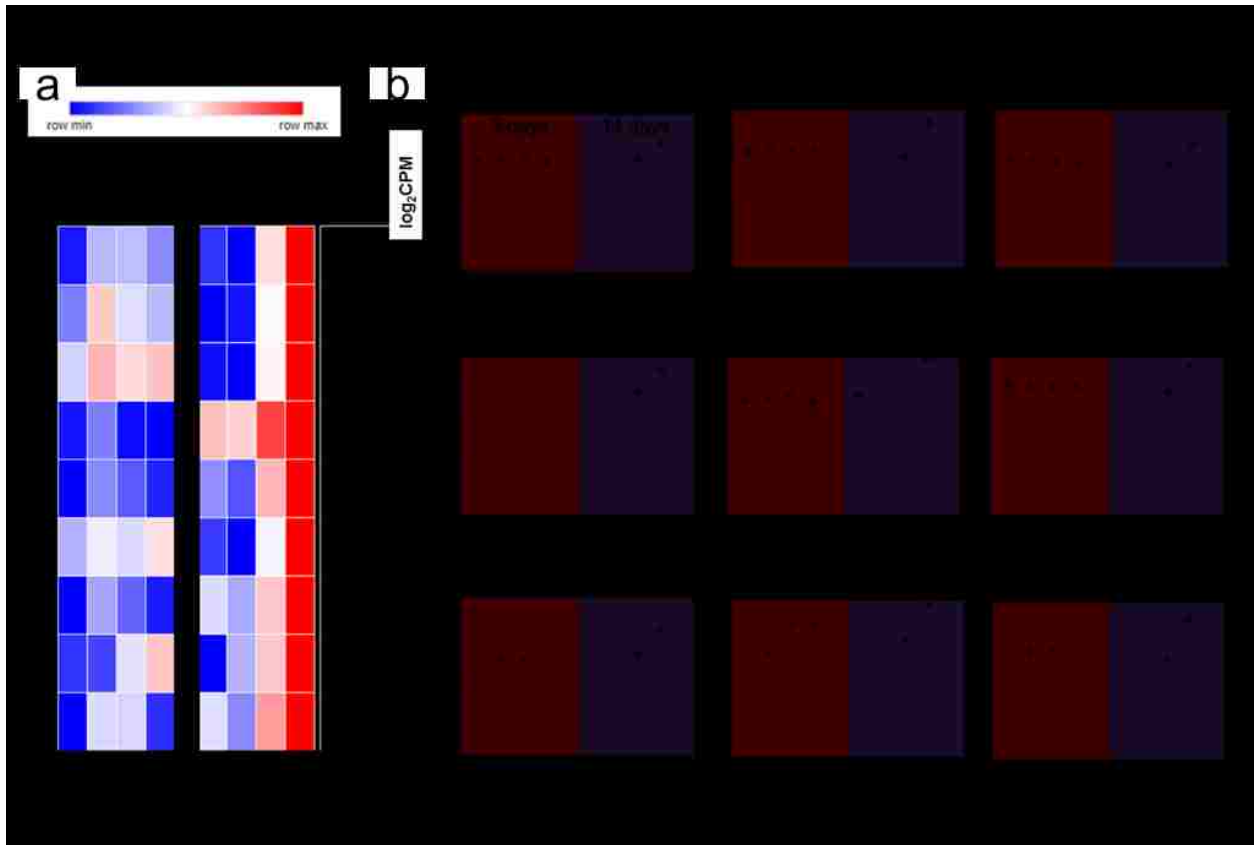
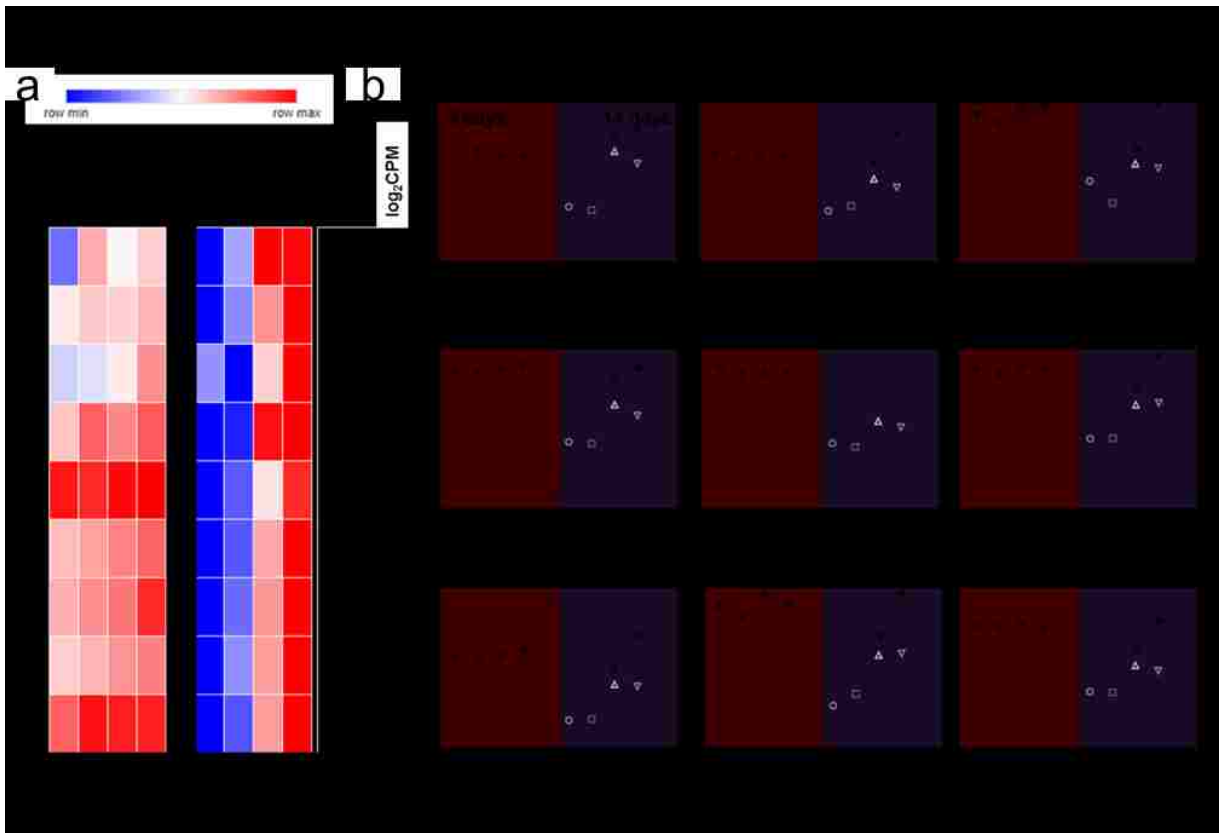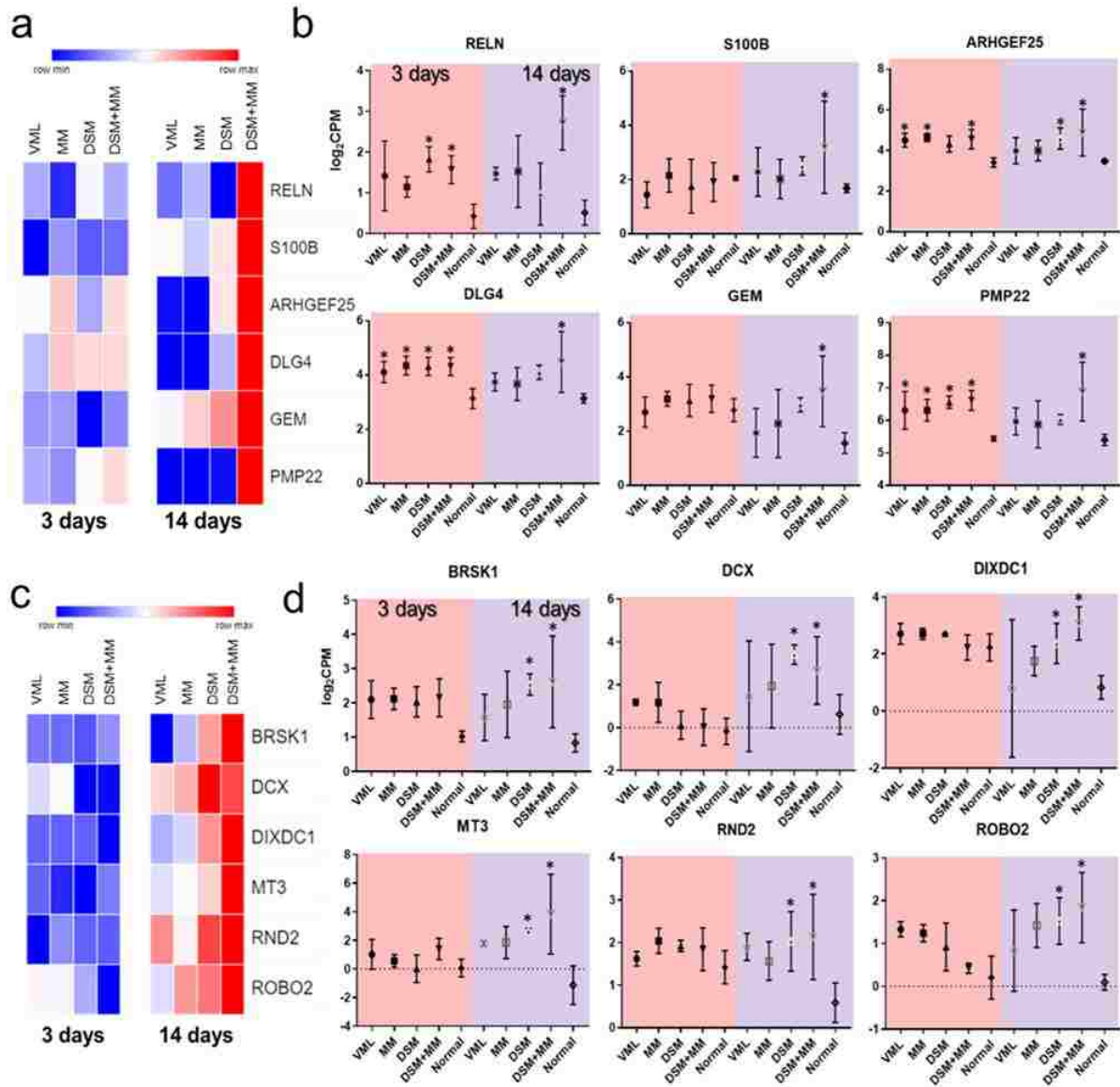Figure 2

Figure 3

157

Figure 4

Figure 5

Figure 6

Figure 7

161

Chapter 6

Conclusion

Despite significant advances in the past decade in the engineering of therapeutic biomaterials at the lab scale, little change has occurred in the fundamental clinical practice of treating VML. The ~22 human subjects evaluated across 4 VML clinical reports[1-4] of ECM-based therapies exhibit substantial variation in degree and site of injury which makes rigorous assessment of implant efficacy difficult. Additionally, the differing methods for assessing functional outcome between clinical studies and the broad preclinical VML literature suggest a need for future animal studies to add additional clinically relevant measures of functional recovery such as measures of range of motion. While electrophysiological stimulation provides a precise absolute measure of force recovery, this is generally replaced in humans subjects with the application of dynamometers, and the lack of biomechanical data in animals beyond raw force makes comparison to clinical reports difficult; application of a standardized noninvasive electrophysiological stimulation approach[5] between preclinical and clinical studies of VML may improve confidence in the clinical relevance of preclinical force data. Overall, a more controlled approach to clinical evaluation of VML therapies is necessary for translation of promising lab-scale therapies to the clinic. In particular, an opt-in HIPAA-compliant registry of clinical data from VML subjects -similar to those used for subject recruitment in cancer and diabetes research[6]- would enable improved communication between researchers and clinicians for mobilizing appropriate subjects for controlled trials.

A significant challenge in treating VML is that musculoskeletal clinicians are most likely to encounter patients long after their initial injury, when the site of the wound has already remodeled into a fibrotic mass which precludes regeneration of normal tissue. While the

magnitude of fibrosis in massive musculoskeletal trauma can be greater than that in the degenerative fibrosis of other tissues, recent findings suggesting the ability of specific compounds to revert fibrosis in the heart[7], liver[8], and other tissues[9] may be of use to the filed. Most VML preclinical studies have understandably focused on the idealized scenario of immediate repair of injury; given that this ideal is not reflected in the clinic, assessing the ability of biomaterials to promote functional regeneration long after the initial injury would provide clinically relevant insight. A transcriptomic study of VML in male rats was presented in chapter 5 suggesting that muscle force may be preserved in DSM+MM treatment of muscle, that promotion of neuroregenerative signaling may play a role in mediating this preservation, and that this preservation can be brought about in the two weeks following injury. Therefore, despite the (typically) months of time between the initial VML injury and onset of recuperative therapies, beginning therapeutic interventions immediately after injury may be critical to outcome. As the biological understanding of the skeletal muscle cell community in VML improves, it is evident that key biochemical information informing the design of therapeutic biomaterials will be more readily available. Specifically, elucidating key molecular mechanisms mediating skeletal muscle regeneration, inflammation, fibrosis, and innervation will provide tangible molecular targets which materials can be engineered to affect, by inclusion of exogenous molecules that act on specific pathways or by the codelivery of purposely-conditioned cells.

VML researchers have evaluated the effects of biological scaffolds and some myogenic precursor cell delivery on functional outcome, but this has generally occurred with little deliberate engineering of materials and cells for the microenvironment of skeletal muscle; certainly the cellular heterogeneity of any injured tissue complicates the usefulness of omics data in guiding the design of therapies, but recent advances in cell sorting for these technologies are

already providing a wealth of remarkably informative data for the regeneration of various tissues that is currently missing in VML.[10-14] Of the three investigations applying RNA-sequencing to VML injury and repair[15,16] -including that of this author described in chapter 5- none isolate the global transcriptomic response of specific cell types in VML. Additionally, missing from the VML research community is the application of other next-generation technologies such as quantitative mass spectrometry proteomics.[17] Integration of data from transcriptomic and proteomic methods is currently providing to other areas of biology[18-21] a more comprehensive screening of relevant cell behavior than classic methods (qPCR, western blot, etc.), and it is the opinion of this author that the collective understanding of VML pathobiology and repair will benefit greatly from their application. Further, the continually decreasing financial cost of these techniques is anticipated to lead to their application in personalized medicine[22], and the strategic decision to apply omics technologies to VML research now will provide datasets that would doubtlessly inform the development of future therapies.

Polymorphisms of individuals impairing peripheral nerve regeneration, myogenesis, and the inflammatory-to-constructive myeloid cell transition are key examples of personalized treatment targets assessable by next generation techniques. While sex differences in the outcome of VML-specific therapies have not been targeted for study thus far, the 2016 implementation of the Sex as a Biological Variable (SABV) policy by the NIH is expected to ameliorate this shortcoming. Interestingly, limited study demonstrates that female muscle-derived stem cells exhibit a capacity for regeneration greater than their male counterparts[23], with the mechanism responsible remaining unclear. Thus, not only may outcome vary between the sexes, but the expectation that female donor cells outperform those of males also necessitates that future studies report and consider the sex of delivered cells in their analyses.

In addition to adopting more high throughput methods for analyzing transcriptomic and proteomic changes relevant to VML and potential interventions, a redoubled exploration of musculoskeletal molecular biology may be clinically useful; in particular, study of epigenetic changes such as DNA methylation at cytosine-guanine (CpG) dinucleotides, histone modification, and noncoding RNA expression may play roles in muscle injury and regeneration. Epigenetic modifications are both reversible and can cause pathologically relevant changes in gene expression, with several inhibitors of histone deacetylation and DNA methylation having been FDA-approved and clinically applied.[24] Notably, evidence suggests that DNA methylation is in activating the expression of several genes during the commitment of cells to a myogenic lineage.[25] For example, the activation of the myogenic gene program following satellite cell activation is now known to be mediated by decreases in NAD+ and a consequent decrease in the deacetylase SIRT1, allowing for increased acetylation of lysine 16 of histone 4[26], a particularly important site whose acetylation leads to conversion of heterochromatin to euchromatin, making sites throughout the genome more accessible for transcription.[27] DNA methylation itself is known to increase substantially during aging with such predictability that one group developed a DNA methylation model which predicts age from DNA methylation profile with a correlation of 96% and error of approximately 3 years.[28] Sarcopenia[29] and reduced satellite cell content[30] are observed in the elderly, with SPRY1 being one site of age-associated DNA methylation resulting in reduction of the available pool of quiescent satellite cells.[31] Interestingly, acute exercise has been shown to reduce methylation of genomic sites associated with skeletal muscle metabolism, suggesting a role for methylation in the effects of physical therapy in the elderly and a specific mechanism by which increased activity may minimize the deleterious effects of aging on skeletal muscle.[32,33] Whole genome bisulfite sequencing is the current gold-standard tool for detection of

DNA methylation[34] and its application in combination with transcriptomic and proteomic techniques will provide an additional layer of biological insight for VML treatment.

Noncoding RNAs (ncRNAs) are RNA molecules which have independent functions and do not generally undergo translation into peptides, with many functioning to regulate gene expression across the transcriptome.[35] A number of ncRNAs have been shown to govern satellite cell proliferation and differentiation.[36-38] Circular RNAs (circRNAs) are a relatively unexplored class of RNA molecules which are relatively stable compared to their linear counterparts, with some demonstrated potential to bind microRNA molecules.[39] NcRNAs -including circRNAs- are in some cases enriched in exosomes[40,41], including those of muscle-resident cells, with the potential to directly affect the muscle fibrosis and regeneration.[42,43] Recent direct evidence of cell-to-cell contacts and exosome exchange between macrophages and satellite cells from activation through myoblast fusion suggests a direct intracellular crosstalk which could be mediated in part by the exchange of noncoding RNAs; elucidating the identities and functions of relevant noncoding RNAs in skeletal muscle and their responses to injury and biomaterial therapies should therefore be yet another goal in bettering the collective understanding of VML pathobiology.

Remarkable insights have recently been made in the understanding of vertebrate limb regeneration observed in *Urodela* amphibians which are relevant to muscle regeneration. While humans have homologs for many of the same key limb regeneration associated genes as *Urodela*, in practice these are not typically expressed following injury. Limb-regenerating vertebrates mobilize the dedifferentiation of injury-adjacent cells to form a blastema, from which these cells can redifferentiate to reform the complete range of tissues in a limb.[44] Interestingly, the dedifferentiated cells do not appear to be fully pluripotent; rather, they retain a memory of

their tissue origin and remain committed to a tissue-specific lineage. For example, dedifferentiated skeletal muscle cells contribute to reformation of skeletal muscle in a limb but do not contribute to cartilage formation.[45] Recapitulating this process in humans is considered to be eventually feasible, but recent estimates of treatment time indicate that the time course for complete regeneration of a whole limb from a functioning blastema would likely range from 2-5 years, with complex pharmacological cues to guide morphogenesis throughout treatment.[46] Forming a functional blastema in humans is an awesome interdisciplinary challenge which will require extensive series of studies mapping the process as it exists in current models and engineering human cells to mimic it. A complete genome sequence for the critical regenerative model *Ambystoma mexicanum* was only recently published in 2018[47] with a chromosome-scale assembly of the massive 32 Gb genome released in early 2019.[48] A complete definition of the molecular mechanisms mediating blastema formation in both amphibian models and mammalian digit tip regeneration will be a necessary step toward limb regeneration.[49] Despite the enormous technical challenges involved, limb regeneration in amphibians is the only extensively characterized example of complete vertebrate muscle regeneration following VML, and so engineering this process in human cells -which retain much of the necessary machinery involved- might be the most fruitful approach for achieving complete functional regeneration over the long term.

Autologous muscle transfer is occasionally performed as a treatment for muscle loss, but clearly results in morbidity at the donor site (typically the latissimus dorsi first used for head and neck reconstruction in 1978[50] or the gracilis[51-54]) and can require a prohibitively large volume of tissue in the case of VML.[55] Thus, there is interest in the *in vitro* production of tissue-like constructs that could be transplanted. Regarding the *in vitro* production of ECM scaffolds which

provides finer control over implant composition and architecture, scale-up of methods for the

bulk production of ECM will be needed to generate a clinically useful amount of tissue. A

number of bioreactor schemes are available that could be applied for this purpose, including

existing hollow fiber membrane bioreactors with the potential to leverage the productivity of cell

densities as high as 10^{10} cells per membrane cartridge.[56] The rapid proliferation of mammalian

cells in dynamic bioreactors additionally provides the opportunity for expansion of a patients'

own precursor cells and, thereby, production of an autologous ECM minimizing foreign epitopes

and their inflammatory consequences. A new approach for producing ECM *in vitro* was

described in chapters 2 and 3 whereby asymmetric hollow fiber membranes are used as a

sacrificial cell culture substrate for mammalian cells, with ECM isolated through the dissolution

of the membrane by an appropriate solvent as continuous threads of whole matrix. While the

effectiveness of implants derived from these threads in the treatment of VML is the subject of an

ongoing preclinical study, several avenues exist to improve upon this first generation of

sacrificial culture-derived ECM. The current platform is based on the static culture of fibroblasts

on hollow fibers, and therefore does not leverage the aforementioned benefits of dynamic

bioreactor culture with commercial membrane cartridges; evaluating sacrificial hollow fiber cell

culture at a pilot scale will better reveal the feasibility of this approach for satisfying a

commercial demand for ECM. A recognized concern in the approach is the use of irritating

solvents such as N-methyl-2-pyrrolidone (NMP) in the isolation of ECM from the sacrificial

membranes. While overall proteinaceous composition and retention of ECM constituents within

the resulting scaffolds is demonstrated in chapter 2, the potential effects of such solvents on

scaffold composition have not been extensively evaluated, and so the process may benefit from

modifications allowing for omission of solvent use. A promising approach may be to capitalize

upon the development of thermally responsive polymers such as PNIPAAM which can be dissociated from cells and ECM by a modest change in temperature. Conveniently, processes for preparing PNIPAAM-grafted hollow fibers are described in the literature[57-59] and have even been successfully exploited for isolation of adhered mammalian cells through the thermal dissociation mechanism.[59] Hu *et al* also developed a spinning process for producing wholly NIPAAM hollow fibers which could allow for streamlining the fabrication and cell culture processes into a single simultaneous step.[60]

In summary, VML is a challenging pathology which will require the coordinated interdisciplinary efforts of biologists, tissue engineers, materials scientists, and clinicians to address adequately. Clearly, much remains to be learned in terms of the molecular processes governing the homeostasis of normal skeletal muscle, let alone the processes relevant to recovery of muscle from severe trauma. However, new technologies now allow for their characterization at the genomic, epigenomic, transcriptomic, and proteomic scales which are expected to reveal clinically useful targets. Some biomaterial and cell delivery therapies for VML have been developed at the lab scale -including the DSM+MM approach- and have shown promising results at the preclinical stage. As the DSM component of this specific approach would likely require FDA regulatory approval, it may be prudent to begin assessing the approach across multiple animal models in anticipation of the regulatory process. Alternatively, clinical application of MM itself would not require regulatory approval. Regardless of the specific promising approaches that are translated, the differing methods for assessing functional outcomes (dynamometers, electrostimulation, etc.) in the preclinical and clinical settings should be unified to enhance the predictive value of VML animal studies on clinical outcome. In the longer term, developments in mammalian bioreactor systems and ECM isolation may enable the commercial

production of ECM with more control over implant architecture and composition than is allowed

with the simple decellularization of cadaveric tissues, with the possibility of proliferating a

patients' own cells, enabling the engineering of personalized ECM implants. Further yet, the

recent insights into limb regeneration in amphibian models and the conservation of relevant

genes across vertebrates hold the distant promise of leveraging the latent regenerative potential

of dedifferentiated cells, gene therapies, and pharmacological treatments for complete

regeneration of the tissue community of skeletal muscle from severe trauma.

References

1   Mase, V. J. *et al.* Clinical application of an acellular biologic scaffold for surgical repair of a large, traumatic quadriceps femoris muscle defect. *Orthopedics* **33** (2010).

2   Sicari, B. M. *et al.* An acellular biologic scaffold promotes skeletal muscle formation in mice and humans with volumetric muscle loss. *Science translational medicine* **6**, 234ra258-234ra258 (2014).

3   Dziki, J. *et al.* An acellular biologic scaffold treatment for volumetric muscle loss: results of a 13-patient cohort study. *Npj Regenerative Medicine* **1**, 16008, doi:10.1038/npjregenmed.2016.8

        https://www.nature.com/articles/npjregenmed20168#supplementary-information (2016).

4   Han, N. *et al.* Electrodiagnostic evaluation of individuals implanted with extracellular matrix for the treatment of volumetric muscle injury: case series. *Physical therapy* **96**, 540-549 (2016).

5   Downs, M. E. *et al.* Non-invasive peripheral nerve stimulation via focused ultrasound in vivo. *Physics in medicine and biology* **63**, 035011, doi:10.1088/1361-6560/aa9fc2 (2018).

6   Tan, M. H., Thomas, M. & MacEachern, M. P. Using registries to recruit subjects for clinical trials. *Contemporary clinical trials* **41**, 31-38 (2015).

7   Henry, B. L. *et al.* Relaxin suppresses atrial fibrillation in aged rats by reversing fibrosis and upregulating Na+ channels. *Heart Rhythm* **13**, 983-991, doi:https://doi.org/10.1016/j.hrthm.2015.12.030 (2016).

8   Ulmasov, B. *et al.* An Inhibitor of Arginine-Glycine-Aspartate-Binding Integrins Reverses Fibrosis in a Mouse Model of Nonalcoholic Steatohepatitis. *Hepatology communications* **3**, 246-261 (2019).

9   Zeisberg, M. & Kalluri, R. Reversal of experimental renal fibrosis by BMP7 provides insights into novel therapeutic strategies for chronic kidney disease. *Pediatric nephrology (Berlin, Germany)* **23**, 1395-1398, doi:10.1007/s00467-008-0818-x (2008).

10   Guerrero-Juarez, C. F. *et al.* Single-cell analysis reveals fibroblast heterogeneity and myeloid-derived adipocyte progenitors in murine skin wounds. *Nature Communications* **10**, 650, doi:10.1038/s41467-018-08247-x (2019).

11   Tikhonova, A. N. *et al.* The bone marrow microenvironment at single-cell resolution. *Nature*, doi:10.1038/s41586-019-1104-8 (2019).

12   Stuart, T. & Satija, R. Integrative single-cell analysis. *Nature Reviews Genetics* **20**, 257-272, doi:10.1038/s41576-019-0093-7 (2019).

13   Potter, S. S. Single-cell RNA sequencing for the study of development, physiology and disease. *Nature Reviews Nephrology* **14**, 479-492, doi:10.1038/s41581-018-0021-7 (2018).

14   Hu, G. *et al.* Single-cell RNA-seq reveals distinct injury responses in different types of DRG sensory neurons. *Scientific Reports* **6**, 31851, doi:10.1038/srep31851 https://www.nature.com/articles/srep31851#supplementary-information (2016).

15   Aguilar, C. A. *et al.* Multiscale analysis of a regenerative therapy for treatment of volumetric muscle loss injury. *Cell death discovery* **4**, 33 (2018).

16   Greising, S. M. *et al.* Unwavering pathobiology of volumetric muscle loss injury. *Scientific reports* **7**, 13179 (2017).

17   Guo, T. *et al.* Rapid mass spectrometric conversion of tissue biopsy samples into permanent quantitative digital proteome maps. *Nature Medicine* **21**, 407, doi:10.1038/nm.3807 https://www.nature.com/articles/nm.3807#supplementary-information (2015).

18   Michaut, M. *et al.* Integration of genomic, transcriptomic and proteomic data identifies two biologically distinct subtypes of invasive lobular breast cancer. *Scientific Reports* **6**, 18517, doi:10.1038/srep18517. https://www.nature.com/articles/srep18517#supplementary-information (2016).

19   Carlyle, B. C. *et al.* Isoform-Level Interpretation of High-Throughput Proteomics Data Enabled by Deep Integration with RNA-seq. *Journal of Proteome Research* **17**, 3431-3444, doi:10.1021/acs.jproteome.8b00310 (2018).

20   Voillet, V. *et al.* Integrated Analysis of Proteomic and Transcriptomic Data Highlights Late Fetal Muscle Maturation Process. *Molecular & Cellular Proteomics* **17**, 672-693, doi:10.1074/mcp.M116.066357 (2018).

21   Latonen, L. *et al.* Integrative proteomics in prostate cancer uncovers robustness against genomic and transcriptomic aberrations during disease progression. *Nature Communications* **9**, 1176, doi:10.1038/s41467-018-03573-6 (2018).

22   Suwinski, P. *et al.* Advancing Personalized Medicine Through the Application of Whole Exome Sequencing and Big Data Analytics. *Frontiers in Genetics* **10**, doi:10.3389/fgene.2019.00049 (2019).

23   Deasy, B. M. *et al.* A role for cell sex in stem cell–mediated skeletal muscle regeneration: female cells have higher muscle regeneration efficiency. *The Journal of cell biology* **177**, 73-86 (2007).

24   Kelly, T. K., De Carvalho, D. D. & Jones, P. A. Epigenetic modifications as therapeutic targets. *Nature biotechnology* **28**, 1069, doi:10.1038/nbt.1678 (2010).

25   Palacios, D. & Puri, P. L. The epigenetic network regulating muscle development and regeneration. *Journal of cellular physiology* **207**, 1-11 (2006).

26   Ryall, James G. *et al.* The NAD+-Dependent SIRT1 Deacetylase Translates a Metabolic Switch into Regulatory Epigenetics in Skeletal Muscle Stem Cells. *Cell Stem Cell* **16**, 171-183, doi:https://doi.org/10.1016/j.stem.2014.12.004 (2015).

27   Shia, W.-J., Pattenden, S. G. & Workman, J. L. Histone H4 lysine 16 acetylation breaks the genome's silence. *Genome biology* **7**, 217-217, doi:10.1186/gb-2006-7-5-217 (2006).

28   Hannum, G. *et al.* Genome-wide methylation profiles reveal quantitative views of human aging rates. *Molecular cell* **49**, 359-367 (2013).

29   Roubenoff, R. Sarcopenia and its implications for the elderly. *European journal of clinical nutrition* **54**, S40 (2000).

30   Verdijk, L. B. *et al.* Satellite cell content is specifically reduced in type II skeletal muscle fibers in the elderly. *American Journal of Physiology-Endocrinology and Metabolism* **292**, E151-E157 (2007).

31   Bigot, A. *et al.* Age-associated methylation suppresses SPRY1, leading to a failure of re-quiescence and loss of the reserve stem cell pool in elderly muscle. *Cell reports* **13**, 1172-1182 (2015).

32   Nitert, M. D. *et al.* Impact of an Exercise Intervention on DNA Methylation in Skeletal Muscle From First-Degree Relatives of Patients With Type 2 Diabetes. *Diabetes* **61**, 3322, doi:10.2337/db11-1653 (2012).

33   Barrès, R. *et al.* Acute Exercise Remodels Promoter Methylation in Human Skeletal Muscle. *Cell Metabolism* **15**, 405-411, doi:https://doi.org/10.1016/j.cmet.2012.01.001 (2012).

34   Olova, N. *et al.* Comparison of whole-genome bisulfite sequencing library preparation strategies identifies sources of biases affecting DNA methylation data. *Genome Biology* **19**, 33, doi:10.1186/s13059-018-1408-2 (2018).

35   Batista, P. J. & Chang, H. Y. Long noncoding RNAs: cellular address codes in development and disease. *Cell* **152**, 1298-1307 (2013).

36   Caretti, G. *et al.* The RNA Helicases p68/p72 and the Noncoding RNA SRA Are Coregulators of MyoD and Skeletal Muscle Differentiation. *Developmental Cell* **11**, 547-560, doi:https://doi.org/10.1016/j.devcel.2006.08.003 (2006).

37   Cesana, M. *et al.* A Long Noncoding RNA Controls Muscle Differentiation by Functioning as a Competing Endogenous RNA. *Cell* **147**, 358-369, doi:https://doi.org/10.1016/j.cell.2011.09.028 (2011).

38   Dey, B. K., Pfeifer, K. & Dutta, A. The H19 long noncoding RNA gives rise to microRNAs miR-675-3p and miR-675-5p to promote skeletal muscle differentiation and regeneration. *Genes & Development* **28**, 491-501, doi:10.1101/gad.234419.113 (2014).

39   Hansen, T. B. *et al.* Natural RNA circles function as efficient microRNA sponges. *Nature* **495**, 384 (2013).

40   Geisler, S. & Coller, J. RNA in unexpected places: long non-coding RNA functions in diverse cellular contexts. *Nature reviews Molecular cell biology* **14**, 699 (2013).

41   Gezer, U., Özgür, E., Cetinkaya, M., Isin, M. & Dalay, N. Long non-coding RNAs with low expression levels in cells are enriched in secreted exosomes. *Cell biology international* **38**, 1076-1079 (2014).

42   Zanotti, S. *et al.* Exosomes and exosomal miRNAs from muscle-derived fibroblasts promote skeletal muscle fibrosis. *Matrix Biology* **74**, 77-100, doi:https://doi.org/10.1016/j.matbio.2018.07.003 (2018).

43   Nakasa, T. *et al.* Acceleration of muscle regeneration by local injection of muscle-specific microRNAs in rat skeletal muscle injury model. *Journal of cellular and molecular medicine* **14**, 2495-2505 (2010).

44   Zielins, E. R., Ransom, R. C., Leavitt, T. E., Longaker, M. T. & Wan, D. C. The role of stem cells in limb regeneration. *Organogenesis* **12**, 16-27, doi:10.1080/15476278.2016.1163463 (2016).

45   Kragl, M. *et al.* Cells keep a memory of their tissue origin during axolotl limb regeneration. *Nature* **460**, 60, doi:10.1038/nature08152. https://www.nature.com/articles/nature08152#supplementary-information (2009).

46   Alibardi, L. Review: Limb regeneration in humans: Dream or reality? *Annals of Anatomy - Anatomischer Anzeiger* **217**, 1-6, doi:https://doi.org/10.1016/j.aanat.2017.12.008 (2018).

47   Nowoshilow, S. *et al.* The axolotl genome and the evolution of key tissue formation regulators. *Nature* **554**, 50, doi:10.1038/nature25458. https://www.nature.com/articles/nature25458#supplementary-information (2018).

48   Smith, J. J. *et al.* A chromosome-scale assembly of the axolotl genome. *Genome research* **29**, 317-324 (2019).

49   Simkin, J. *et al.* The mammalian blastema: regeneration at our fingertips. *Regeneration (Oxford, England)* **2**, 93-105, doi:10.1002/reg2.36 (2015).

50   Quillen, C. G., Shearin, J. J. & Georgiade, N. G. Use of the latissimus dorsi myocutaneous island flap for reconstruction in the head and neck area: case report. *Plastic and reconstructive surgery* **62**, 113-117 (1978).

51   Morrow, C. P., Lacey, C. G. & Lucas, W. E. Reconstructive surgery in gynecologic cancer employing the gracilis myocutaneous pedicle graft. *Gynecologic oncology* **7**, 176-187 (1979).

52   Kalisman, M. & Sharzer, L. A. Anal sphincter reconstruction and perineal resurfacing with a gracilis myocutaneous flap. *Diseases of the Colon & Rectum* **24**, 529-531 (1981).

53   Pickrell, K. L., Broadbent, T. R., Masters, F. W. & Metzger, J. T. Construction of a rectal sphincter and restoration of anal continence by transplanting the gracilis muscle: a report of four cases in children. *Annals of surgery* **135**, 853 (1952).

54   Greene, J. J., Tavares, J., Mohan, S., Jowett, N. & Hadlock, T. Long-Term Outcomes of Free Gracilis Muscle Transfer for Smile Reanimation in Children. *The Journal of pediatrics* **202**, 279-284. e272 (2018).

55   Liu, J. *et al.* Current methods for skeletal muscle tissue repair and regeneration. *BioMed research international* **2018** (2018).

56   Cadwell, J. J. Hollow Fibers Enhance Protein Expression: Mammalian Systems Excel in 3D Conditions Provided by Hollow Fiber Bioreactors. *Genetic Engineering & Biotechnology News* **38**, 20-21 (2018).

57   Li, H. *et al.* Preparation and characterization of pH-and thermo-sensitive polyethersulfone hollow fiber membranes modified with P (NIPAAm-MAA-MMA) terpolymer. *Desalination* **309**, 1-10 (2013).

58   Wang, W., Chen, L. & Yu, X. Preparation of temperature sensitive poly (vinylidene fluoride) hollow fiber membranes grafted with N-isopropylacrylamide by a novel approach. *Journal of applied polymer science* **101**, 833-837 (2006).

59   Zhuang, M., Liu, T., Song, K., Ge, D. & Li, X. Thermo-responsive poly (N-isopropylacrylamide)-grafted hollow fiber membranes for osteoblasts culture and non-invasive harvest. *Materials Science and Engineering: C* **55**, 410-419 (2015).

60   Hu, M. *et al.* Hydrodynamic spinning of hydrogel fibers. *Biomaterials* **31**, 863-869 (2010).

Appendix

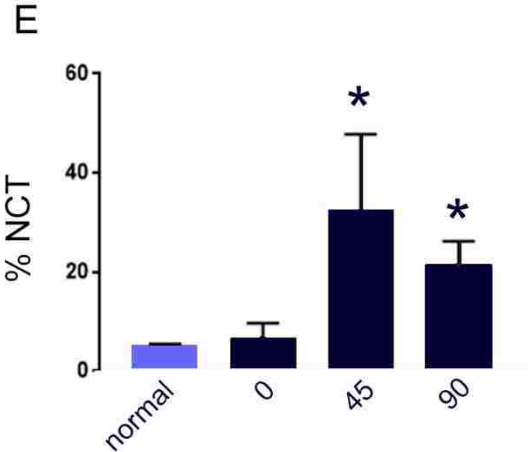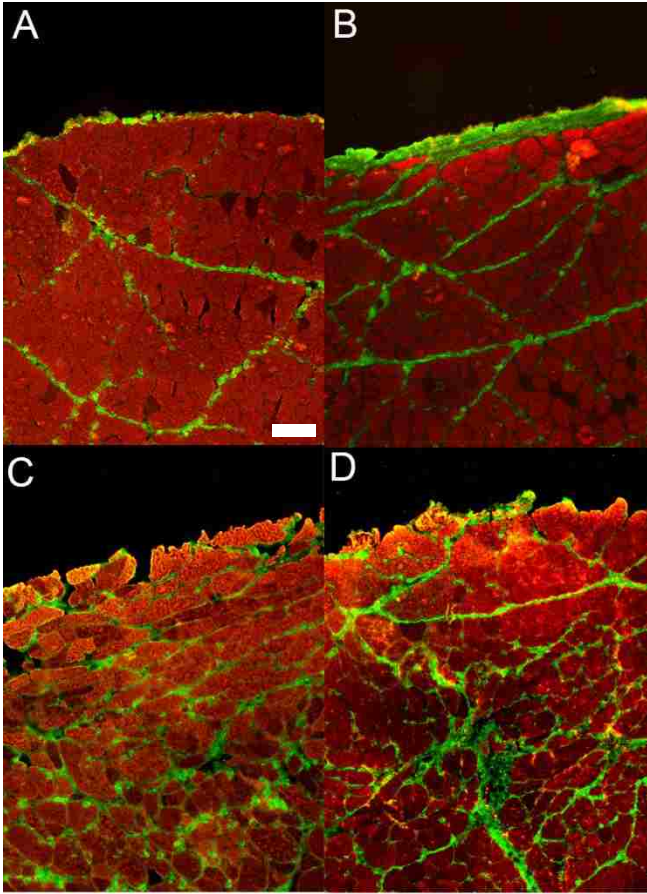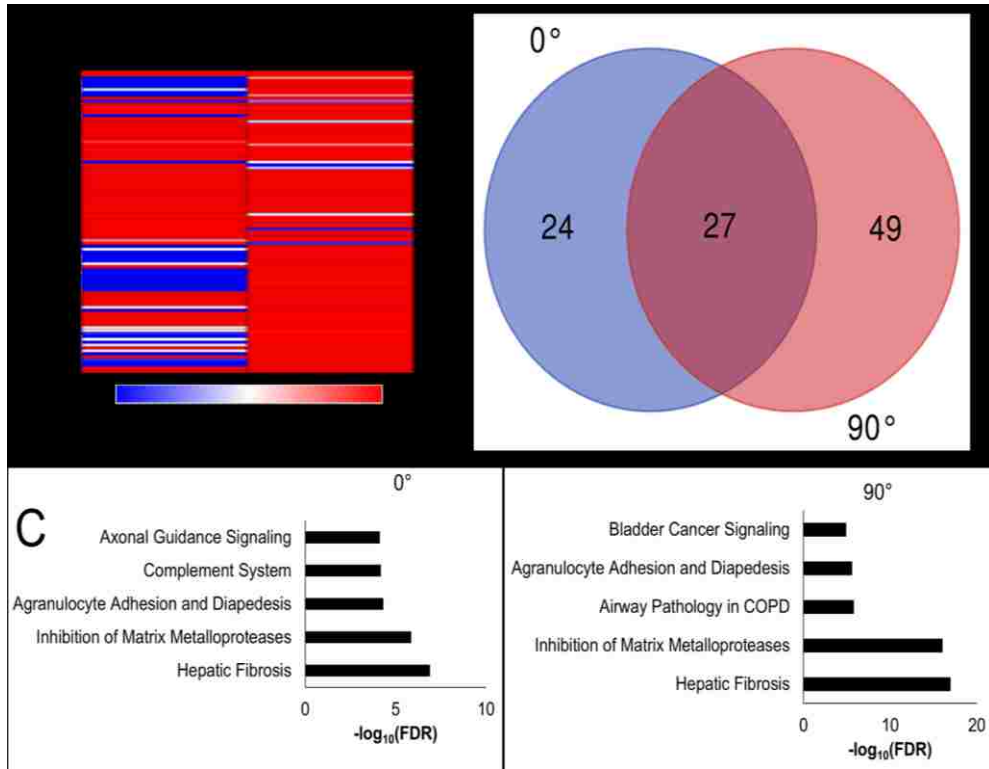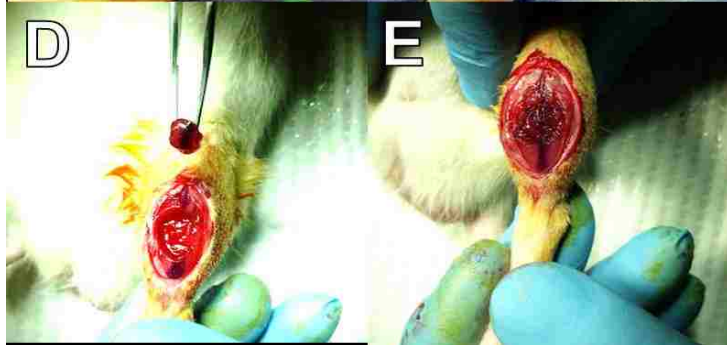**Effect of Autologous Muscle Graft Alignment on VML Outcome**

Figure 1

Figure 2

Rat tibialis anterior

Biopsy punch

Reinsert plug

Suture
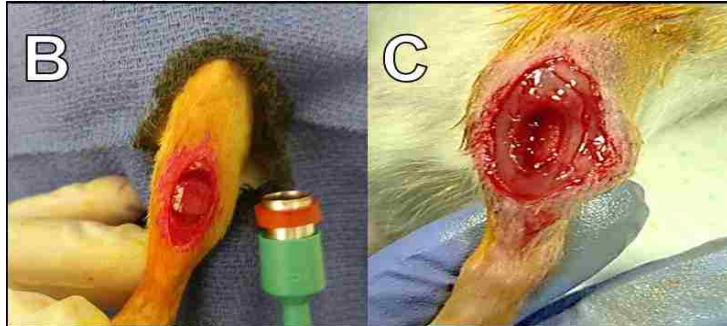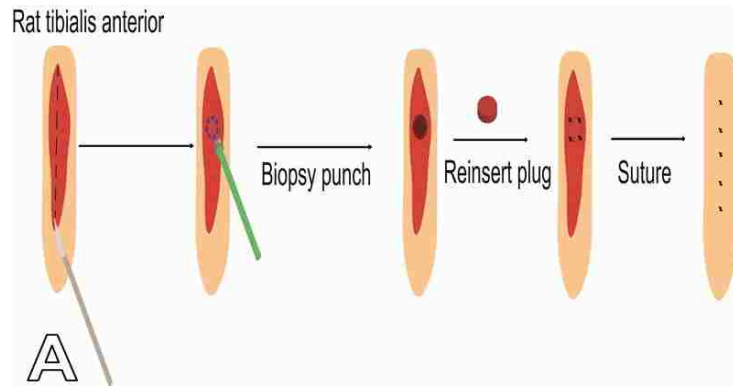
Figure Legend

Figure 1: Graft Alignment Correlates With Degree of Intramuscular Collagen

Deposition

Collagen I (green) and MHC (red) composite immunofluorescence imaging for (A) uninjured, (B) 0°, (C) 45°, and (D) 90° alignment groups at 12 weeks post injury, with (E) image analysis for noncontractile tissue area as a percent of total thresholded area. Scale-bar = 100 µm.

Figure 2: Transcriptome Profiling of Graft Alignment

(A) Heatmap of log2FC for all differentially expressed genes (104 unique DEGs) across all 0° and 90° groups relative to uninjured contralateral limbs at 2 weeks post-injury. (B) Visualization of the top DEG intersections across all groups with (C) the top canonical pathways for each group identified by Ingenuity Pathway Analysis.

Figure 3: Autologous Graft Excision and Reinsertion

(A) Graphical schematic of graft excision and reinsertion, with gross imaging of (B) biopsy, (C) defect creation, (D) graft alignment, and (E) graft reinsertion.

UNIVERSITY OF
ARKANSAS

Office of Research Compliance

To: Jeffrey Wolchok
Fr: Craig Coon
Date: November 15th, 2017
Subject: IACUC Approval
Expiration Date: November 14th, 2020

The Institutional Animal Care and Use Committee (IACUC) has APPROVED your protocol # **18055**: *Engineering a Muscle Regenerative Biomaterial*.

In granting its approval, the IACUC has approved only the information provided. Should there be any further changes to the protocol during the research, please notify the IACUC in writing (via the Modification form) prior to initiating the changes. If the study period is expected to extend beyond November 14th, 2020 you must submit a newly drafted protocol prior to that date to avoid any interruption. By policy the IACUC cannot approve a study for more than 3 years at a time.

The following individuals are approved to work on this study: Jeffrey Wolchok, Tyrone Washington, John Kim, and Kevin Roberts. Please submit personnel additions to this protocol via the modification form prior to their start of work.

The IACUC appreciates your cooperation in complying with University and Federal guidelines involving animal subjects.

CNC/tmp

180